Doping of Vapor–Liquid–Solid Grown Gallium Arsenide Nanowires

Henrik Mäntynen

School of Electrical Engineering

Thesis submitted for examination for the degree of Master of Science in Technology.

Espoo 09.03.2016

Thesis supervisor:

Prof. Harri Lipsanen

Thesis advisors:

M.Sc. Joona-Pekko Kakko

M.Sc. Tuomas Haggrén

Aalto University
School of Electrical
Engineering

AALTO UNIVERSITY
SCHOOL OF ELECTRICAL ENGINEERING

ABSTRACT OF THE
MASTER'S THESIS

Author: Henrik Mäntynen

Title: Doping of Vapor–Liquid–Solid Grown Gallium Arsenide Nanowires

Date: 09.03.2016 Language: English Number of pages: 9+78

Department of Micro- and Nanosciences

Professorship: Nanotechnology

Supervisor: Prof. Harri Lipsanen

Advisors: M.Sc. Joona-Pekko Kakko, M.Sc. Tuomas Haggrén

GaAs and other group III–V compound semiconductor nanowires are extensively researched and hold promise for several application areas like electronics, optoelectronics and photovoltaics. Most of the applications require electrical impurity doping for which accurate control and measurements remain challenging.

The aim of this work was to grow and characterize doped GaAs nanowires in order to forward the development of the growth process used by the Nanotechnology group. The nanowires were grown via the vapor–liquid–solid mechanism in a metal-organic vapor phase epitaxy device. Doping was done during the growth by using zinc and tin for p-type and n-type doping, respectively. The grown nanowires were inspected with scanning electron microscope and micro-Raman measurements. The doping levels (carrier concentrations) were estimated with electrical measurements, for which a metal contacting scheme employing optical lithography was investigated.

Doped nanowires were found to suffer from increased structural defect density and tapering to varying degrees compared to undoped reference nanowires. Aligning metal contacts and nanowires proved to be an issue and the investigated scheme hence did not work as well as expected. However, initial carrier concentration values were obtained for the current process. Based on the obtained results, additional measurements and growth process optimization were recommended.

Keywords: nanowire, gallium arsenide, doping, vapor–liquid–solid, metal-organic vapor phase epitaxy

AALTO-YLIOPISTO
SÄHKÖTEKNIIKAN KORKEAKOULU

DIPLOMITYÖN
TIIVISTELMÄ

Tekijä: Henrik Mäntynen

Työn nimi: VLS-mekanismilla kasvatettujen galliumarsenidinanolankojen seostaminen

Päivämäärä: 09.03.2016 Kieli: Englanti Sivumäärä: 9+78

Mikro- ja nanotekniikan laitos

Professuuri: Nanoteknologia

Työn valvoja: Prof. Harri Lipsanen

Työn ohjaajat: DI Joona-Pekko Kakko, DI Tuomas Haggrén

Galliumarsenidi- ja muita III-V puolijohdenanolankoja on tutkittu kattavasti ja ne ovat lupaavia moniin sovelluskohteisiin, kuten elektroniikkaan, optoelektroniikkaan ja aurinkokennotekniikkaan. Useimmat sovellukset edellyttävät seostamista sähköisillä epäpuhtauksilla, minkä hallinta ja mittaaminen ovat edelleen haastavia.

Täman työn tavoitteena oli kehittää Nanotekniikka-ryhmän kasvatusprosessia kasvattamalla ja karakterisoimalla seostettuja GaAs-nanolankoja. Nanolangat kasvatettiin VLS-mekanismin (vapor–liquid–solid) avulla käyttäen metalloorgaanista kaasufaasiepitaksialaitetta. Seostaminen suoritettiin kasvatuksen aikana käyttäen sinkkiä p-tyypin ja tinaa n-tyypin seostukseen. Kasvatettuja nanolankoja tarkasteltiin pyyhkäisyelektronimikroskopian ja mikro-Raman–mittausten avulla. Seostustasot (varauksenkuljettajatiheydet) arvioitiin käyttäen sähköisiä mittauksia, joita varten tutkittiin optista litografiaa hyödyntävää metallikontaktointimenetelmää.

Seostettujen nanolankojen havaittiin kärsivän vaihtelevasti lisääntyneistä rakenteellisista vioista ja enenevästi kaventuvasta muodosta verrattuna seostamattomiin vertailunanolankoihin. Metallikontaktien kohdistaminen nanolankoihin osoittautui ongelmalliseksi ja tutkittu kontaktointimenetelmä ei siksi toiminut niin hyvin kuin oli odotettu. Tämänhetkiselle kasvatusprosessille saatiin silti alustavat tulokset varauksenkuljettajatiheyksistä. Saatujen tulosten perusteella suositeltiin lisämittauksia ja kasvatusprosessin optimointia.

Avainsanat: nanolanka, galliumarsenidi, seostus, VLS-mekanismi, metalloorgaaninen kaasufaasiepitaksia

Preface

This thesis was conducted in the Nanotechnology group at the Department of Micro- and Nanosciences of Aalto University School of Electrical Engineering. I would like to thank Professor Harri Lipsanen for the opportunity to make my thesis in the group with such an interesting and challenging topic. I would also like to thank the instructors M.Sc. Joona-Pekko Kakko and M.Sc. Tuomas Haggrén for all the support, advice and practical guidance with the research. I owe my gratitude to Alexander Pyymäki Perros for performing the atomic layer deposition HfO_2 coating for one of the samples and to Joonas Holmi for providing the substrates for micro-Raman measurements and for advice regarding the device. Also, the rest of the personnel in the department of Micro and Nanosciences working in Micronova premises deserve my gratitude for creating a pleasant and motivating working atmosphere. Finally, I owe special thanks to my family for the support during my studies and the thesis work.

Otaniemi, 09.03.2016

Henrik Mäntynen

Contents

Symbols and abbreviations

Symbols

a	Lattice constant
$\vec{\mathbf{a}}_i$	Lattice vectors
$\vec{\mathbf{b}}_i$	Reciprocal lattice vectors
C_{gl}	Transistor gate capacitance per unit length
E	Energy
$\vec{\mathbf{E}}$	Electric field
E_{B}	Schottky barrier height (energy)
E_{c}	Conduction band (energy)
E_{F}	Fermi energy
E_{g}	Band gap (energy)
E_{v}	Valence band (energy)
f_{m}	Lattice mismatch (misfit)
$\vec{\mathbf{G}}$	Reciprocal lattice translation vector
g_{m}	Transconductance (gate–channel)
h	Planck constant ($6.62607004 \times 10^{-34}$ J s)
$\hbar$	Reduced Planck constant ($1.054571800 \times 10^{-34}$ J s)
I	Electric current
I_{D}	Transistor drain current
$\vec{\mathbf{k}}$	Wave vector
k_{B}	Boltzmann's constant ($1.38064852 \times 10^{-23}$ J / K)
L_{c}	Contact length
L_{ch}	Transistor channel length
L_{T}	Transfer length
m_{e}^*	Electron effective mass
m_{h}^*	Hole effective mass
n	Charge carrier concentration (electrons)
N_{A}	Acceptor concentration
N_{c}	Effective density of states in conduction band
N_{D}	Donor concentration
n_{i}	Intrinsic carrier concentration
N_{v}	Effective density of states in valence band
p	Charge carrier concentration (holes)
q	Elementary charge ($1.60217662 \times 10^{-19}$ C)
R	Electrical resistance
R_{c}	Electrical contact resistance
r_{nw}	Nanowire radius
T	Absolute temperature
$\vec{\mathbf{T}}$	Lattice translation vector
V	Voltage
V_{DS}	Transistor drain–source voltage

V_{GS}	Transistor gate–source voltage
V_{th}	Transistor threshold voltage
W	Depletion region width
η	Electrochemical potential
μ_{e}	Electron mobility
μ_{F}	Fermi level
μ_{h}	Hole mobility
ν_{a}	Nanowire axial growth rate
ν_{r}	Nanowire radial growth rate
ω	Angular frequency
Φ	Work function
ϕ_{s}	Nanowire surface potential
ρ	Electrical resistivity
ρ_{c}	Specific contact resistance
σ	Electrical conductivity
τ	Relaxation time
ε_{r}	Relative permittivity
ε_0	Vacuum permittivity ($8.854187817 \times 10^{-12}$ F / m)

Abbreviations

BCC	Body-centered cubic (lattice)
BSE	Backscattered electron
DEZn	Diethylzinc
EBL	Electron beam lithography
FCC	Face-centered cubic (lattice)
FE	Field emission
FET	Field effect transistor
FWHM	Full width at half maximum
HCP	Hexagonal close-packed (lattice)
MISFET	Metal–insulator–semiconductor field effect transistor
MOVPE	Metal–organic vapor phase epitaxy
PE	Primary electron
RIE	Reactive ion etching
SC	Simple cubic (lattice)
SCL	Space-charge-limited (current)
SE	Secondary electron
SEM	Scanning electron microscope (device)
	Scanning electron microscopy (technique)
TBAs	Tertiarybutylarsine
TE	Thermionic emission
TEM	Transmission electron microscope (device)
	Transmission electron microscopy (technique)
TESn	Tetraethyltin
TFE	Thermionic field emission

TMGa	Trimethylgallium
VLS	Vapor–liquid–solid (mechanism)
VSS	Vapor–solid–solid (mechanism)
WZ	Wurtzite (crystal structure)
ZB	Zinc blende (crystal structure)

1 Introduction

Semiconductor nanowires are crystalline structures with much larger extent in the axial than in the radial direction with dimensions typically in the order of micrometers and tens of nanometers, respectively. Although such structures can be, to some extent, fabricated by the traditional "top-down" lithographic techniques, nanowire growth via "bottom-up" approaches with self-assembly and controlled crystallization shows more promise and has attracted more attention. Consequently, only the latter type of nanowires are considered in this thesis.

GaAs and other group III–V compound semiconductor nanowires are extensively researched and one of the common techniques of growing them is the so-called vapor–liquid–solid (VLS) mechanism which promotes axial growth compared to radial growth. Nanowire VLS growth can be realized in a metal–organic vapor phase epitaxy (MOVPE) system which is the most common technique used for growing semiconductor nanowires [**1**, p. 146].

Nanowires have attracted increasing research interest in the recent years as they hold promise for several application areas. III–V nanowires could potentially be used in future generations of field effect transistors (FET) [**2**, **3**] or in novel devices like realizing spin-orbit qubits [**4**]. Optoelectronics and photovoltaic devices, like LEDs [**5**], lasers [**6**] and solar cells [**7**], are other major application areas – especially when integrated with the predominant Si technology. However, none of the envisioned or demonstrated devices have yet reached commercial production and there is still much research work to be done on the matter.

Most of the applications for semiconductor nanowires require controlled doping with electrically active impurity atoms in order to tune the conductivity. In planar thin film growth, doping is typically achieved by diffusion or ion implantation and the carrier concentration is determined with Hall measurements. However, the size and geometry of nanowires makes these standard techniques unsuitable. Instead, the common approaches are doping nanowires during the growth (in situ) and using electrical measurements employing FET structures to evaluate doping levels. However, quantitative carrier concentration measurements are challenging for nanowires and this limits the ability to understand and develop doping for them. [**8**]

The aim of this work was to grow and characterize doped GaAs nanowires in order to forward the development of the growth process used by the Nanotechnology group. A growth recipe for undoped GaAs nanowires was used as a starting point to which p-type doping with Zn (group II) and n-type doping with Sn (group IV) were added. The effects of doping on nanowire growth were investigated with scanning electron microscopy (SEM) and micro-Raman spectroscopy while electrical measurements were used to estimate the carrier concentrations as a function of the molar II/III and IV/III ratios. Furthermore, an electrical contacting method with a regular array of contact patterns defined via optical lithography was investigated here. Ideally, this method would be much faster and less tedious than defining a pattern for each nanowire individually with electron beam lithography (EBL).

The structure of this thesis is as follows. First, general theory on crystalline semiconductors is treated in section 2 giving the fundamental background for discussing

the crystalline structure and electrical properties of nanowires. Section 3 then more specifically discusses the nanowire growth and effects related to surface states and electrical contacts. The fabrication and characterization methods and devices, in turn, are introduced in section 4. Finally, the results are discussed in section 5 and conclusions are drawn in section 6.

2 Semiconductor theory

GaAs is a crystalline compound semiconductor material. This section first discusses the structure of crystalline materials and the conventional ways of representing and handling such constructs. The crystalline structure is of paramount importance to both the electrical properties and the growth of a nanowire. Next, the band structure, electrical conductivity and doping in semiconductors are reviewed. These determine the response of a semiconductor to an applied electric field. In electronics, semiconductors are not used in isolation but rather as parts of structures. Therefore, metal contacts are typically unavoidable, as in this work. Consequently, the behavior of metal–semiconductor junctions is also discussed. Finally, an important functional semiconductor structure, a metal–insulator–semiconductor field effect transistor (MISFET), is presented shortly as a nanowire variant of this structure is employed in the electrical measurements conducted in this work.

2.1 Crystal structure

Group III–V compound semiconductor materials, as well as commonly used silicon substrates, have typically single crystalline structure. An ideal crystal structure is ordered, repeats indefinitely and can be described by a combination of a space lattice and a basis. A space lattice is an abstract set of points in space given by the translation vectors

$$\vec{\mathbf{T}} = u\vec{\mathbf{a}}_1 + v\vec{\mathbf{a}}_2 + w\vec{\mathbf{a}}_3\,, \tag{1}$$

where u, v and w are the complete set of integers and $\vec{\mathbf{a}}_1$, $\vec{\mathbf{a}}_2$ and $\vec{\mathbf{a}}_3$ are called the lattice vectors. The angles between the lattice vectors are denoted as $\angle(\vec{\mathbf{a}}_1,\vec{\mathbf{a}}_2) = \alpha$, $\angle(\vec{\mathbf{a}}_1,\vec{\mathbf{a}}_3) = \beta$ and $\angle(\vec{\mathbf{a}}_2,\vec{\mathbf{a}}_3) = \gamma$. The basis is a set of atoms the locations of which are given by vectors

$$\vec{\mathbf{R}}_i = x_i\vec{\mathbf{a}}_1 + y_i\vec{\mathbf{a}}_2 + z_i\vec{\mathbf{a}}_3\,, \tag{2}$$

where x_i, y_i and z_i are fractions. The crystal structure is obtained by substituting the basis set of atoms to each point in the space lattice defined by equation 1 such that the origin of a basis coincides with a lattice point. Since the crystal structure has perfect translational symmetry it is enough to just consider one block of the structure, a unit cell that can fill the space by repetition. A unit cell is called a primitive cell when it has the following properties: (i) it contains only one lattice point, (ii) it has the smallest possible size, and (iii) it has a basis set containing only one molecular unit of the material. [**9**, p. 3–11]

Neither unit cells nor primitive cells are unique for a given crystal structure, but for 3D crystals there exist only 14 different lattice types with special symmetry properties and these are called the Bravais lattices. Crystals in nature typically assume either cubic or hexagonal lattices and, therefore, more important Bravais lattices include: simple cubic (SC), body-centered cubic (BCC), face-centered cubic (FCC), and hexagonal close packed (HCP). The unit cells of these lattices are illustrated in figure 1. For cubic lattices $\alpha = \beta = \gamma = 90°$ and $|\vec{\mathbf{a}}_1| = |\vec{\mathbf{a}}_2| = |\vec{\mathbf{a}}_3| = a$, where a is called the lattice constant. For the hexagonal lattice $\alpha = 120°$, $\beta = \gamma = 90°$

and $|\vec{\mathbf{a}}_1| = |\vec{\mathbf{a}}_2| \neq |\vec{\mathbf{a}}_3|$. The conventional unit cells of BCC, FCC, and HCP lattices shown in figure 1 are not primitive but they better visualize the crystal structure. [**9**, p. 10–17]

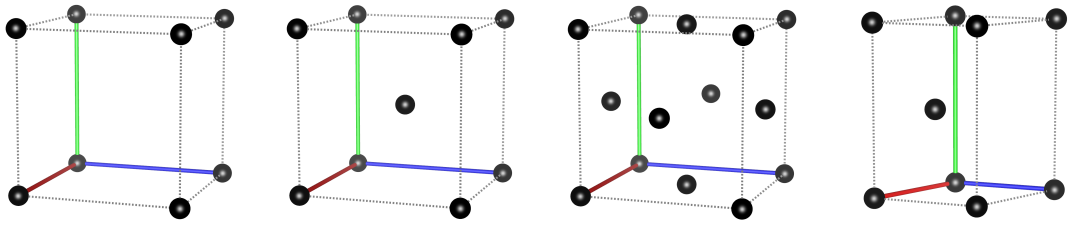

Figure 1: From left to right, conventional unit cells of the SC, BCC, FCC and HCP lattices. The lattice points are denoted with black spheres and the lattice vectors $\vec{\mathbf{a}}_1$, $\vec{\mathbf{a}}_2$ and $\vec{\mathbf{a}}_3$ are denoted with red, blue and green lines from the origin, respectively.

In order to navigate crystal structures, different directions and crystal planes need to be addressable. The conventional way of denoting directions is with three integers inside square brackets: $[uvw]$. These integers are obtained by first projecting the direction vector to the unit cell axes **a**, **b** and **c** and then dividing the projections with their highest common denominator to obtain the smallest integer numbers u, v and w, respectively. The complete set of equivalent directions is denoted with angular brackets: $\langle uvw \rangle$. Crystal planes are denoted with normal brackets as (hkl) and the integers h, k and l are called the Miller indices of the plane. The Miller indices are obtained by first taking the intersections of the plane along the unit cell axes: h', k' and l'. The reciprocals $1/h'$, $1/k'$ and $1/l'$ are then transformed to the smallest integers that still have the same ratios, i.e. h, k and l, respectively. The complete set of planes of the same type is denoted with curvy brackets: $\{hkl\}$. It is also conventional that for hexagonal lattices four Miller indices are used instead of three. These indices $(hkil)$ are obtained in the same way as before but using four axes **a**, **b**, **c** and **d**, respectively. Axes **a**, **b** and **c** lie in the basal plane in 120° angles with respect to each other and axis **d** is orthogonal to the other three. For both directions and planes negative integer values are denoted with a bar on top of the number. [**10**, p. 50–52] The axes of hexagonal lattices are shown in figure 2a and some important planes of both cubic and hexagonal lattices are shown in figures 2b and 2c.

Bulk III–V semiconductors typically have cubic zinc blende (ZB) structure but III–V nanowires also often exhibit hexagonal wurtzite (WZ) structure in parts of or throughout the whole nanowire [**11**]. The ZB crystal structure has an FCC lattice with a two atom basis ($\vec{\mathbf{R}}_1 = 0\vec{\mathbf{a}}_1 + 0\vec{\mathbf{a}}_2 + 0\vec{\mathbf{a}}_3$ and $\vec{\mathbf{R}}_2 = 1/4\vec{\mathbf{a}}_1 + 1/4\vec{\mathbf{a}}_2 + 1/4\vec{\mathbf{a}}_3$) where the atoms are dissimilar. ZB lattice is otherwise the same as diamond lattice except that in diamond lattice both atoms of the basis are similar. [**9**, p. 14–16] Silicon, for example, has the diamond crystal structure. The conventional FCC lattice can be divided to layers A, B and C along the [111] direction as shown in figure 3. The stacking sequence ABCABC in this direction then produces hexagonal layering

although the lattice is cubic [**9**, p. 17]. Similarly the ZB lattice can be divided to bilayers Aa, Bb and Cc (taking into account the two atom basis compared to FCC) and follows the AaBbCcAaBbCc stacking sequence. The WZ lattice, in turn, can be obtained with the AaBbAaBb stacking sequence. A change in the stacking sequence can take place rather easily and both ZB and WZ structures can be present in a single nanowire. [**11**] The ZB and WZ lattices and stacking sequences are illustrated in figure 4.

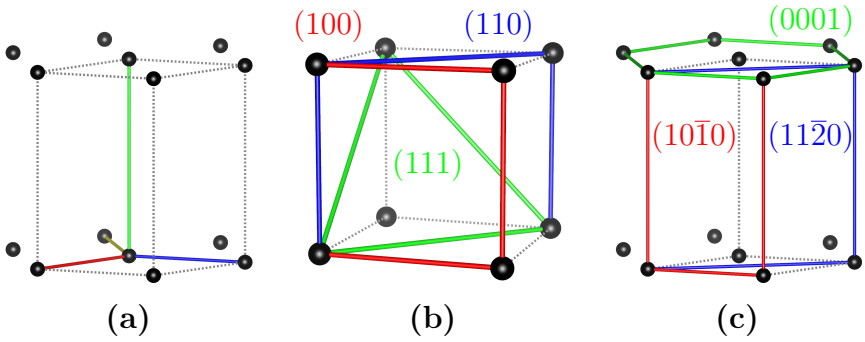

Figure 2: Axes in a hexagonal lattice (a) and some important planes in cubic (b) and hexagonal lattices (c). In (a) the axes **a**, **b**, **c** and **d** are denoted with red, blue, yellow and green lines, respectively.

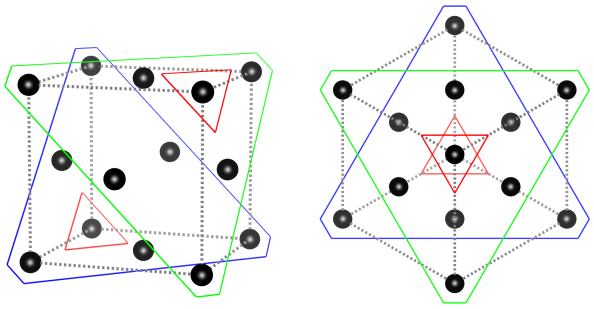

Figure 3: Layers A, B and C in the [111] direction of the FCC lattice. The layers are denoted with red, blue and green, respectively.

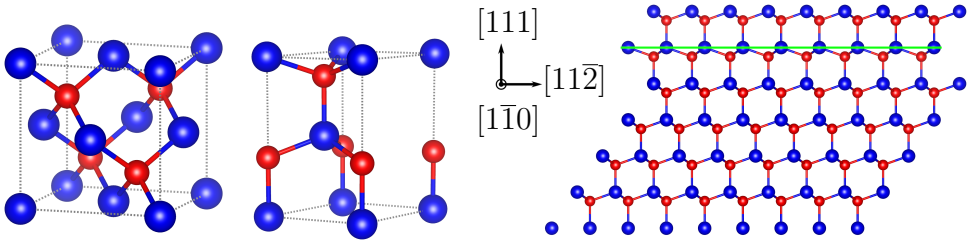

Figure 4: From left to right, the ZB and WZ lattices and a layer stack AaBbCcAaBb<u>A</u>aB showing both ZB and WZ stacking. Blue and red spheres denote Ga and As atoms, respectively and the green line marks layer <u>A</u>.

In reality, crystals are never ideal. Even in otherwise flawless crystals the perfect translational symmetry is broken due to the finite extent of the crystal. However, despite the small diameter of nanowires, the crystal structure still extends over very large distances compared to the lattice constant and an ideal crystal is good enough a model. Instead, other deviations from the ideal structure called crystal defects are more important. Crystal defects can be roughly divided to three categories based on their dimensionality: point defects (0D), line defects (1D) and planar defects (2D). Point defects include vacancies, substitutional atoms and interstitial atoms. Vacancy is a single atom missing from a lattice while a substitutional (impurity) atom substitutes one atom in the lattice. Interstitial atom is a single atom occupying an empty space in between the atoms of the lattice. If the interstitial atom is of the same material as the crystal it is called a self-interstitial. Line defects include e.g. dislocations (line defects associated with translational displacements of atoms in the lattice) while planar defects include e.g. stacking faults (changes in the normal stacking sequence). [**10**, p. 137–150] This work only considers impurity defects associated with doping and stacking faults occurring during nanowire growth. For example, a twin plane stacking fault in a ZB crystal occurs when a single bilayer is faultily stacked reversing the stacking sequence from AaBbCc to CcBbAa [**11**].

2.2 Energy bands

When atoms bond together to form a solid, instead of discrete atomic energy states, there will be bands of such a high number of allowed states that they can be considered approximately continuous in energy. In an ideal crystal, the (nearly) free-electron-like valence electrons can be treated as delocalized waves that are solutions of the Schrödinger equation (describing the quantum-mechanical behavior of the electrons) and the electron wave vectors ($\vec{\mathbf{k}}$) of these solutions then determine the bands of allowed energy states in reciprocal space ($\vec{\mathbf{k}}$–space) [**10**, p. 289–290]. Another way by which a band structure may be thought to arise is by the overlap with or interaction between atomic orbitals of the material (this being more pronounced for e.g. materials that form covalent bonds) [**10**, p. 329]. However, both of these approaches to model the band structures work within the independent-electron approximation in which the (individual) electron-electron interactions have been neglected [**10**, p. 361].

For each real-space lattice with translation vectors $\vec{\mathbf{T}}$ (equation 1) there exists a corresponding reciprocal lattice defined by translation vectors

$$\vec{\mathbf{G}} = \frac{2\pi\vec{\mathbf{n}}_{hkl}}{d_{hkl}}\,, \tag{3}$$

where $\vec{\mathbf{n}}_{hkl}$ is the unit normal vector for (hkl) planes of the real-space lattice and d_{hkl} is the spacing of these planes. Each point $\vec{\mathbf{G}}$ in reciprocal space corresponds to a family of planes $\{hkl\}$ in real space. Equivalently, the reciprocal lattice translation vectors can be defined as

$$\vec{\mathbf{G}} = h\vec{\mathbf{b}}_1 + k\vec{\mathbf{b}}_2 + l\vec{\mathbf{b}}_3\,, \tag{4}$$

where $\vec{\mathbf{b}}_1$, $\vec{\mathbf{b}}_2$ and $\vec{\mathbf{b}}_3$ are the lattice vectors of the reciprocal lattice. Therefore,

$\vec{\mathbf{G}} \bullet \vec{\mathbf{T}} = 2\pi(hu + kv + lw)$ and the lattice vectors satisfy

$$\begin{cases} \vec{\mathbf{b}}_i \bullet \vec{\mathbf{a}}_j = 2\pi, & i = j \\ \vec{\mathbf{b}}_i \bullet \vec{\mathbf{a}}_j = 0, & i \neq j \end{cases}.$$

A general point in the reciprocal space is $\vec{\mathbf{k}} = k_1\vec{\mathbf{b}}_1 + k_2\vec{\mathbf{b}}_2 + k_3\vec{\mathbf{b}}_3$ with any coefficients k_1, k_2, k_3. [**10**, p. 90-91] For example, the BCC lattice is transformed into a reciprocal lattice with FCC structure and the FCC lattice is transformed into reciprocal lattice with BCC structure correspondingly. More generally, the reciprocal lattice is obtained from the corresponding real-space lattice via a spatial Fourier-transform. [**9**, p. 85–86]

The smallest space filling unit of a reciprocal lattice is its Wigner–Seitz cell and is referred to as the first Brillouin zone. The Wigner–Seitz cell is constructed by first taking the central lattice point ($\vec{\mathbf{k}} = 0$) and then bisecting the lines between the central and all other lattice points with planes. The smallest volume such enclosed around the central point forms the cell. Higher order Brillouin zones are defined similarly by progressively taking the next-smallest enclosed volume beyond the previous zones. [**10**, p. 93–94] Since the energy bands are four-dimensional quantities (energy as a function of three reciprocal space coordinates), band structures can readily be visualized only along trajectories in the $\vec{\mathbf{k}}$–space, typically chosen between certain points of symmetry in the first Brillouin zone of a given reciprocal lattice [**10**, p. 312]. For the reciprocal lattice of the FCC structure, these special points are: Γ (0, 0, 0), X (1, 0, 0), W(1, 1/2, 0), K(3/4, 3/4, 0) and L(1/2, 1/2, 1/2) (in units of $2\pi/a$) [**10**, p. 95]. The first Brillouin zone of the reciprocal lattice of the FCC structure (and hence ZB structure) along with it's special points is shown in figure 5.

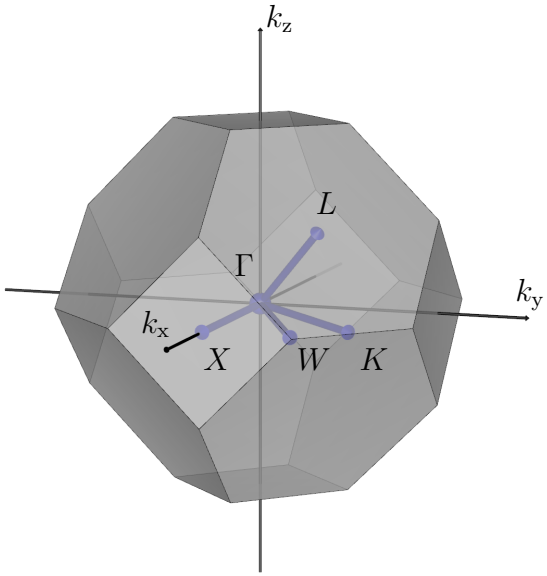

Figure 5: First Brillouin zone of the reciprocal lattice of the FCC structure and the special points Γ, X, W, K and L.

The translational symmetry in the real-space lattice results in periodic potential seen by the electrons and, therefore, the electron wavefunctions and corresponding eigenenergies in the reciprocal space are also periodic. This periodicity means that all allowed $\vec{\mathbf{k}}$-values fall within the first Brillouin zone since all values (bands) outside the first Brillouin zone can be folded inside it by a translation with an appropriate reciprocal lattice vector. The presentation in which the entire band structure is represented inside the first Brillouin zone is called the reduced-zone scheme. [**10**, p. 309–314] The full number of bands in the structure is equal to the number of atoms in the basis of the crystal structure (e.g. two in the case of GaAs) multiplied by the number of atomic orbitals involved and each band contains two states per atom in the crystal (the factor of two corresponding to spin-up and spin-down states). [**10**, p. 345] According to the Pauli exclusion principle, two electrons can not have the exact same state and therefore each state in a band can only be occupied by a single electron.

Electrons fill the allowed states in the bands according to thermodynamics, such that at absolute zero temperature the electrons assume configuration with the lowest total energy. Since electrons are fermions, their thermodynamic behavior is described by the Fermi–Dirac distribution function:

$$f_{\mathrm{FD}}(E) = \frac{1}{e^{\frac{E-\mu_{\mathrm{F}}}{k_{\mathrm{B}}T}} + 1}\,, \tag{5}$$

where E is electron state energy, μ_{F} is the Fermi level (chemical potential), k_{B} is the Boltzmann's constant and T is the absolute temperature. The Fermi–Dirac distribution expresses the probability that an electron state with energy E is occupied at temperature T. The zero-temperature chemical potential is called the Fermi energy ($E_{\mathrm{F}} \equiv \mu_{\mathrm{F}}|_{T=0\mathrm{K}}$). At $T = 0$ K the distribution becomes a step function meaning that all states with energy below the Fermi energy ($E < E_{\mathrm{F}}$) are occupied and all higher energy states are unoccupied. At higher temperatures, thermal energy can excite electrons to higher-energy states such that there is a finite probability that some states above E_{F} are occupied and, correspondingly, some states below E_{F} are left unoccupied. The Fermi level above $T = 0$ K then marks the energy with 50 % probability of state occupation. [**10**, p. 297, 490–491] In the $\vec{\mathbf{k}}$–space, the Fermi level defines a surface $E(\vec{\mathbf{k}}) = \mu_{\mathrm{F}}$.

Energy regions between bands, devoid of allowed states everywhere in $\vec{\mathbf{k}}$–space, are called band gaps. If the Fermi level is inside a band gap (i.e. there are only completely filled bands below it and empty bands above it at $T = 0$ K), the highest occupied bands are called valence bands while the lowest unoccupied bands are called conduction bands. Furthermore, those materials for which the conduction band minimum and valence band maximum occur at the same point in $\vec{\mathbf{k}}$–space are termed direct band gap materials and those for which the minimum band gap occurs between different $\vec{\mathbf{k}}$–values are termed indirect band gap materials. [**10**, p. 345] Bulk GaAs, for example, is a direct band gap material with a band gap energy of $E_{\mathrm{g}} = 1.52$ eV (at $T = 0$ K) [**10**, p. 351]. This band gap is due to the hybridization of atomic orbitals: the s and p orbital states do not form separate bands but instead combine (hybridize) to form new hybrid sp^3–orbitals with corresponding bands. The

sp^3–hybrids can form bands from either bonding or antibonding combinations and these will be separated by the band gap. [**10**, p. 337–344] Figure 6 shows an example of a modeled band structure for GaAs.

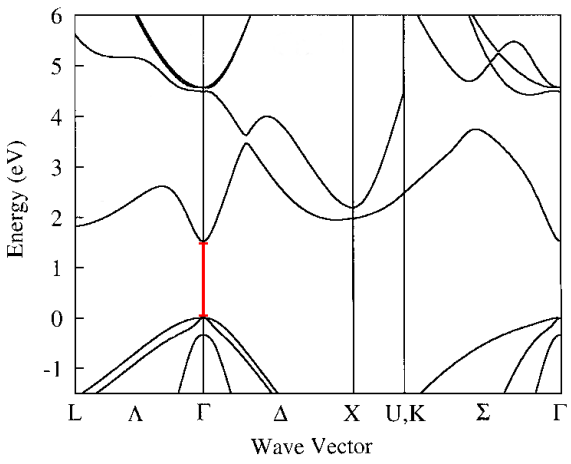

Figure 6: Modeled band structure for GaAs (the direct band gap occurs at the Γ–point). Modified from [**12**].

2.3 Electrical conductivity

Electrical (metallic) conduction in crystalline materials can be understood with the help of the electronic band structure. When electron dynamics are considered in a crystalline material, it needs to be taken into account that the electrons interact with the lattice and form a system. Therefore, the inertial mass of an electron needs to be replaced with an effective mass (m_e^*) and the electron momentum becomes crystal momentum ($\hbar\vec{\mathbf{k}}$) that can be transferred freely between an electron and the lattice. The electron effective mass results from the band structure and is inversely proportional to the local $\vec{\mathbf{k}}$–space curvature of a given band as:

$$m_e^* = \frac{\hbar^2}{\nabla_k^2 E(\vec{\mathbf{k}})}\,, \tag{6}$$

where $\hbar$ is the reduced Planck constant (more generally, m_e^* can be a tensor quantity). [**10**, p. 421–424] Furthermore, the electrons can only exist in the allowed states of the band structure and no two electrons can occupy the same state due to the Pauli exclusion principle.

In the equilibrium state, i.e. in the absence of external fields and chemical potential or temperature gradients, electrons occupy $\vec{\mathbf{k}}$–space states according to the Fermi–Dirac distribution and there is no net crystal momentum and hence no electric current flow. When the crystal is subject to an applied electric field ($\vec{\mathbf{E}}$), the electrons gain momentum in the direction of the field and the entire electron distribution is shifted in $\vec{\mathbf{k}}$–space resulting in net momentum and current. The electrons would continue to gain momentum were it not for scattering due to lattice

defects, phonons and other electrons. Both inelastic and elastic scattering work to oppose the electron distribution shift, although electrons can scatter to states within the equilibrium distribution only inelastically. Overall, the scattering limits the $\vec{\mathbf{k}}$–space shift of the electron distribution to a finite steady-state value corresponding to a constant net momentum and current. At normal temperatures well above $T = 0$ K, the electron–phonon scattering is the dominant scattering mechanism while, in general, the electron–electron scattering is negligible. [**10**, p. 429–436] However, the $\vec{\mathbf{k}}$–space shift is, in the first place, only possible if there are unoccupied states into which electrons can shift.

The classification of crystalline materials into insulators, conductors and semiconductors is (in simple terms) explained by the degree of band filling. In insulators, the valence band is completely filled, the conduction band is empty and there is a sufficiently large band gap between the two such that thermal excitation of electrons from valence to conduction band is negligible at finite temperatures. Therefore, there are no vacant states to which the valence band electrons could shift and the applied field is unable to alter the initial distribution leaving the net momentum as zero. In conductors, the highest occupied band (or bands) are only partially filled, which means that vacant states are readily available. Semiconductors, on the other hand, are similar to insulators but have sufficiently small band gap such that electrons can be thermally excited from the valence to conduction band at finite temperatures. Therefore, both the valence and conduction band contain electrons and vacant states. [**10**, p. 323–325] These differences are schematically illustrated in figure 7. GaAs is a semiconductor due to the relatively small band gap.

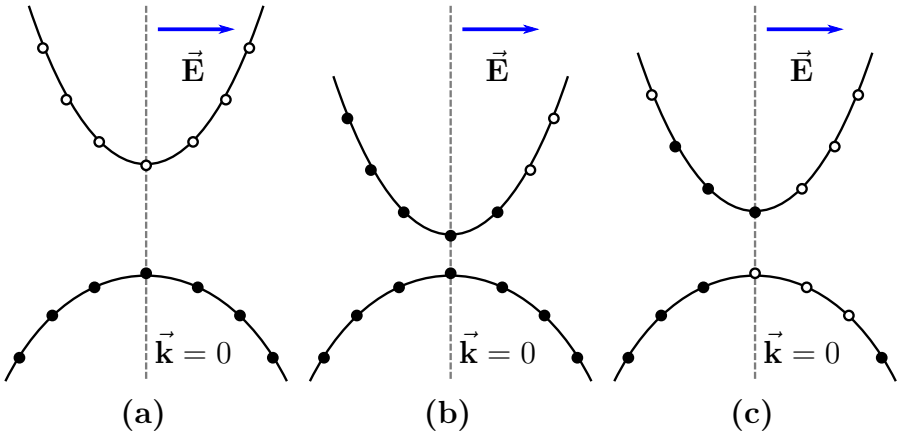

Figure 7: Schematic illustration of electrons in energy bands under an applied electric field for (a) an insulator, (b) a conductor and (c) a semiconductor. Black and white circles denote occupied and unoccupied electron states, respectively.

When a nearly filled band is considered (e.g. the valence band in a semiconductor), it is typically more convenient to consider the behavior of the relatively small number of vacant states as positively charged ($+q$) quasiparticles called holes. Holes relate to the corresponding missing electrons in a band such that the hole wave vector, energy and effective mass are obtained by taking the negative of corresponding electron

values: $\vec{\mathbf{k}}_\mathrm{h} = -\vec{\mathbf{k}}_\mathrm{e}$, $E_\mathrm{h}(\vec{\mathbf{k}}_\mathrm{h}) = -E_\mathrm{e}(\vec{\mathbf{k}}_\mathrm{e})$ and $m^*_\mathrm{h} = -m^*_\mathrm{e}$. The hole picture considers electrons as vacant hole states and hence, for each band, the current can either be considered to be carried by electrons or holes but not both. [**10**, p. 424–428] For conduction in semiconductors, it is typical to consider holes in valence band and electrons in conduction band.

The electrical conductivity σ is defined as the constant of proportionality between obtained current density $\vec{\mathbf{J}}$ and applied electric field as $\vec{\mathbf{J}} \equiv \sigma\vec{\mathbf{E}}$. For semiconductors, the conductivity can be written in the form

$$\sigma = q\mu_\mathrm{e} n + q\mu_\mathrm{h} p\,, \tag{7}$$

where q is the elementary charge, μ_e is electron mobility, n is electron concentration in conduction band, μ_h is hole mobility and p is hole concentration in valence band [**10**, p. 495]. The mobility is defined as the constant of proportionality between the drift velocity $\vec{\mathbf{v}}_\mathrm{g}$ (effective mean velocity of the charge carriers) and the applied electric field as $|\vec{\mathbf{v}}_\mathrm{g}| \equiv \mu_\mathrm{e,h}|\vec{\mathbf{E}}|$. Mobility is therefore a measure of how easily charge carriers can move in a crystal and (within the so-called relaxation time approximation) is related to the band structure and scattering as

$$\mu_\mathrm{e,h} = \frac{q\tau_\mathrm{e,h}}{m^*_\mathrm{e,h}}\,, \tag{8}$$

where $\tau_\mathrm{e,h}$ is the relaxation time (mean time between scattering events) and $m^*_\mathrm{e,h}$ is the effective mass. [**10**, p. 417–419] When the conduction in a macroscopic semiconductor crystal slab is considered, the conductivity relates to the measurable resistance R as

$$R = \frac{\rho l}{A} = \frac{l}{\sigma A} \tag{9}$$

where l is the slab length, A is the cross-sectional area and ρ is the resistivity (defined as the inverse of conductivity: $\rho \equiv \frac{1}{\sigma}$).

2.4 Intrinsic and extrinsic semiconductors

Semiconductors doped by electrically active impurities are called extrinsic while undoped semiconductors are called intrinsic. The purpose of the doping is to controllably increase the charge carrier concentration from the intrinsic case, which is achieved by introducing substitutional or interstitial impurity atoms that have different valence than the atoms of the host crystal. Those impurity atoms that can inject extra electrons to the conduction band are called donors and those that can capture electrons from the valence band (equivalent to injecting holes) are called acceptors. The dopant concentrations are denoted as N_D and N_A, respectively. Furthermore, semiconductors with donor doping have electrons as the majority charge carriers and are called n–type while acceptor doping leads to holes being the majority carriers and such semiconductors are called p–type. [**10**, p. 501]

Typically used dopants are substitutional and, for III–V compound semiconductors, this means that the type of the dopant can depend on which atom (group III or

V) it substitutes. For example, Zn is a group II element and has one valence electron less than Ga and two valence electrons less than As. Therefore, substitutional Zn dopants will act as acceptors in GaAs regardless of which atom they substitute. On the other hand, Sn is a group IV element and has one valence electron more than Ga but one less than As. Therefore, Sn can act as a donor when it substitutes a Ga atom and as an acceptor when it substitutes an As atom (such dopants are called amphoteric). In order for the dopants to inject electrons to the conduction band or holes to the valence band, the dopant energy levels need to be within the band gap of the semiconductor and sufficiently close to the conduction or valence band edges such that the dopants can be ionized by thermal energy. [**10**, p. 501–503]

In intrinsic semiconductors, charge carriers are generated when electrons are thermally excited from the valence to the conduction band. Therefore, for each electron in the conduction band there must be a corresponding hole left in the valence band and

$$n = p \equiv n_\mathrm{i}\,, \tag{10}$$

where n_i is the intrinsic carrier concentration [**10**, p. 490]. In order to simplify the picture, typically only one conduction band $E_\mathrm{c}(\vec{\mathbf{k}})$ and valence band $E_\mathrm{v}(\vec{\mathbf{k}})$ (separated by the band gap E_g) are considered. A further simplification is to reduce the bands to their corresponding edges at the band gap, as if the bands were flat in the $\vec{\mathbf{k}}$–space. This is illustrated in figure 8. This approximation requires that the Fermi level is sufficiently far away from the band edges in energy ($|E_\mathrm{c,v} - \mu_\mathrm{F}| \gg k_\mathrm{B}T$) and the states occupied by electrons and holes can be considered (in the vicinity of the band gap) to be free-electron-like [**10**, p. 492].

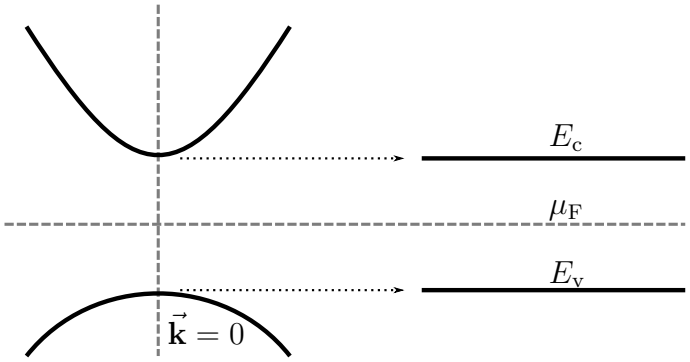

Figure 8: Schematic illustration of simplified semiconductor band structure in the vicinity of the band gap and its reduction to the band edges.

This simplified picture allows for succinct calculation of the carrier concentrations and the position of the Fermi-level. The charge carrier concentrations are obtained as

$$n = N_\mathrm{c} e^{-\frac{E_\mathrm{c}-\mu_\mathrm{F}}{k_\mathrm{B}T}} \tag{11}$$

and

$$p = N_\mathrm{v} e^{-\frac{\mu_\mathrm{F}-E_\mathrm{v}}{k_\mathrm{B}T}}\,, \tag{12}$$

where $N_c = 2\left(\frac{2\pi m_e^* k_B T}{h^2}\right)^{\frac{3}{2}}$ and $N_v = 2\left(\frac{2\pi m_h^* k_B T}{h^2}\right)^{\frac{3}{2}}$ are the effective densities of states for the reduced conduction and valence band, respectively, and h is the Planck constant. The intrinsic carrier concentration is obtained from equations 10, 11 and 12 as

$$n_i = \sqrt{N_c N_v} e^{-\frac{E_g}{2k_B T}} \tag{13}$$

and the position of the Fermi level can be solved as

$$\mu_F = E_v + \frac{1}{2}E_g + \frac{3}{4}k_B T \ln\left(\frac{m_h^*}{m_e^*}\right). \tag{14}$$

Therefore, for intrinsic semiconductors, the Fermi-level is in the middle of the bandgap at $T = 0$ K or if the bands are symmetric ($m_e^* = m_h^*$). Furthermore, the intrinsic carrier concentration of equation 13 does not depend on the position of the Fermi level and is actually equally valid in the extrinsic case. [**10**, p. 492–495]

In extrinsic semiconductors, the dopants contribute charge carriers to the system and much higher carrier concentrations may be obtained than in the intrinsic case. However, as both the dopant ionization and the intrinsic carrier generation are thermally activated, there exist three distinct temperature régimes for the carrier concentration: freeze-out, saturation and intrinsic-like. In the freeze-out régime, the temperature is low enough such that only part of the dopants are ionized, i.e. $n < N_D$ (or $p < N_A$). In the saturation régime, practically all the dopants are ionized and $n \approx N_D$ (or $p \approx N_A$). In the intrinsic-like régime, the temperature is so high that the thermally generated intrinsic carrier concentration exceeds the dopant concentration and the semiconductor behavior reverts to the intrinsic case. Typically, normal temperatures (e.g. room temperature) correspond to the saturation régime due to the relatively low energy required to ionize dopants. In this case, the Fermi-level for an n–type semiconductor is

$$\mu_F = E_c - k_B T \ln\left(\frac{N_c}{N_D}\right) \tag{15}$$

and for a p–type semiconductor

$$\mu_F = E_v + k_B T \ln\left(\frac{N_v}{N_A}\right). \tag{16}$$

Therefore, the Fermi level is close to the conduction band edge and valence band edge for n-type and p-type doping, respectively. [**10**, p. 506–510]

2.5 Metal–semiconductor junction

An electrical contact between a metal and a semiconductor can exhibit one of three different types of current–voltage behavior called ohmic, blocking and injecting. In an ohmic contact, the current across the junction depends linearly on the voltage over the junction. Blocking behavior in a contact results if it can't replenish the charge being extracted from the semiconductor under an applied electric field (voltage). Injecting behavior means that the applied field causes extra charge to be injected

to the semiconductor instead. Therefore, it becomes progressively harder for the current to increase with the voltage in a blocking contact and easier in an injecting contact. [**10**, p. 694]

In the absence of an electric field charge will flow across the junction until the chemical potentials have been equalized at the junction. The factor that determines whether the contact is ohmic or blocking is the relative difference between the metal and semiconductor work functions. The work function for a material is defined as

$$\Phi \equiv E_{\text{vac}} - \mu_{\text{F}} \,, \tag{17}$$

where E_{vac} is the vacuum energy level. If an n–type semiconductor forms a contact with a metal of smaller work function ($\Phi_{\text{S}} > \Phi_{\text{M}}$) electrons will flow from the metal to the semiconductor and the resulting charge imbalance generates an electric field that bends the semiconductor bands down. The result in this case is an ohmic contact. If $\Phi_{\text{S}} < \Phi_{\text{M}}$ instead, electrons will flow from the semiconductor to the metal leaving behind a depletion layer of exposed ionized donors. The electric field forms in the opposite direction in this case and the semiconductor bands bend upwards accordingly. This results in a Schottky barrier at the interface and the contact is blocking. Figure 9 shows schematic band pictures of the ohmic and blocking contact for an n–type semiconductor. For a p–type semiconductor, the work function difference criteria for ohmic or blocking contact are reversed. [**10**, p. 695–696]

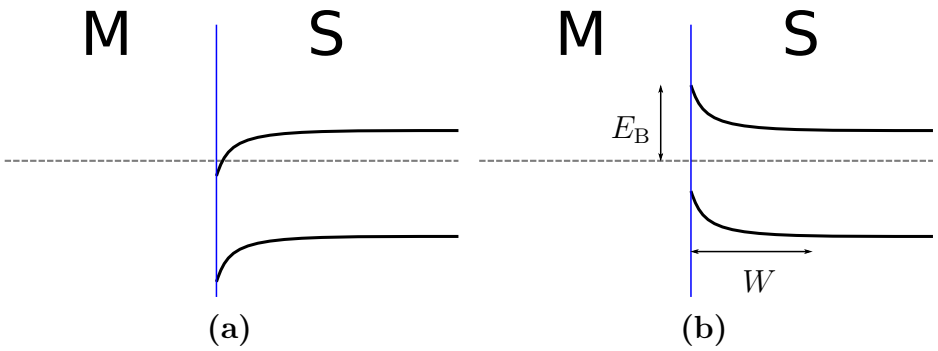

Figure 9: Schematic band pictures of (a) ohmic and (b) blocking metal–semiconductor contacts for an n–type semiconductor. The Schottky barrier E_{B} and depletion width W are also marked.

As a first approximation, the Schottky barrier height (for an n–type semiconductor) is given as

$$E_{\text{B}} = \Phi_{\text{M}} - \chi_{\text{S}} \,, \tag{18}$$

where $\chi_{\text{S}} = E_{\text{vac}} - E_{\text{c}}$ is the semiconductor electron affinity. However, this dependence is rarely seen experimentally. One of the effects resulting in Schottky barrier height to deviate from that of equation 18 is Fermi level pinning. If there exists a high enough density of interface states within the band gap at the junction, the Fermi level can be approximately pinned to a particular energy (e.g. in the middle of the band gap) despite the flow of electrons to the interface. The interface states can form, for example, as metal-induced gap states when the junction is formed. [**10**, p. 696–699]

When an external electric field is applied over the junction, the chemical potential (Fermi level) is no longer constant across the junction, but instead the electrochemical potential is. The electrochemical potential is obtained as

$$\eta = \mu_{\mathrm{F}} - qV\,, \tag{19}$$

where q is the elemental charge and V is the applied voltage. The electric field also bends the semiconductor bands by qV, which is illustrated in figure 10 for a blocking contact to an n–type semiconductor. This also affects the width of the depletion region. [**10**, p. 699]

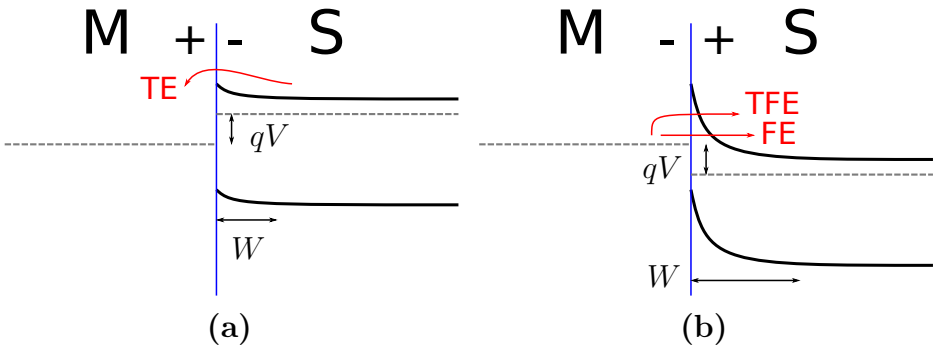

Figure 10: Blocking contact to an n–type semiconductor under an applied voltage in (a) forward-bias and (b) reverse-bias. Electrostatic potential difference qV and depletion region width W are also marked and carrier transport through the metal–semiconductor interface via TE, FE and TFE mechanisms are indicated.

In the case of a blocking contact with a Schottky barrier, a larger current will flow in the forward-bias, i.e. when the applied voltage reduces the energy barrier by qV in the semiconductor–metal direction. On the other hand, the bias does not affect the barrier height in the reverse direction and therefore the reverse bias current is very small in comparison. This leads to the typical rectifying behavior of Schottky contacts. However, if the barrier is thin enough, electron transport can take place via tunneling through the barrier (field emission, FE) instead of thermionic emission (TE) over it. For example, high doping in the semiconductor can lead to a thin barrier and a low-resistance quasi-ohmic contact with approximately the same magnitude of current for both polarities of applied voltage. [**10**, p. 699–700] In addition to TE and FE, carrier transport through a metal–semiconductor interface can take place via thermionic-field emission (TFE) in which thermally excited carriers tunnel through a thinner barrier [**13**, **14**]. These mechanisms are also indicated in figure 10.

2.6 MISFET

A MISFET is a device that consists of a drain, source and gate. In conventional planar MISFET devices, the drain and source are highly doped regions in the semiconductor substrate which, in turn, has low and opposite doping. The gate is a metal electrode that is positioned between the drain and source areas and is separated from the

substrate by a thin insulator layer. The operation of the MISFET structure is based on the forming and conductivity modulation of a channel in the semiconductor region between the drain and source when a voltage is applied to the gate electrode. The device is hence basically a voltage controlled resistor. [**10**, p. 732] The conventional MISFET structure is schematically illustrated in figure 11a.

The gate voltage causes the conduction and valence bands in the semiconductor to bend at the insulator–semiconductor interface such that the majority carriers are repelled away from the interface. When the gate voltage reaches the threshold voltage, the band bending causes the Fermi level to go inside one of the bands and an inversion layer is formed. This degenerate inversion layer forms the conductive channel and the carrier concentration can be further increased by increasing the gate voltage. Positive gate voltage and p–type doped substrate will lead to an n–type channel while negative gate voltage and n–type doped substrate will lead to a p–type channel. [**10**, p. 706–707] Figure 11b shows a schematic band diagram illustrating this effect.

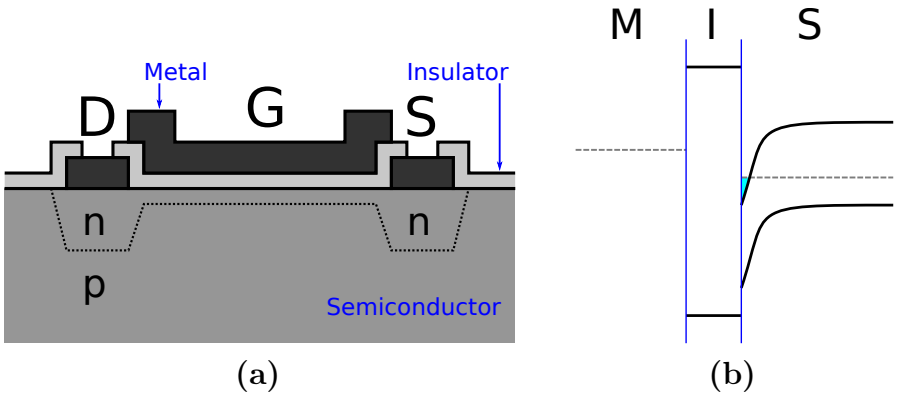

Figure 11: Schematic illustration of the (conventional) planar MISFET device structure (a) and channel formation due to band bending (b).

A simple model considering the current–voltage relationships in the described MISFET device gives the drain–source current of an n–channel device as

$$I_\mathrm{D} = \frac{\mu_\mathrm{e} C_\mathrm{gl}}{L_\mathrm{ch}} \Big(V_\mathrm{GS} - V_\mathrm{th} - \frac{1}{2} V_\mathrm{DS} \Big) V_\mathrm{DS} \tag{20}$$

and p–channel device (all current and voltage polarities are reversed and V_th is negative) as

$$I_\mathrm{D} = -\frac{\mu_\mathrm{h} C_\mathrm{gl}}{L_\mathrm{ch}} \Big(|V_\mathrm{GS}| - |V_\mathrm{th}| - \frac{1}{2} |V_\mathrm{DS}| \Big) |V_\mathrm{DS}| \,, \tag{21}$$

where $\mu_\mathrm{e,h}$ is the mobility in the channel, C_gl is the gate capacitance per unit length, L_ch is the channel length and V_GS, V_DS and V_th are the gate–source, drain–source and threshold voltage, respectively. These equations are only valid if $V_\mathrm{GS} \geq V_\mathrm{th}$ and $V_\mathrm{DS} \leq V_\mathrm{GS} - V_\mathrm{th}$. [**15**, p. 40–46] Furthermore, if V_DS is very small, equation 20 becomes approximately

$$I_\mathrm{D} \approx \frac{\mu_\mathrm{e} C_\mathrm{gl}}{L_\mathrm{ch}} \Big(V_\mathrm{GS} - V_\mathrm{th} \Big) V_\mathrm{DS} \,, \tag{22}$$

which is linear with respect to both V_{GS} and V_{DS} (this applies to equation 21 as well). Regardless, the transconductance, defined as $g_{\mathrm{m}} \equiv \frac{\partial I_{\mathrm{D}}}{\partial V_{\mathrm{GS}}}$ [**15**, p. 87], is simply

$$g_{\mathrm{m}} = \frac{\mu_{\mathrm{e,h}} C_{\mathrm{gl}}}{L_{\mathrm{ch}}} |V_{\mathrm{DS}}| \,, \tag{23}$$

which directly depends on the mobility, capacitance and V_{DS} voltage.

In conventional MISFET devices, the source and drain series resistances R_{S} and R_{D} are typically relatively small and can be mostly ignored at low drain currents [**15**, p. 77]. If the series resistances are not negligible, however, the measurable drain–source voltage $V_{\mathrm{DS,meas}}$ includes voltage drops from these resistances

$$V_{\mathrm{DS,meas}} = V_{\mathrm{DS}} + V_{\mathrm{RS}} + V_{\mathrm{RD}} = V_{\mathrm{DS}} + (R_{\mathrm{S}} + R_{\mathrm{D}}) I_{\mathrm{D}} \tag{24}$$

and the gate–source voltages includes voltage drop from the source resistance

$$V_{\mathrm{GS,meas}} = V_{\mathrm{GS}} + V_{\mathrm{RS}} = V_{\mathrm{GS}} + R_{\mathrm{S}} I_{\mathrm{D}} \,. \tag{25}$$

Therefore, the measurable (apparent) transconductance $g_{\mathrm{m,meas}} \equiv \frac{\partial I_{\mathrm{D}}}{\partial V_{\mathrm{GS,meas}}}$ is different from the actual transconductance. Furthermore, the actual transconductance is no longer given by the equation 23 since the V_{DS} depends on I_{D}. In nanowire devices, the metal contacts can result in significant contact resistances (as will be discussed in section 3.3) which implies non-negligible source and drain series resistances for nanowire FETs.

3 Nanowire theory

Due to their dimensionality, nanowires pose more challenges than planar microfabricated structures made from the same semiconductor material. Firstly, the one-dimensional nature of the epitaxial nanowire growth requires a more complicated process than normal planar epitaxy. One way to achieve such growth is via the VLS mechanism which is employed in this work and presented in section 3.1. Secondly, regardless of the growth process, nanowires may suffer from surface related effects and difficulties in making good electrical contacts. Both of these issues have significant implications for conducting electrical measurements on nanowires and are therefore discussed in sections 3.2 and 3.3, respectively.

3.1 Nanowire VLS growth

All the nanowires in this work were grown on Si substrates with the MOVPE technique via the VLS mechanism. The MOVPE precursor materials used in this work were trimethylgallium, tertiarybutylarsine, diethylzinc and tetraethyltin (abbreviated in this thesis as TMGa, TBAs, DEZn and TESn, respectively). In VLS nanowire growth, small seed particles act to substantially increase the growth rate in one direction while the growth conditions are selected such that planar growth is kinetically hindered on both the substrate surface and the nanowire side facets. The seed particles can be of foreign material or droplets of one of the growth components. Selective area nanowire growth takes place under the seed particles such that the particles get lifted in the process and the diameter of the nanowire is set by the seed diameter (save for planar growth). Although the seed particles are essential in the VLS mechanism, they do not directly participate in the growth and are normally not consumed. [**1**, p. 143–144] Au is a conventional choice for a seed particle as most early work focused on this material [**1**, p. 144]. On the other hand, Au can be an undesirable contaminant in semiconductor processing and alternative seed particle metals have also been investigated (e.g. 15 period III to VI metals in [**16**]). In this work, only Au nanoparticle seeds were used.

The VLS mechanism was first proposed by Wagner and Ellis [**17**] to explain the growth of Si whiskers below small Au particles on a Si substrate. According to this model, the Au particle and Si substrate form a (stable) liquid alloy at high temperatures and it is a preferred site for deposition from the vapor. This is due to the liquid alloy acting either as a preferred sink for arriving Si atoms or as a catalyst for the Si containing vapor phase precursor molecule decomposition. The Au particle thus becomes supersaturated (has thermodynamically unstable composition) with Si. Solid Si then starts to precipitate from the alloy and nucleates on the substrate below the particle leading to crystal growth at the particle–whisker interface and the particle is hence lifted up.

The heteroepitaxial VLS growth of GaAs nanowires on Si, however, is a more complicated process as there are two growth components instead of one and neither of them are of the same material as the substrate. Furthermore, the original model for the VLS mechanism is, in general, not sufficient. First, epitaxial growth is

discussed in section 3.1.1. The VLS mechanism and effect of growth conditions are then further discussed in sections 3.1.2 and 3.1.3, respectively. These specifically consider Au-assisted growth of GaAs nanowires in MOVPE, unless stated otherwise. The addition of dopant precursors for in situ doping further complicates the growth process. Doping during the growth and its implications are discussed in section 3.1.4. It should be noted that these are vast and complex topics and the discussion given here is by no means exhaustive.

3.1.1 Epitaxial growth

Epitaxy means the formation of single-crystalline material on top of a single-crystalline substrate such that the structure and orientation of the forming crystal depend on those of the substrate. Typically, a distinction is made between the cases when the epitaxially grown material is the same as that of the substrate and when the two are of different materials. The former is called homoepitaxy while the latter is called heteroepitaxy. The growing layer is called an epilayer. Thermodynamically, the requirement and driving force for the crystal growth, whether epitaxial or not, is the chemical potential difference of the growth components in the source and in the growing solid crystal phase. The chemical potential of the growth components depends on their partial pressure (or concentration) in a system. In order for the growth to take place, the chemical potential needs to be lower in the crystal phase. [**1**, p. 145–146] For example, in liquid phase epitaxy the source is a supersaturated melt which is in excess of the growth material compared to the equilibrium concentrations. This excess material (in solid phase) precipitates from the melt to the crystal growing on top of the substrate. [**18**, p. 453–454] In vapor phase epitaxy the growth material precipitates from a supersaturated vapor phase instead and MOVPE is a subset of this technique [**1**, p. 146].

When atoms precipitate from the supersaturated phase to the growth interface they can be incorporated to the growing crystal. The atoms will first adsorb to the surface of the substrate or the epilayer. These adatoms can then diffuse along the surface until they find a bonding location in the crystal that is energetically favorable. Such favorable locations have more neighboring atoms with which the adatom can form bonds with. In addition to surface diffusion, an adatom can alternatively be exchanged with another already bound atom. It is also possible that an adatom desorbs back to the supersaturated phase before finding a more stable binding location. [**10**, p. 168–171]

In the case of heteroepitaxy, it is the more difficult for the epilayer to conform to the substrate crystal structure the larger the lattice constant difference is between the two. This lattice mismatch (or misfit) is defined as

$$f_{\mathrm{m}} = \frac{a_{\mathrm{S}} - a_{\mathrm{L}}}{a_{\mathrm{L}}} \tag{26}$$

where a_{S} and a_{L} are the lattice constants of the substrate and the epilayer, respectively. In order to accommodate the lattice mismatch, the crystal and substrate lattices will strain; negative f_{m} leads to compressive and positive f_{m} to tensile stress in the

epilayer and the opposite for the substrate. [**18**, p. 423–424] As long as the lattices strain to accommodate the mismatch the growth is called pseudomorphic. However, at a certain point it becomes more energetically favorable for dislocation defects to form at the interface relaxing the strained epilayer. The epilayer thickness at this point is called the critical thickness and it depends on the lattice mismatch. When the layer thickness further increases, more misfit is relieved by dislocations. [**18**, p. 418–419, 429] Lattice mismatch is schematically illustrated in figure 12.

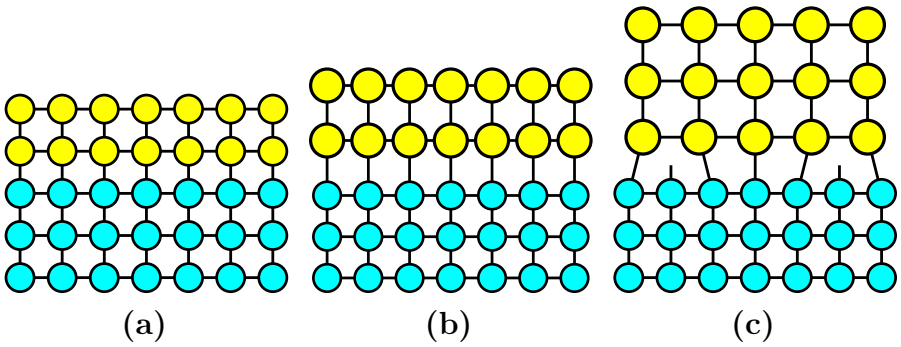

Figure 12: Schematic illustration of epitaxial layers in the case of (a) lattice matching, (b) lattice mismatch and strain accommodation (c) lattice mismatch and relaxation by dislocations.

Since dislocation defects deteriorate the properties of the grown epilayer, the critical thickness poses a limitation for planar epitaxial growth. Unlike thin films, nanowires have only limited extent (diameter) on the substrate surface and permit effective strain relaxation without the forming of defects. Therefore, lattice-mismatched epitaxial growth of III–V nanowires on Si is possible without compromising the crystal quality. [**19**] Critical diameters in VLS grown III–V nanowires have been reported to exhibit inverse dependence on the lattice mismatch and also assumed to vary with used growth conditions [**20**]. Furthermore, in nanowires with segments of dissimilar materials, heteroepitaxial axial growth also exhibits larger critical thickness (length) of the grown segment than in corresponding planar heteroepitaxy with the same materials. When the nanowire diameter is small enough, the critical thickness (length) can become infinite. [**21**]

3.1.2 VLS mechanism

The VLS growth of III–V nanowires is not fully understood but thermodynamics, kinetics, physical surface processes as well as chemical reactions involving the vapor phase precursors should all be considered [**1**]. In general, the following processes take place during the growth: (i) vapor phase precursors are constantly supplied to the reactor, (ii) the precursors decompose and growth material atoms adsorb on the Au particle, nanowire or substrate, (iii) group III adatoms dissolve to the Au particle, (iv) excess material precipitates from the particle to the growth interface, (v) group III and V adatoms diffuse along surfaces (for one diffusion length on average), (vi) adatoms desorb back to vapor, (vii) diffusing adatoms reach the particle–nanowire

interface, (viii) the group III and V material reaching the growth interface nucleate there and contribute to the crystal growth and (ix) planar radial growth due to those adatoms that neither reach the particle nor desorb to vapor. [**1**, **22**] The processes i–ix are illustrated in figure 13. The group III adatoms generally have larger diffusion lengths than group V adatoms, for which desorption back to vapor is likely to occur [**23**].

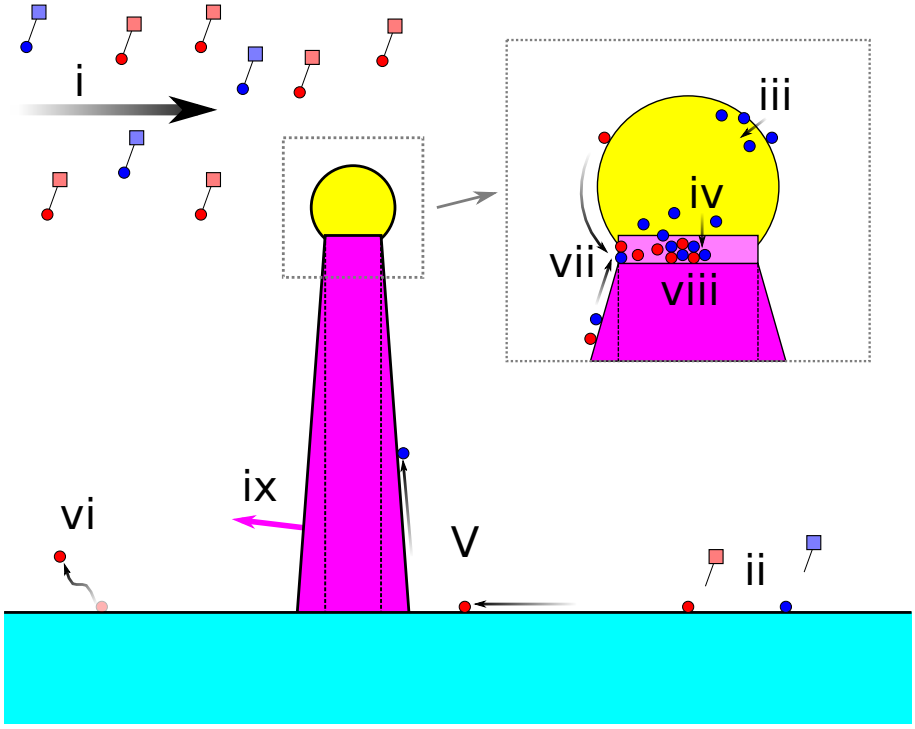

Figure 13: Processes taking place in Au-assisted VLS growth in MOVPE: (i) constant vapor phase precursor supply flow, (ii) precursor decomposition and growth material adsorption on surfaces, (iii) group III adatoms dissolve to the particle, (iv) excess material precipitates from the particle to the growth interface, (v) group III and V adatoms diffuse along surfaces, (vi) adatoms desorb back to vapor, (vii) adatoms reach the particle–nanowire interface, (viii) nucleation and nanowire crystal growth and (ix) radial growth. Blue and red circles denote group III and V atoms, respectively and circles attached to squares denote precursor molecules.

As already mentioned, chemical potential difference is the thermodynamical driving force for the growth; the growth material can only be incorporated from the vapor phase (decomposed precursors) to the particle and from the particle to the growing nanowire crystal, if the material has higher chemical potential in the vapor than in the particle and again higher in the particle than in the nanowire. This means that the chemical potential difference must be larger between vapor and nanowire than particle and nanowire. The growth would hence actually occur faster directly from the vapor. However, this is the case only if compositions everywhere are uniform. Due to the growth kinetics, like adatom diffusion or preferential precursor decomposition at the nanoparticle, the local concentration of growth material around

the particle may be increased, thus making the chemical potential differences locally higher than the vapor–crystal difference elsewhere. [**1**, p. 151]

It has been argued that the Au particle may, in some systems, act as a catalyst lowering the activation energy of precursor decomposition, although that is not a general effect in VLS [**1**, p. 151–153]. For Au-assisted GaAs growth in MOVPE, there are reports in which the obtained activation energies for axial and planar growth were found to show no significant difference suggesting that Au particles did not act as catalysts in those systems [**24**, **25**]. Furthermore, GaAs nanowires have been grown by Au-assisted VLS via molecular beam epitaxy technique, in which the vapor consists of elemental Ga and As and there is no thermally activated precursor decomposition to be catalyzed [**1**, p. 153].

The Au particle could, however, act as a sink, effectively collecting the group III adatoms that readily diffuse along the substrate and nanowire surfaces and dissolve into the particle [**25**]. The group V component As, on the other hand, dissolves to Au in significant quantities only at temperatures much higher than those used for GaAs nanowire growth in MOVPE. Therefore, there exists no stable ternary Au–Ga–As or binary Au–As alloys and the As atoms rather reach the growth interface by diffusion along the particle–nanowire interface. Moreover, it might be possible that precursors have higher accommodation coefficient in the liquid particle and this effect contributes to the VLS nanowire growth. [**1**, p. 152, 154]

For most nanowire materials and growth systems the seed particle forms a liquid alloy but in some cases nanowire growth occurs also under conditions in which sold particles are expected, implying the so called vapor–solid–solid (VSS) growth [**1**, p. 154–156]. For example, Johansson et al. [**25**] not only demonstrated successful MOVPE growth of InAs and InP nanowires at such temperatures where the Au seed particles were solid but also that the growth failed at temperatures required for liquid alloys. However, Au nanoparticles have been found to exhibit melting point depression with decreasing particle diameter as well as hysteresis in melting and solidification temperatures. Small diameter Au nanoparticles can even reshape under relatively low temperatures while still maintaining their crystalline structure. Therefore, it is not easy to determine the actual state of a particle under given conditions. Nevertheless, VLS and VSS mechanisms are considered similar and both valid for nanowire growth. [**1**, p. 154–156]

Some models of the VLS mechanism suggest that the most important factor for one-dimensional growth is the preferential nucleation of material at the particle–nanowire interface as compared to elsewhere on the nanowire or substrate surface. This would also mean that the phase of the seed particle is less critical and the same considerations could apply to the VSS case as well. [**1**, p. 156–157] For example, according to the model of Joyce et al. [**11**], Au-assisted VLS growth of III–V nanowires proceeds by repeated nucleation at the three-phase contact line and bilayer growth propagation over the particle–nanowire interface. Each nucleus creates a new external vapor–nucleus facet at the three-phase contact line tending for facets with the lowest surface energy. Therefore, change of which facets have the lowest surface energy, e.g. due to varying temperature and V/III ratio, can lead to twinning, changes in growth direction (kinking) and altering between ZB and WZ

crystal structures [**11**]. It has further been suggested in [**26**] that such morphological phenomena, including nanowire growth along the substrate (crawling), result from the interplay of facet growth, particle droplet statics, and the introduction of new facets at the three-phase contact.

Nanowire VLS growth has also been successfully conducted inside a transmission electron microscope (TEM) and this has provided additional insight on the growth process. For example, Chou et al. [**23**] examined the local kinetics of Au-assisted GaP nanowire growth in situ as each atomic plane was added at the particle–nanowire growth interface and they observed fluctuations in growth rate, even under steady growth conditions with high V/III ratio. Wen et al. [**27**], in turn, suggested that a non-planar growth interface with truncated edges is a general phenomenon for growth of III/V nanowires in the standard $\langle 111 \rangle$ direction.

3.1.3 Effect of growth conditions

The VLS growth of nanowires in MOVPE is a complex and delicate process in which altering growth conditions can lead to vastly different results. Important parameters affecting the growth include temperature, V/III ratio (ratio of the reactant species in moles inside the reactor), group III and V precursor (molar) flow rates, seed particle diameter and density as well as substrate material and preparation. Of these parameters, the temperature, V/III ratio and precursor (molar) flow rates are readily tunable in MOVPE and therefore used to control the growth. The pressure inside the MOVPE reactor, although generally left unaltered, should also be considered as a growth parameter as it can e.g. affect the state of the seed particle [**1**, p. 156].

Nanowires can only grow within a limited temperature range specific for each growth system. Since the VLS mechanism requires that the planar growth is kinetically hindered, the upper temperature limit is dictated by the onset of planar growth. For example, for GaAs growth on GaAs substrate, this is around 480 – 500 °C. [**24**] The lower temperature limit for successful nanowire growth is not so clear but depends on the various thermally activated processes. For example, without precursor decomposition the growth cannot take place. It has been proposed that the minimum temperature required for stable well-oriented growth corresponds to obtaining suitable nanoparticle–substrate interface conditions and liquid nanoparticle state during the growth initiation [**28**].

Temperature further has a significant effect on nanowire morphology, growth rate and crystal structure. For example, tapering is reduced at lower growth temperatures. Since radial growth is kinetically limited, diffusing adatoms are less likely to be incorporated into nanowire sidewalls at lower growth temperatures and decreasing the temperature also decreases adatom diffusion length reducing the flux of adatoms from the substrate to the nanowire. Both of these effects work to reduce nanowire tapering. [**28**]

The temperature dependence of axial growth rate of nanowires in MOVPE depends on the growth-limiting factor. If the growth is thermodynamically limited (crystallization is the limiting step), growth rate decreases with temperature and if chemical reactions (precursor decomposition) are limiting, the growth rate typically

increases with temperature. However, if mass transport (movement of material through the gas phase towards the growth interface) is the limiting factor, the growth rate is mostly temperature independent. [**1**, p. 147] GaAs nanowire growth is typically chemical reaction limited and the growth rate hence tends to increase with temperature until the onset of planar growth [**1**, p. 160].

Although temperature affects the crystal structure of growing nanowires, it is just one of the relevant parameters and the structure results from the interplay involving all of them. For example, as already mentioned, changes in temperature and V/III molar ratio can affect the surface energies for new external vapor–nucleus facets. A combination of low growth temperature and high V/III ratio can lead to reduced stacking fault density [**29**] or even pure ZB nanowires [**11**]. Conversely, high temperatures and low V/III ratio have been used to produce pure WZ nanowires [**11**].

Two-temperature processes have been used in order to grow GaAs nanowires with high quality and minimum tapering. For example, Joyce et al. [**28**] grew GaAs nanowires on GaAs substrates via Au-assisted VLS in MOVPE. In this process, the growth is initiated with a brief high-temperature step which allows for obtaining suitable initial conditions leading to epitaxial nucleation and straight vertically aligned growth. The temperature is then rapidly ramped down to the desired low value for the prolonged growth step. The low temperature is able to maintain the straight epitaxial growth as long as the necessary conditions are established during the growth initiation. In addition to reduced tapering and stacking fault density, the low growth temperature has been found to result in enhanced nanowire optical quality [**28**]. Similar two-temperature processes have also been successfully used to grow doped GaAs nanowires [**30**, **31**].

The V/III ratio can have significant impact on nanowire crystal structure and growth rate. Typically, group V precursors are in excess in order to avoid homogeneous nucleation of group III species [**1**, p. 161] and high V/III ratios are employed. However, high V/III ratios have been reported to, for example, both decrease planar defect density [**11**, **28**, **29**, **32**] and instigate kinking and increase tapering [**32**]. Furthermore, the activation energy of precursor decomposition has been found to decrease with V/III ratio indicating that the decomposition of the precursors is affected by the presence of both species [**1**, p. 161]. Again, the entire growth system needs to be considered in order to find optimal values for the V/III ratio (or any other parameter).

The molar flows of the group III and V precursors affect the availability of growth components as well as the supersaturation. When the nanowire axial growth is mass transport limited, the growth rate increases with increasing group III and V flows – or just group III flow if there is already an abundance of group V species. This also reduces nanowire tapering since the radial growth rate, being kinetically limited, increases only marginally. [**33**] Furthermore, increasing both group III and V flows, while maintaining a constant V/III ratio, has been reported to result in reduced twin defect density in GaAs nanowires [**33**, **34**]. This effect may have resulted from As and Ga precursor species acting to reduce surface and interface tensions at the triple phase line that drive twin defect formation [**33**].

The seed particle diameter not only dictates the nanowire diameter but also has an effect on the growth. The nanowire growth rate typically decreases with increasing seed particle diameter since the growth interface scales faster with growing nanowire radius ($\propto r_{\mathrm{nw}}^2$) than the side facet area over which adatoms are collected by diffusion ($\propto r_{\mathrm{nw}}$) [**1**, p. 163]. However, for small diameter seed particles, the nanowire growth is affected by the Gibbs–Thomson effect in the particle (increasing reactant pressure the smaller the size) and the growth rate actually increases with increasing radius [**22**, **25**]. For larger seed particles and under high supersaturation, the Gibbs–Thomson effect can be neglected [**25**]. The diameter dependence of growth of GaAs nanowires in MOVPE is also dependent on the V/III ratio [**1**, p. 164]. Furthermore, based on previous reports, it was concluded in [**11**] that nanowires with small and large diameters tend toward WZ and ZB crystal structure, respectively.

When the seed particle density is high enough it can lead to growth material competition between neighboring nanowires as their collection areas for diffusing adatoms overlap. This competition then results in reduced growth rate for the nanowires. Conversely, when the seed particle density is low (interwire separation is large compared to diffusion) the nanowires grow independently. [**1**, p. 164] However, Borgstroḿ et al. [**35**] observed an additional "synergetic" régime for MOVPE growth of InAs and GaAs nanowires in which the growth rate was enhanced when the collection areas for neighboring wires did not overlap but the wires were still in relatively close proximity. This effect was attributed to nanowire interaction through gas-phase diffusion such that the catalyzed decomposition of the Ga precursor on the Au alloy surface led to a locally enhanced vapor pressure of partially decomposed species which could then diffuse to a neighboring wire and contribute to its growth.

The substrate can also affect the growth conditions. For example, a Si (111) substrate has been found to reduce the activation energy for nanowire growth as compared to a GaAs substrate, possibly due to enhanced pyrolysis rate of the precursors at low temperatures (when the pyrolysis rate is less than 100 %) [**29**]. Furthermore, substrate preparation, including cleaning and native oxide removal steps, can significantly improve the yield of vertically grown epitaxial nanowires. For example, both buffered oxide etch and HF solutions were used in [**29**] to remove the native oxide and form a hydrogen-terminated surface. It was found that the buffered oxide treatment resulted in higher yield of vertical nanowires, possibly due to producing flatter Si surface.

Finally, the collection area for diffusing adatoms (dictated by the finite diffusion length) changes over time and can hence induce time dependence to the growth rate. Initially, the diffusing adatoms are mainly collected from the substrate surface, but as the nanowire grows in height, the overall collection area shrinks as the adatoms are mainly collected from the nanowire side facets. When the nanowire height becomes larger than the diffusion length, adatoms are only collected from the side facets and the collection area becomes constant. It should be noted that this mainly concerns the group III species that, as already mentioned, have typically longer diffusion lengths than group V species. [**1**, p. 162–164]. However, these effects can be rather minor as the axial growth rate has been considered to be constant after the initial nucleation [**29**, **36**].

3.1.4 Doping during the growth

For in situ doping in MOVPE, additional dopant precursor gas flow is added during the normal growth sequence and the dopants can be incorporated to the growing nanowire similarly to the actual growth components. The doping concentration is controlled by varying the precursor molar flow compared to the growth component precursors, e.g. the II/III ratio of DEZn and TMGA or IV/III ratio of TESn and TMGA in p- and n-type doping of GaAs, respectively. It should be noted, however, that the doping concentration is not necessarily equal to the molar ratio in the vapor phase since the diffusion lengths, decomposition rates and sticking coefficients may be significantly different for the dopant and the growth precursor [**8**]. For example, DEZn is already completely pyrolyzed at 400 °C whereas TMGa is only partially decomposed even at 450 °C. The effective II/III ratio may therefore differ significantly from the actual II/III ratio and possibly varies with the used growth temperature. [**37**] In the case of amphoteric dopants, the incorporation site, and hence the type of doping, can critically depend on the used V/III ratio and the seed particle solubilities of the different species. Despite the apparent difficulties, controlled doping and similarly high doping levels as in corresponding thin films would seem possible. [**8**]

The dopants can get incorporated in the nanowire either via the VLS mechanism through the seed particle, via diffusion to and along the particle–nanowire interface, via incorporation in the radial overgrowth or via diffusion through the side facets. Dopant incorporation via radial growth is likely adequately described by thin-film growth models, although unusual side facets and lower growth temperatures need to be taken into account. Furthermore, nanowires have a large surface-to-volume ratio which can influence the dopant incorporation. Even in the absence of radial growth, it might be energetically favorable for dopants to segregate to the surface states which also leads to a highly doped shell compared to the bulk. This effect is more pronounced for small diameter nanowires. [**8**] However, doping by diffusion into the nanowire is less likely to be significant. For example, DEZn has been found to cause no significant doping effect via diffusion through the side facets and Zn diffusion within GaAs nanowires during the growth should be negligible [**30**].

Wallentin and Borgström [**8**] presented a simplified model for dopant incorporation via the seed particle. This model assumes that the doping at the particle–nanowire interface is locally akin to doping in normal liquid phase epitaxy system and considers steady state growth with dopant concentration c_P in the particle and c_W in the nanowire and fluxes J_{VP} from vapor to particle, J_{PV} from particle to vapor (re-evaporation) and J_{PW} from particle to wire. Dopants are then classified to two types based on their solubility in the seed particle and particle-to-wire segregation coefficient κ. Type A dopants have low solubility to the particle but high segregation coefficient, therefore leading to low concentration in the particle with negligible re-evaporation. Type B dopants, on the other hand have high solubility in the particle and low segregation coefficient leading to relatively high concentration in the particle. In the case of type A dopants, the fluxes J_{VP} and J_{PW} are almost equal, whereas for type B dopants, the segregation coefficient determines the incorporation to the nanowire ($c_W = \kappa c_P$). Regardless of the type, diffusion of dopants through a

liquid seed particle to the growth interface is expected to be fast and should therefore not be a limiting factor [**8**].

The incorporation of dopants in the seed particle has implications on, for example, achieving uniform doping or sharp doping gradients. For this purpose, type A dopants would be preferred in order to speed up dopant saturation and to reduce the memory effects in the seed particle [**8**]. However, both Zn and Sn seem to rather be type B dopants. For example, Gutsche et al. [**30**] observed a delayed Zn incorporation in Au seed particles, possibly due to slow Au particle saturation with Zn. This led to intrinsic nanowire feet up to several microns and even to doping gradients across the whole wire length with low DEZn supply. Similar effect was also observed with Sn doping of GaAs nanowires using TESn as precursor [**31**]. Furthermore, the memory effects in the MOVPE reactor can also limit the achievable sharpness in doping gradients when changing dopant supplies [**8**]. Despite this, pn-diodes in a single GaAs nanowire using DEZn and TESn as precursors have been successfully demonstrated [**38**]. Additionally, pre-saturating the Au seed particle with dopants prior to growth can somewhat alleviate the gradient problem by resulting in less axially extended doping profiles [**37**].

In addition to intentional doping, unintentional impurity doping can also take place. In MOVPE, the main source of unintentional doping is carbon atoms coming from the decomposed organometallic precursors [**33**] and incorporation of these carbon impurities mostly leads to p-type background doping [**38**]. Furthermore, higher temperatures leading to additional planar growth on the nanowire side facets facilitates carbon incorporation in the growing shell [**38**].

The effects of doping on nanowires are often much stronger than in thin-film growth and can have similarly strong influence on e.g. growth rate and crystal structure as changes in growth parameters like V/III ratio [**8**]. Indeed, Zn doping has been demonstrated to e.g. promote ZB growth of InP nanowires with tunable twinning superlattice structure [**39**] and to cause significant effects on GaAs nanowire growth [**30**, **38**, **40**]. However, Sn doping of GaAs by using TESn as precursor has showed much less of an impact [**31**, **38**].

Several groups [**30**, **38**, **40**] have reported increased twin plane defect density, kinking and even seed particle splitting in GaAs nanowires when using DEZn precursor and higher II/III ratios. The actual values, though, seem to be rather specific to the used growth system as, for example, a II/III ratio of 0.008 was deemed mostly unusable in [**30**] while a much higher upper limit of 0.16 was reported in [**40**]. Furthermore, lower II/III ratios resulted in no observable changes in structural properties and showed direct proportionality with the resulting estimated Zn acceptor density in [**30**] whereas any doping led to increased twinning in [**40**].

These strong effects on nanowire growth with higher II/III ratios might be related to increased Zn content in the Au seed particle, possibly altering its phase. Haggren et al. [**40**] studied a Au seed particle post growth by quantitative energy-dispersive X-ray spectroscopy and observed it to contain a considerable amount of Zn (nearly 20 at.-%) which might have affected the phase of the particle during growth. They also observed a significant concentration of As in the Au particle, albeit As is not generally dissolved in Au at those temperatures, further indicating a changed Au

particle phase. Additionally, the axial growth rate was found to increase with the II/III ratio and this was attributed to either enhanced Ga diffusion or the changes in the Au particle.

In stark contrast to Zn, Sn doping with TESn precursor has been reported to show no additional structural defects regardless of the used IV/III ratio, possibly due to relatively low solubility of Sn in the Au particle (as compared to Zn solubility) [**31**]. However, an increase in the nanowire axial growth rate with higher IV/III ratios has been observed, attributed to enhanced surface diffusion of Ga adatoms in the presence of TESn [**31**, **38**]. The enhanced growth rate can lead to effective dilution of the doping and hence there might not be a clear proportionality between TESn flow and nanowire doping concentration [**38**].

3.2 Nanowire surface states and passivation

The high density of surface states in III–V materials and related effects like Fermi level pinning is a common and well known problem that becomes more serious in nanowires due to the increased surface-to-volume ratio. Surface or interface states appear due to bond disorder and there is a strong tendency that the Fermi level becomes pinned at free surfaces due to high density of states. Such surface or interface states have several detrimental effects on e.g. FETs and photonic devices using nanowires. Firstly, the Fermi level pinning leads to the formation of a depletion layer at the surface (like in the formation of a Schottky barrier as discussed in section 2.5) increasing the nanowire resistance. Such surface depletion and related band bending is schematically illustrated in figure 14. Secondly, the efficiency of gate control in nanowire FETs is reduced and charge–discharge transients of interface states in the gate stack may cause threshold voltage shifts, drift and hysteresis effects leading to poor performance and reliability. Finally, surface states can cause carrier recombination lowering the quantum efficiency of radiative transitions in photonic devices. [**41**]

GaAs is among those III–V materials that suffer more severely from effects associated with the surface states [**42**]. Free GaAs surfaces exhibit Fermi level pinned approximately in the center of the band gap which can lead to significant surface depletion layers even with elevated doping levels [**31**]. For example, with a 100 nm diameter nanowire, doping concentrations below 10^{17} $1/\mathrm{cm}^3$ are expected to yield completely depleted nanowires and concentrations closer to 10^{18} $1/\mathrm{cm}^3$ would be needed in order to generate a significant amount of free carriers for conduction. GaAs also has an extremely high surface recombination velocity, which is three orders of magnitude higher than in most other III–V semiconductors. [**42**] Furthermore, exposure of GaAs nanowires to oxygen ambient quickly leads to the formation of an oxide shell. This shell does not serve to passivate the nanowire and instead induces acceptor-like levels within the band gap trapping free carriers and hence also resulting in a depletion space-charge region that may extend deep inside the wires. The surface or interface states, in general, may also contribute to the decrease in conductivity (mobility) by increasing carrier scattering. [**43**]

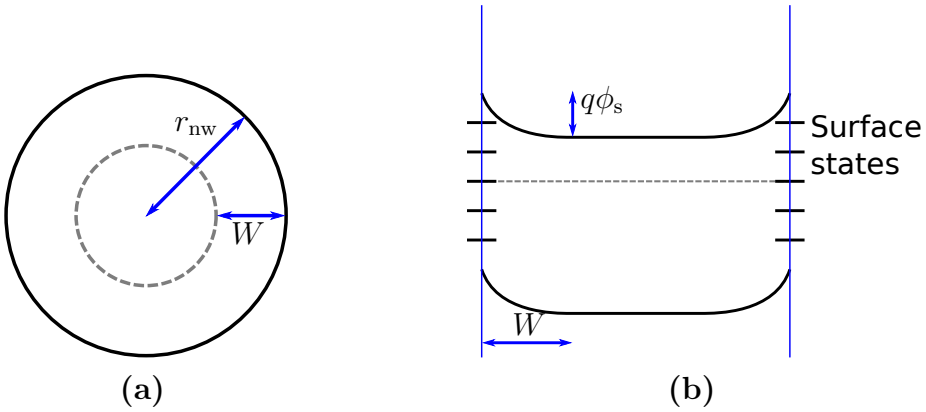

Figure 14: Schematic illustration of surface depletion layer (a) and corresponding band bending (b) in a nanowire resulting from Fermi level pinning due to surface states. For simplicity, the nanowire here has an unrealistic cylindrical shape. The depletion region width W, nanowire radius r_{nw} and surface potential ϕ_{s} are also marked.

A rough idea of the extent of a depletion layer forming in an n-type nanowire, depending on the surface potential ϕ_{s}, doping concentration $N_{\mathrm{D,A}}$ and nanowire radius r_{nw}, can be obtained from a simplified model considering an infinitely long cylindrical nanowire (as in figure 14). This implies radial symmetry and neglecting any edge effects at the ends of the nanowire. Such a model was used in [**44**] where it was further assumed that the charge in the depleted region consists entirely of immobile ionized dopants. Under these conditions, the electrostatics of the nanowire could be treated analytically with Poisson's equation in cylindrical coordinates:

$$\frac{\partial^2\phi}{\partial r^2} + \frac{1}{r}\frac{\partial\phi}{\partial r} = -\frac{qN_{\mathrm{D}}}{\varepsilon_{\mathrm{r}}\varepsilon_0}\,, \tag{27}$$

where ϕ is the potential, r is the general radial distance, ε_{r} is the relative permittivity of the nanowire, ε_0 is the permittivity of free space, q is the elementary charge and N_{D} is the donor concentration. With boundary conditions stating that the electric field and potential are both equal to zero at the depletion region edge ($r = r_{\mathrm{nw}} - W$), the solution for the potential as a function of the radial distance was obtained as

$$\phi(r) = \frac{qN_{\mathrm{D}}(r_{\mathrm{nw}} - W)^2}{2\varepsilon_{\mathrm{r}}\varepsilon_0}\left[\ln\left(\frac{r}{r_{\mathrm{nw}} - W}\right) - \frac{r^2}{2(r_{\mathrm{nw}} - W)^2} + \frac{1}{2}\right], \tag{28}$$

where W is the depletion region width. Equation 28 is transcendental for W but can be solved numerically when setting $\phi(r_{\mathrm{nw}}) = \phi_{\mathrm{s}}$. Furthermore, it suggests that the depletion region increases with reducing dopant density, increased surface potential and reduced nanowire radius. However, this model is not applicable to the case of full depletion and cannot therefore be used to solve under which conditions this would occur. [**44**] In the case of p-type acceptor doping, N_{D} can be substituted with $-N_{\mathrm{A}}$.

Due to the various detrimental effects of surface states, efficient surface passivation is mandatory in order to make use of GaAs nanowires in applications. In general, a

suitable passivation technology should remove surface states to a sufficient degree in addition to which it should be applicable to all the facet types present in nanowires [**41**]. Among the most used passivation techniques of GaAs nanowires is capping with a shell of AlGaAs that is a semiconductor material with wider band gap than GaAs and can be deposited in a MOVPE reactor right after the GaAs nanowire growth [**42**, **45**]. This is a successful technique, especially for reducing surface recombination as indicated by e.g. reported high increase in photoluminescence lifetime and intensity [**42**]. Haggren et al. [**45**] have demonstrated also another surface passivation scheme for GaAs nanowires in which ultrathin epitaxial InP or GaP capping layers were grown in situ in MOVPE. The passivation efficiency of this technique was found to be similar or slightly stronger than with using AlGaAs capping (especially with InP) and it showed good stability. The technique was further considered appealing due to the only few-monolayer thick capping layer requiring no lattice-matching and having little impact on the nanowire morphology, band structure and contacting.

3.3 Metal contacts to nanowires

Obtaining good, i.e. ohmic, metal contacts is typically challenging with bulk semiconductors and even more so with nanowires. Depletion due to the contact formation (as discussed in section 2.5) suggests the need for relatively high doping concentrations to limit the extent of the depletion region and create thin Schottky barriers through which carriers may tunnel. Furthermore, nanowires can generally withstand only gentle processing which poses problems for e.g. oxide removal by etching or contact improvement by annealing. Despite this, forming low-resistance ohmic contacts to nanowires has been achieved in many cases. [**8**] For example, Pt/Ti/Pt/Au (5/10/10/400 nm) stack provided perfectly ohmic contacts to p-type Zn doped ($\gtrsim 4 \times 10^{18}$ 1/cm^3) GaAs nanowires in [**30**] and Ge/Ni/Ge/Au (5/10/25/400 nm) stack with rapid thermal annealing resulted in almost ohmic contacts to n-type Sn doped ($\sim 10^{18}$ 1/cm^3) GaAs nanowires in [**31**]. One way to approach this problem is to highly dope the ends of the nanowire that are used for contacting, thus allowing for a different doping level in the middle segment [**8**]. This would be useful for e.g. nanowire FET structures in order to obtain only moderately doped channel region for efficient gate-modulation and high mobility and highly doped contact regions for small contact resistance (source/drain series resistance) [**13**]. Lower-doped materials typically show nonlinear Schottky-type behavior and, without high-quality contacts, the overall resistance is normally limited by the contacts rather than the nanowire channel [**8**]. In this case, it becomes more difficult to interpret nanowire current–voltage measurements and use them to extract information of the nanowire properties.

In the case of non-ohmic contacts, the nonlinear current–voltage behavior may be modeled by considering a metal–semiconductor–metal system composed of two Schottky barriers connected back-to-back in series with the nanowire channel in between. This model is illustrated in figure 15. The model should be applicable in room-temperature for long nanowires few μm in length with diameters of few tens of nm or more such that the charge transport is within the diffusive regime (effective

mass approximation and Ohm's law can be used to describe the conductance in the undepleted part of the nanowire) and the depletion length is much less than the nanowire channel length. In microelectronic devices, Schottky contacts are expected to cause rectifying current–voltage behavior with negligible current for reverse bias. However, in the nanowire system, the tunneling current through a reverse biased Schottky contact is significant. For a contacted nanowire, an almost symmetric current–voltage characteristic is generally expected. The asymmetry results mainly from different Schottky barrier heights in the two contacts but can also be caused by e.g. different effective contact areas. [**14**]

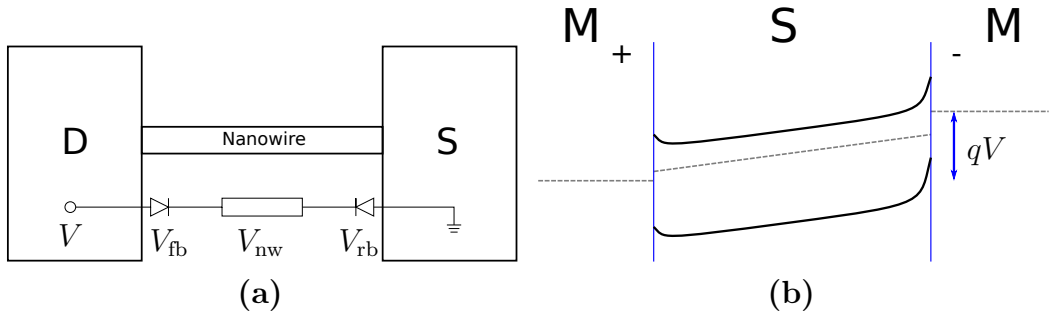

Figure 15: Schematic illustration of the metal–semiconductor–metal model of a contacted (n-type) nanowire showing the equivalent circuit (a) and corresponding band diagram (b).

The overall positive bias voltage V across the contacted nanowire, is divided to voltage drop across the first (forward-biased) Schottky contact V_{fb}, voltage drop across the nanowire channel V_{nw} and voltage drop across the second (reverse-biased) Schottky contact V_{r} as shown in figure 15a. It was suggested in [**14**] that the electrical transport through the forward-biased contact occurs via TE while TFE is the dominating mechanism for the reverse-biased contact. At low bias V, the current is small and the voltage is divided mainly over the two Schottky contacts. When the voltage V is increased, the voltage drop V_{rb} increases rapidly and starts to dominate while V_{fb} remains very small in comparison. However, when V is further increased, contribution from the voltage drop V_{rb} decreases while the voltage drop over the nanowire channel depends on the current and hence increases continuously. Eventually, V_{nw} becomes the dominating term and the current–voltage curve approaches linear behavior. In this large bias régime, the differential resistance $\partial V/\partial I$ comes almost exclusively from the nanowire resistance with much smaller contributions from the contacts. Although the current–voltage curve is affected by e.g. contact areas, native oxide layers and minority carrier injection, all these effects, to a good approximation, should only change the absolute current values and the low bias régime. [**14**]

Another type of nonlinear current–voltage characteristic can result when the nanowire exhibits space-charge-limited (SCL) current. In this electronic transport régime, the current–voltage behavior is dictated rather by the nanowire than the metal contacts and the current becomes proportional to the square of the voltage ($I \propto V^2$). The SCL current behavior can arise when conduction is mobility dominated, when the carrier injection is efficient, and the carrier concentration is low. Thinner nanowires

are more prone to this effect due to e.g. poor electrostatic screening of injected carriers and larger depletion regions resulting from contacts or surface. Furthermore, the carrier concentration needed to obtain Ohmic behavior is much larger in thin wires and the scaling hence favors the SCL current behavior. However, even with SCL current behavior, velocity saturation at larger voltages (higher fields) can lead to $I \propto V$ dependence. [**46**] It should be noted that both SCL current and Schottky-type contact behavior have been observed in a single nanowire [**47**], which further demonstrates that the interpretation of nanowire current–voltage measurements can become significantly more difficult when ohmic contacts are not achieved.

The contact resistance R_c, or the area-independent specific contact resistance ρ_c, of a metal–nanowire contact may be approximated by using a transmission line model as shown in figure 16. The model assumes that the entire circumference of the nanowire (radius r_nw) is in direct contact with the metal along a length (L_c) of the nanowire, that the voltage (V) is uniform throughout the entire metal contact, that the voltage in the nanowire varies only along its length and that the nanowire resistivity below the contact is a constant. Furthermore, the depletion due to the contact formation is assumed to be negligible. The current transport here does not occur uniformly in the contact but rather takes place primarily near the edges. Therefore, the differential interface resistance is $\mathrm{d}R_\mathrm{i} = \rho_\mathrm{c}/(2\pi r_\mathrm{nw}\mathrm{d}x)$ and the differential resistance along the nanowire is $\mathrm{d}R_\mathrm{nw} = \rho\mathrm{d}x/(\pi r_\mathrm{nw}^2)$. The contact resistance can then be solved to be

$$R_\mathrm{c} = \frac{\rho_\mathrm{nw} L_\mathrm{T}}{\pi r_\mathrm{nw}^2} \coth\left(\frac{L_\mathrm{c}}{L_\mathrm{T}}\right), \tag{29}$$

where L_T is called the transfer length and is given as

$$L_\mathrm{T} = \sqrt{\frac{r_\mathrm{nw}\rho_\mathrm{c}}{2\rho_\mathrm{nw}}}\,. \tag{30}$$

However, if the metal is in contact with only a fraction (f_c) of the nanowire circumference, the differential interface resistance becomes $\mathrm{d}R_\mathrm{i} = \rho_\mathrm{c}/(2\pi r_\mathrm{nw} f_\mathrm{c}\mathrm{d}x)$ and ρ_c should be substituted with $\rho_\mathrm{c}/f_\mathrm{c}$ in the solution (equations 29 and 30). [**48**]

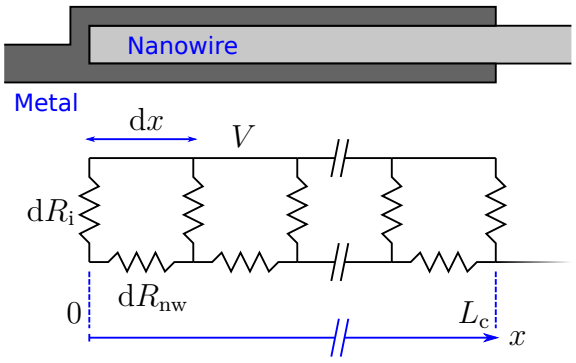

Figure 16: Schematic illustration of an all-around metal–nanowire contact (assuming cylindrical nanowire shape) and the corresponding transmission line model.

4 Research methods

This section describes the fabrication and characterization methods used in this work. Nanowires were first grown by MOVPE after which separate samples were fabricated to form electrical contacts to nanowires detached from the growth substrates. Optical lithography with a laserwriter device was used to define all patterns, reactive ion etching (RIE) was used to etch the alignment markers and evaporation followed by lift-off was used to deposit the contact metals. The nanowire samples (both growth and contacting) were inspected with SEM and separate samples were prepared for micro-Raman measurements. Finally, electrical measurements were carried out for the contacted nanowires.

4.1 MOVPE

MOVPE is a subset of the vapor phase epitaxy growth technique and uses organometallic precursor gases that are introduced to the reactor in continuous flow and decompose either fully or partially in the presence of the heated target substrate. The adsorption of adatoms from the decomposed precursors then leads to growth on the target substrate. The MOVPE apparatus used in this work is manufactured by Thomas Swan & Co. Ltd. and is schematically presented in figure 17. The device consists of bubblers containing the precursor materials, a gas line system that controls the various gas flows in the device, a reactor chamber where the growth takes place and a glove box for sample loading and storage purposes. The device operation is controlled either manually or (partially) by computer software.

The precursor materials are inside bubblers that are immersed in temperature controlled liquid baths (water or glycol). The bubblers operate such that hydrogen carrier gas flow is directed into the bubblers and it saturates with the precursor material while traveling through it. The vapor pressure of the precursor in the mix depends on the material and temperature. Carrier gas flow through the bubblers is controlled with mass-flow controllers and, for some precursors, the output flow to the reactor can be diluted with a hydrogen flow bypassing the bubbler. The precursor materials used in this work were TMGa, TBAs, DEZn and TESn. It should be noted that the gas flows (in sccm) rather than molar flows are controllable in the MOVPE and the molar flows are calculated from these.

The gas line system is actually more complex than in the figure 17 schematic but basically consists of manifold, ventilation and make-up lines. The lines can be fed from either a nitrogen or hydrogen supply. When the precursor materials are used, hydrogen carrier flows are introduced to the bubblers the outputs of which are directed with pneumatic valves to either ventilation or manifold lines. Group III and V precursors have their own lines in order to prevent premature reactions and the manifold lines are combined just shortly before they reach the reactor. The make-up lines (not shown in figure 17) are used to maintain a constant total gas flow to the reactor. Finally, reaction byproducts and unused precursors are flushed from the reactor to a ventilation line. All the ventilation lines eventually lead to a gas scrubber.

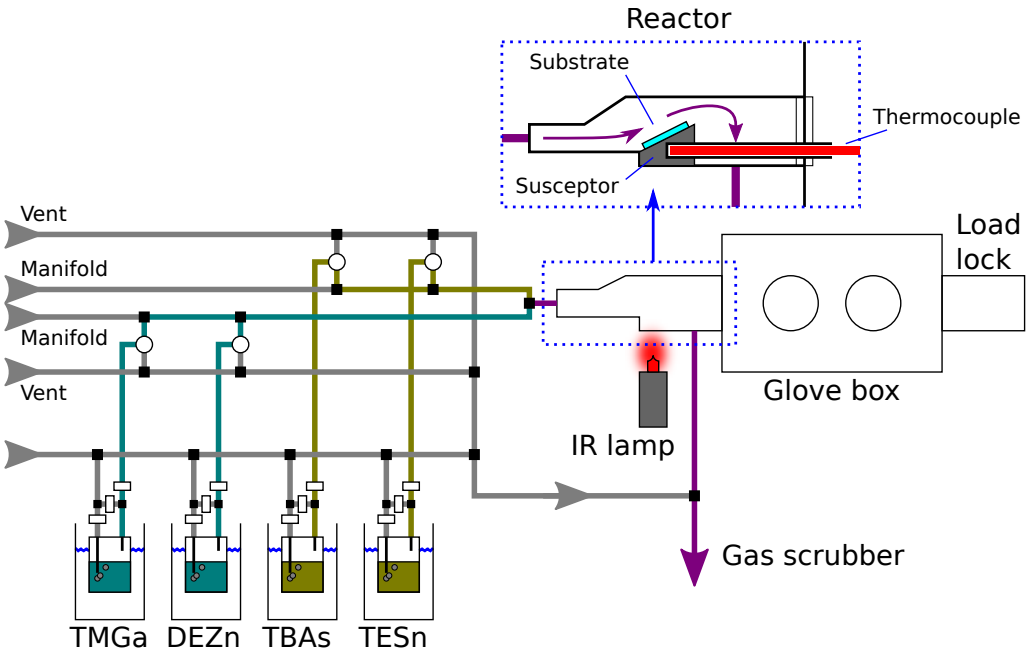

Figure 17: Schematic of the used MOVPE device. The precursor gases are directed to the reactor where growth occurs on the heated sample substrate. Precursor gas flows are indicated with colored lines (arrows) and carrier gas flows with gray lines (arrows).

The reactor chamber is made of quartz and shaped such that it promotes laminar flow of the introduced gases above the target substrates. The substrates are first loaded to an intermediary glove box with nitrogen atmosphere such that the reactor, when opened, is not directly exposed to the outside environment. Furthermore, the gas flow to the reactor is switched to nitrogen during the loading for safety reasons. The substrates are then placed on top of a graphite susceptor which is inserted inside the reactor. The heating is achieved with an infrared lamp that effectively heats the susceptor and hence the samples via heat conduction. The temperature is measured with a thermocouple that is placed inside a quartz tube going through the reactor door and into the susceptor. In general, the temperature readout is some tens of degrees Celsius above the actual substrate surface temperature since, for example, the surface is cooled by the constant gas flow. All the temperatures reported in this thesis, therefore, refer to the temperatures measured from the susceptor as the actual substrate temperatures can not be measured directly.

All the nanowires in this work were grown on p-type Si (111) pieces which were prepared as follows. First, small pieces (less than 1 cm^2) were cleaved from two-inch (111) oriented Si wafers after which the pieces were cleaned. The cleaning was done with ultrasonic bath in acetone and isopropanol subsequently for two minutes each. Afterwards, the pieces were rinsed in de-ionized water for five minutes and dried with nitrogen. Secondly, the pieces were treated with few drops of Poly-L-Lysine which was blown away after approximately one minute. This was done to provide enhanced Au nanoparticle adhesion [**40**] and such treatment has not been found to

affect the growth aside from increased overall nanowire density and uniformity [**29**]. Finally, the Au nanoparticles were deposited on the pieces by pipetting few drops of colloidal Au nanoparticle solution (nominal particle diameter 100 nm). The excess solution was blown away after approximately one minute and the pieces were dried with nitrogen. No etching was used to remove the native oxide layer.

When the MOVPE growth process is controlled by computer software, it executes a recipe step-by-step with each step modifying the different parameters. The main steps of the recipe used in this work are presented in table 1. First, the different flow rates are set and the precursor flows are directed to vent for two minutes in order to stabilize all flows. Next, the temperature is ramped up to 650 °C and the target substrate is baked in hydrogen atmosphere for five minutes in order to desorb surface contaminants and to make the Au nanoparticles to alloy with the Si substrate. After the bake, the temperature is lowered to the growth temperature of 450 °C. Due to the cooling, less Si can be dissolved in the Au particles and excess Si starts to precipitate to the substrate, possibly forming a better particle–substrate interface [**29**]. When the correct growth temperature is reached and remains stable, the precursor flows are directed to the reactor to initiate the growth. The length of this growth step is 900 seconds after which the precursor flows are directed to vent except for TBAs which is kept on until the temperature has cooled down to 300 °C. This is done in order to avoid nanowire decomposition by As desorption from the surfaces. Finally, the reactor is flushed with hydrogen flow for five minutes and the flows are then changed to nitrogen.

Table 1: Main steps of the nanowire MOVPE growth recipe used in this work.

#	**Step**	**Time (s)**	**Temp. (°C)**	**TMGa**	**TBAs**	**Dopant**
1	Flow stabilization	120	-	Vent	Vent	Vent
2	Bake	300	650	Vent	Vent	Vent
3	Cooling	-	-	Vent	Vent	Vent
4	Nanowire growth	900	450	Reactor	Reactor	Reactor
5	Cooling to 300 °C	-	-	Vent	Reactor	Vent
6	Flush	300	-	Vent	Vent	Vent
7	Flows to nitrogen	-	-	Vent	Vent	Vent

The nominal V/III ratio was 24.5 and the nominal molar flows of TBAs and TMGa were 149.6 μmol/min and 6.11 μmol/min, respectively for all the growth samples. These values along with the growth temperature of 450 °C have been previously found to result in good yield of undoped epitaxial GaAs nanowires in this specific growth system [**49**]. Furthermore, this growth temperature has also been reported elsewhere to produce good epitaxial nucleation and straight vertically aligned growth with varying V/III ratios, although with considerable tapering as well [**28**, **30**, **31**, **38**]. The dopant precursor molar flows were adjusted accordingly to obtain the desired II/III or IV/III ratios.

4.2 Lithography

In a standard simple photolithography process, the sample substrate is covered by a photoresist polymer which is then subsequently patterned with openings through the layer. First, the sample undergoes a surface preparation step, e.g. baking and priming. Secondly, photoresist is spin coated on the sample and baked to drive out the solvent (so-called "soft bake"). The photoresist layer is then exposed to UV radiation with a given image pattern, typically realized by shining UV light through a photomask. In a positive photoresist, exposure to UV radiation makes the exposed areas soluble, while in a negative photoresist, the exposure causes cross-linking leading to reduced solubility. The exposure is in some cases followed by a post-exposure bake to e.g. complete the photopolymerization process initiated by the exposure. After the exposure, the photoresist is developed in a developer solution that dissolves the soluble parts of the resist layer. Finally, the sample with patterned photoresist is baked to harden the resist (so-called "hard bake"). [**50**, p. 103–106]

Laserwriting is a lithography process in which the photoresist exposure is done by a focused laser beam that scans over the sample. First, the image pattern is rasterized by the control computer, after which the laser beam scans the exposure area point-by-point and a shutter is used to control whether any single point in the pattern gets illuminated or not. A laserwriter system thus needs a laser source, focusing optics, and moving stages for the scan. Lenses with different magnification and numerical aperture can be used to obtain varying beam size and hence varying resolution. The scan can be made by either moving the lens, moving the sample stage or a combination thereof. The larger the beam size (the lower the resolution) the larger the step size can be in the rasterized pattern and the faster the overall exposure.

The laserwiter device used for all lithographic patterning in this work was Microtech LW405A. The device uses a GaN laser (405 nm wavelength) for exposure and it can be operated in beam scan, stage scan or vector scan mode. There are four lenses with different magnification and the best achievable resolution is around 0.8 μm when the lens with highest magnification and numerical aperture is selected. Figure 18 shows a schematic of the laserwriter device.

The different patterns written with the laserwriter were made on a positive AZ 5214E photoresist using the normal lithography process, excluding the initial surface preparation and the bakes after the exposure. However, for the contact metalization patterns, a reverse lithography process was used instead. In this reverse process, the negative of the pattern is exposed on the resist after which the sample is baked at 120 °C for 2 min using a hot plate (so-called "reverse bake"). The AZ 5214E photoresist is designed for this kind of process and the exposed areas thermally cross-link during the bake making them insoluble in the used AZ 351B developer. The whole resist is then exposed to a 3 second UV flash which makes the previously unexposed areas soluble, but is insufficient to affect the thermally cross-linked areas. The idea of the reverse process is to obtain negative side-wall profile (the resist openings widen towards the substrate) which is beneficial in the contact metal evaporation and lift-off explained in section 4.4.

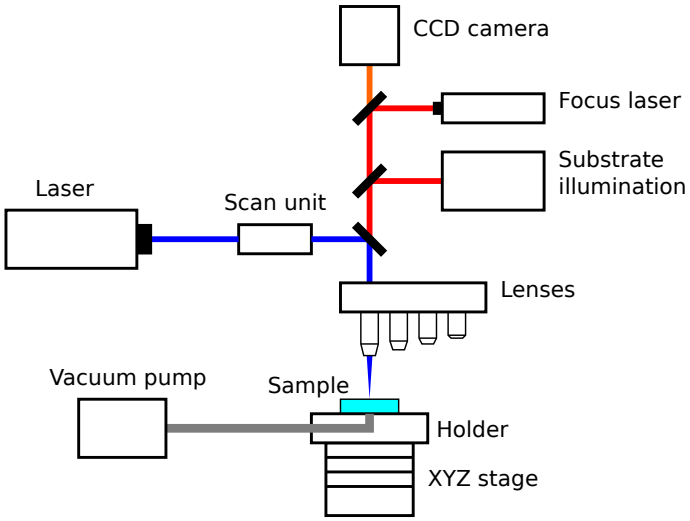

Figure 18: Schematic of the used laserwriter device. The sample is aligned and focused with the help of the camera and focus laser whereas the exposure is obtained by scanning the writing laser beam over the sample surface. The holder uses vacuum to keep the sample firmly attached during operation.

4.3 RIE

RIE, also called plasma etching, is an etching technique that uses reactive gases excited by RF electric fields in a vacuum chamber. The plasma discharge generates ions and excited neutrals both of which are important for plasma etching. The etching results as a combination of chemical reactions between the excited gas molecules and the target material and physical bombardment by the ions accelerated in the RF field. In order for the etching to take place by chemical reactions, the bonds in the etch reaction products should be stronger than in the target material. The etch reaction products must also be volatile such that they diffuse away exposing the target for further reactions. The main advantage of RIE compared to wet etching is the possibility for enhanced anisotropy (vertical sidewalls) due to the directionality of the physical ion bombardment – especially when combined with passivating reactions on the sidewalls. [**50**, p. 132–134]

A schematic of a RIE system is shown in figure 19. The gases are introduced to the reactor chamber through the perforated top electrode and the target substrates are placed on a bottom electrode connected to the RF generator. The plasma of excited and ionized species is ignited above the target surface and the gas phase etch reaction products diffuse away from the target and get eventually removed from the chamber. [**50**, p. 133]

The RIE system used for pattern etching in this work was Oxford Instruments Plasmalab 80Plus. This tool was used to etch alignment marker patterns in the SiO_2 layer of the substrates used for nanowire contacting. The substrates were first coated with AZ 5214E photoresist layer and the marker patterns were processed to the resist using the laserwriter lithography as described in the previous section. The

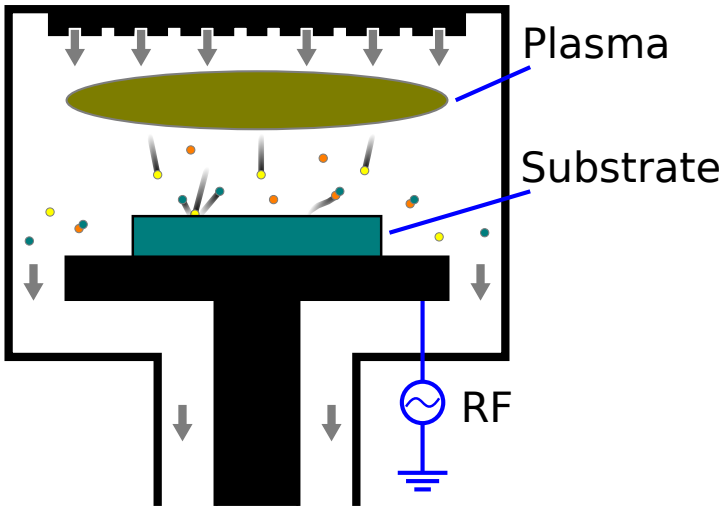

Figure 19: Schematic of a RIE system. The gases are introduced to the reactor chamber through the perforated top electrode and the plasma discharge is ignited above the substrate. Ions accelerated by the RF field and excited neutrals etch the substrate via physical bombardment and chemical reactions. The etch products then diffuse away from the target and get eventually removed from the chamber.

patterned resist then acted as an etch mask for the RIE. A basic SiO_2 etch recipe was used for which the expected etch rate for thermal SiO_2 was 45 nm/min. The used recipe provides good selectivity against Si and, since the resist thickness was around 1 μm, resist consumption was also not a concern. The remaining resist was found to be hardened by the RIE process and was removed by placing the substrates to an ultrasound-assisted acetone bath for 15 minutes.

4.4 Evaporation

Evaporation is a form of physical vapor deposition in which the source material is heated to high temperatures causing evaporation of the material and the evaporated atoms travel to the target substrate in high vacuum. A schematic illustration of an evaporator system using electron beam heating is shown in figure 20. The electrons are first emitted from an electron source after which they are accelerated by a strong electric field (high acceleration voltage). The beam of electrons is then targeted on a solid piece of source material inserted in a crucible. The electron beam strongly heats the material from which atoms will start to evaporate. [**50**, p. 48–50]

Under vacuum conditions with pressure below around 10^{-4} torr, the mean free path of the evaporated atoms is typically larger than the size of the deposition chamber and the atoms hence travel to the target substrate without experiencing much collisions. This results in line-of-sight-like deposition on the target substrate facing towards the crucible. The line-of-sight deposition combined with the low temperature of the target substrate leads to poor coverage on vertical sidewalls even if the film quality is good on planar surfaces. However, the target could be heated to

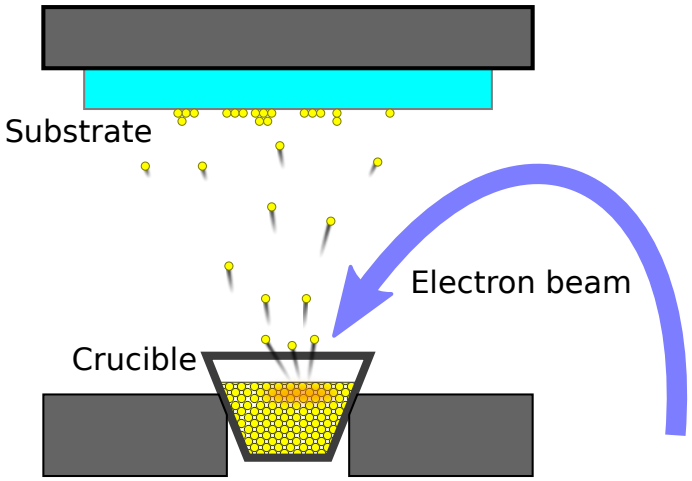

Figure 20: Schematic of an electron beam evaporator system. The source material in the crucible is heated to high temperatures by the electron beam and the evaporated atoms travel to the target substrate in high vacuum.

promote surface diffusion of the adsorbed atoms resulting in improved film quality and uniformity. Evaporation is easier for different elemental metals than metal alloys or compounds. Typical deposition rates are very low, around 0.1 ... 1 nm/s. [**50**, p. 48–50]

The evaporator tool used in this work for contact metal deposition was Edwards E306A thermal evaporator and it was operated exclusively in the electron beam configuration (resistive heating of source filaments being the other option). For contacting the Zn doped p-type nanowires, AuZn alloy (95–5 wt%) was used with layer thicknesses ranging in 150 ... 200 nm. The AuZn deposition rates varied in the range 0.1 ... 0.3 nm/s. For contacting the Sn doped n-type nanowires, Ni/AuGe/Ni stack (AuGe composition 88–12 wt%) was used as that is a known contact system for n-type GaAs [**51**]. The layer thicknesses in the stack were 5/150/15 nm and deposition rates were 0.1 nm/s for Ni and 0.2 ... 0.3 nm/s for AuGe. The sample substrates were not heated during the evaporation, but the Ni/AuGe/Ni metalization was later annealed at 320 °C for approximately 1 min using rapid thermal processing.

The patterning of the metal contacts was achieved by using the so-called lift-off process, the idea of which is illustrated in figure 21. First, a resist layer is deposited on the sample and then patterned using the laserwriter and reverse lithography process as described in section 4.2. Secondly, the contact metal is evaporated over the sample. The evaporated metal film covers the resist as well as the substrate on those areas exposed by the resist pattern. However, due to the line-of-sight deposition in evaporation and the negative sidewall profile from the reverse lithography process, the evaporated metal film becomes discontinuous at the edges of the pattern (as long as the resist is sufficiently thicker than the evaporated film). This is critical for the lift-off technique, since the final step is to remove the resist in acetone which then also leads to removal of the metal that was deposited over the resist. Therefore, only the areas originally exposed by the resist pattern will be covered by the metal.

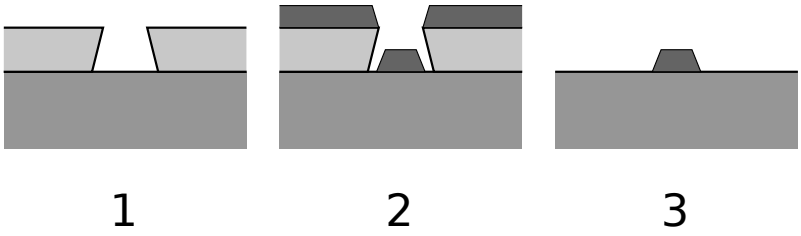

Figure 21: Schematic of the lift-off process consisting of resist deposition and patterning (1), metal evaporation (2) and resist removal (3).

4.5 SEM

A SEM device produces a finely focused beam of electrons that is scanned over the sample surface and the scattered electrons are detected to form an image of the surface topography. SEM is capable of generating high resolution images (lateral resolution down to few nanometers) in addition to which it has a large depth of focus (distance within which the sample remains in focus). A schematic of a SEM device is shown in figure 22. The main components in a SEM device are the electron source, the SEM column and the specimen chamber with the sample holder unit and detectors. A vacuum generation system is used to provide the vacuum conditions under which the SEM is operated. Finally, a screen is needed to show the SEM image. Typically, computers are used for both controlling the SEM and to display the SEM image. [**52**, p. 86–105]

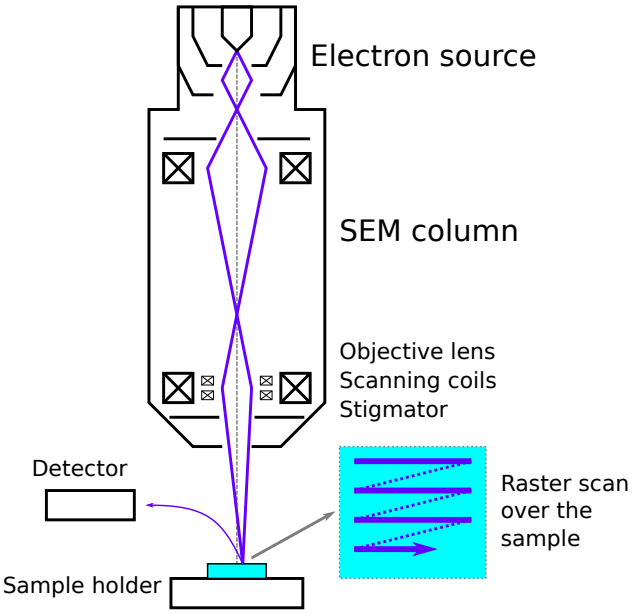

Figure 22: Schematic of a SEM device.

The electron beam in a SEM is first generated by an electron source working under high vacuum conditions. The emitted electrons are accelerated by a high acceleration voltage between the source (cathode) and an anode. [**52**, p. 30–32] The electron beam is then shaped and focused in the SEM column by a set of apertures

and magnetic lenses. At the end of the column, an objective lens is used to demagnify the beam to a small spot. Furthermore, the column also contains scanning coils and (possibly) a stigmator within the objective lens. The magnetic field of the scanning coils is used to deflect the electron beam from the optic axis in x- and y-directions to produce the scanning pattern over the sample surface. The stigmator is used to correct astigmatism resulting from imperfections of the magnetic lenses. If not corrected for, astigmatism distorts the cross-section of the beam from spherical towards elliptic leading to reduced resolution and image sharpness. The sample holder in a SEM is typically inserted in a goniometric unit such that the xyz-position, rotation and tilt can be controlled. [**52**, p. 95–97]

There are two types of signals generated by the interaction of the electron beam (primary electrons, PE) and the sample that are utilized to form a SEM image: secondary electrons (SE) and backscattered electrons (BSE). A secondary electron is created when a PE scatters inelastically from a valence electron of an atom in the sample, thus exciting the electron and ionizing the atom. Most of the PE energy goes to the ionization and the excited SE thus has a low kinetic energy. Therefore, only those SEs originating from a very thin surface layer of few nanometers can escape the sample and contribute to the detectable SE signal. On the other hand, backscattered electrons are PEs strongly deflected by interaction with atomic nuclei of the sample. This type of scattering is almost elastic as only a very small part of the energy gets converted to continuum ("bremsstrahlung") x-ray radiation. Therefore, BSEs have relatively high kinetic energies and can escape the sample from much deeper than SEs. Additionally, PEs can excite atoms in the sample and subsequent de-excitation leads to emission of characteristic x-rays. These can provide information on the chemical composition and hence augment the SEM image. [**52**, p. 94–95]

The contrast in a SEM image results from variation of generated electron signal intensity from different spots in the scan area. The contrast formation in the SE mode is mainly determined by the local inclination of the sample surface with respect to the incident beam, especially at surface edges. The maximum contrast enhancement at an edge occurs when the average penetration depth of the PE corresponds to the height of the step. The penetration depth can be altered with the acceleration voltage as high-energy PEs have reduced scattering cross-section and penetrate deeper into the sample. BSEs additionally show elemental composition contrast as PE interaction with atomic nuclei is much stronger for heavy elements. [**52**, pp. 100–103]

The SEM image resolution is affected by the incident beam diameter and the interaction of PEs with the sample [**52**, p. 100]. The electron beam diameter is directly proportional to the working distance, defined as the distance between the pole piece of the objective lens and the sample surface [**52**, p. 89–91]. However, the area from which electrons are detected has larger diameter due to diffusion of the PE beam inside the sample. This results in decreased resolution, especially for BSEs that can escape from deeper within the sample.

A common problem in SEM imaging of insulating samples is image distortion due to the effect of sample charging. This occurs when the charge supplied to the sample by incident PEs differs from the charge release caused by the emission of SEs and BSEs. The ratio of supplied and released electrons depends on the PE energy,

angle of incidence and the atomic number of the sample material. Charging can be prevented by using a thin (grounded) metal coating to conduct the electrons away. Another way to avoid the charging is to use such acceleration voltages for which dynamic charge compensation takes place. [**52**, p. 103]

The SEM device used in this work was Zeiss Supra 40 with an in-lens SE detector. SEM was used to inspect and take measures of nanowires that were still attached to their growth substrates as well as those detached and dispersed for either electrical contacting or Raman measurements. In order to get a good side-view of the nanowire growth samples, the substrates were cleaved and the cleavage plane was directed towards the SEM column and detector. Furthermore, this allowed to better view the nanowires closer to the center of the substrate, which is preferable to the edge areas that might have differing Au nanoparticle density and growth conditions. For inspecting the nanowires, acceleration voltages in the range 8 ... 10 kV and working distances between 5 ... 9 mm were used. When inspecting the nanowire Raman samples, charging of the SiO_2 layer resulted in slightly lower quality images.

4.6 Electrical measurements

Electrical measurements for contacted nanowires were performed using a HP 4155A semiconductor parameter analyzer connected to a probestation equipped with a microscope and manually operated needle probes. The main parameter of interest was the charge carrier concentration in the nanowires as a result of the varied doping. In order to obtain the carrier concentration both the majority carrier mobility ($\mu_{\mathrm{e,h}}$) and nanowire resistivity (ρ) need to be known. Therefore, two types of measurements were conducted: current–voltage measurements to obtain nanowire resistances (R) and transconductance (g_{m}) measurements on nanowire FET structures to obtain majority carrier mobilities. Using equations 7, 9 and 23, the majority carrier concentration (n or p) is obtained as

$$n, p = \frac{1}{q\mu_{\mathrm{e,h}}\rho} = \frac{1}{q}\frac{C_{\mathrm{gl}}|V_{\mathrm{DS}}|}{g_{\mathrm{m}}}\frac{1}{R\pi r_{\mathrm{nw}}^2}\,, \tag{31}$$

where q is the elementary charge, C_{gl} is the nanowire FET gate capacitance per unit length, V_{DS} is the drain–source voltage in the transconductance measurement and r_{nw} is the nanowire radius (assuming circular cross-section). When surface depletion is taken into account, the effective radius $r_{\mathrm{nw}} - W$ depends on the concentration of ionized dopants (equation 28) which is assumed to be equal to the majority carrier concentration. An overall transcendental equation for n is hence obtained and can be solved numerically. In general, the total resistance and (apparent) transconductance can be measured accurately but translating them to the resistivity and mobility values often involves questionable assumptions [**8**].

The four-point measurement scheme shown in figure 23a can be used to separate the nanowire resistance from the contact resistances. In a four-point measurement the current is supplied by the outer two contacts while voltage is probed between the two middle contacts (with high input impedance). In this way, the measured voltage drop results only from the resistance of the nanowire segment between the

voltage probing contacts. If the voltage-probing contacts are Schottky-type, the depletion due to contact formation reduces the nanowire cross-section for conduction and increases the nanowire resistance below the contacts. On the other hand, even if the contacts are ohmic, they can be invasive such that part of the electrons scatter from the nanowire to the metal contacts and thus alter the current flow (as in figure 23b) [**8**]. It was suggested in [**48**] that it is necessary for the two middle contacts to be short compared to the transfer length L_T (given by equation 30), or else a significant portion of the current may be transported via contacts rather than the semiconductor nanowire beneath. Altogether, the effect of voltage-probing contacts is also minimized if they are very short compared to the nanowire length.

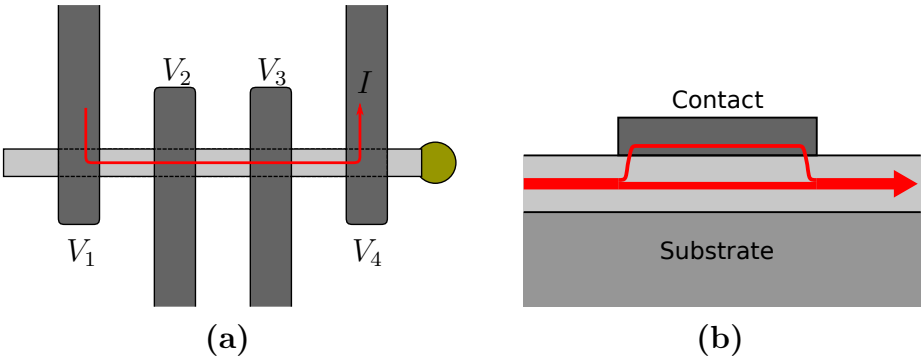

Figure 23: Nanowire four-point current–voltage measurement configuration (a) and possible problem with invasive middle contacts disrupting the current flow (b).

An alternative measurement scheme uses the middle contacts for current and outer contacts for probing voltage, thus essentially forming Kelvin test structures (as in [**53**]) measuring the contact resistances of the middle contacts. Since the current I flows only between fingers 2 and 3, there is no voltage drop along the nanowire towards fingers 1 and 4 and the contact resistances are obtained as $R_{c2} = (V_2 - V_1)/I$ and $R_{c3} = (V_4 - V_3)/I$. This approach avoids the problem of current leaking to the middle contacts. On the other hand, as discussed in section 3.3, the current through a metal–semiconductor contact is not uniform and the contact resistance results from both the interface resistance and the resistance of the nanowire below the contact. Since the voltage in this scheme is probed from the other side of the contact with respect to current flow, the full contact resistance is likely not accounted for.

The obtained nanowires with only two- and three-point contacts were also measured in this work. Nanowires with three contacts form a Kelvin test structure in which the contact resistance of the middle contact can be measured as just described. The other contact can then be approximated to either have the same specific contact resistance ρ_c (Contact resistance given by equation 29) or just the same resistance altogether. The latter approximation is less likely to be accurate since the contact resistance is also affected by the contact area and the nanowire resistivity. When nanowires have only two contacts, however, it is not possible to measure either of the contact resistances and their contribution to the total resistance is unknown.

Fabricating nanowire FET structures and conducting transconductance measurements is the most commonly used method to extract majority carrier mobilities in nanowires [**8**]. In a nanowire FET the nanowire itself acts as the channel while the contacted ends form the source and drain. The transistor gate can be e.g. a third metal contact in the middle on top of a thin insulating dielectric layer (a top-gate), the conductive bulk of the substrate below a dielectric layer (a back-gate), or a metal contact wrapped around the nanowire with a dielectric layer in between (a wrap-gate). Different gate types are schematically illustrated in figure 24. The wrap-gate offers the best gate control of the nanowire channel [**54**] but it is also more difficult to fabricate. In this work, the back-gate configuration (figure 24b) was primarily employed since the only additional fabrication step required was making an electric contact to the substrate. This was achieved by using silver paint on the back of the sample substrates. It is typically assumed that the only difference in the drain current calculation between the planar and nanowire FETs is in the gate capacitance due to the different device geometries [**14**] and equation 23 can hence be used. However, due to the difficulty of obtaining good contacts to nanowires, the source and drain series resistances are not negligible. Therefore, both the transconductance obtained from measurements and the mobility evaluation are expected to be the more inaccurate the larger the contact resistances are relative to the nanowire resistance.

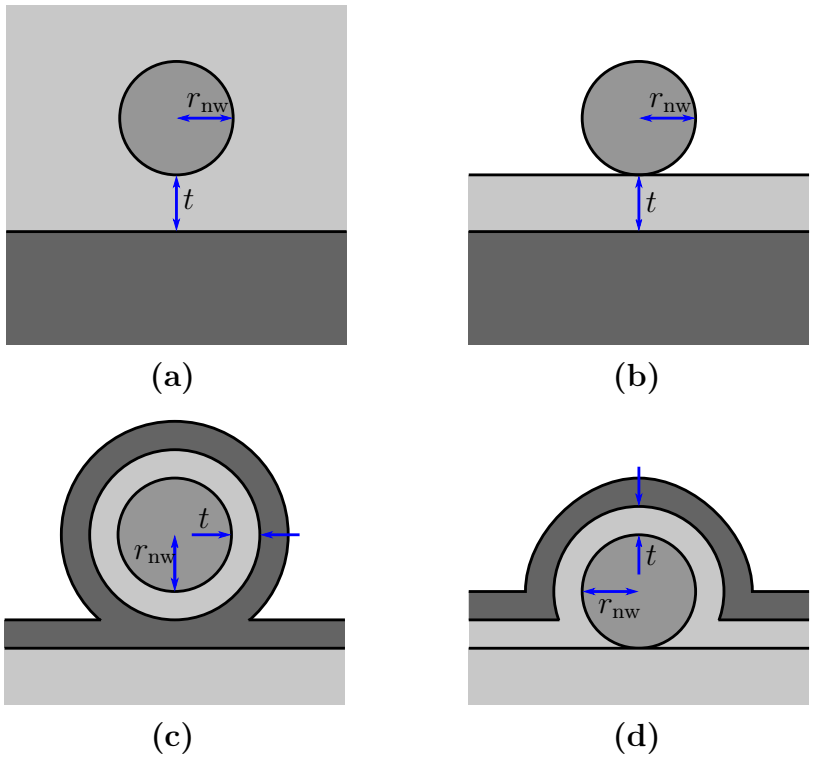

Figure 24: Cross-sections of different nanowire FET gate configurations: (a) back-gate and nanowire embedded in dielectric (b) back-gate and nanowire on top of dielectric (c) wrap-gate and (d) top-gate. For simplicity, the nanowire here has an unrealistic circular cross-section. Nanowire radius r_{nw} and thickness of the dielectric t are also marked.

For the nanowire back-gate FET configuration, a rough approximation for the gate–channel capacitance can be obtained by considering the nanowire as an infinite conducting cylinder (radius r_{nw}) surrounded by an insulator (dielectric constant $\varepsilon_{\mathrm{r,i}}$) located a distance t above an infinite conducting plane (the substrate) as in figure 24a. In this case, the capacitance per unit length can be solved analytically and is given as

$$C_{\mathrm{gl}} = \frac{2\pi\varepsilon_{\mathrm{r,i}}\varepsilon_0}{\operatorname{arccosh}(\frac{r_{\mathrm{nw}}+t}{r_{\mathrm{nw}}})}\,, \tag{32}$$

where ε_0 is the vacuum permittivity. Several assumptions are made here and they, in general, do not hold very well. First, the charge density in the nanowire is assumed to be high enough that the semiconducting nanowire can be treated as metallic. Secondly, it is assumed that the nanowire is much longer than the dielectric layer thickness t such that the fringing capacitance at the source and drain contacts can be neglected. Furthermore, there should be no movable charges or defects in the dielectric layer or at the nanowire surface. [**54**, **55**]

If the nanowire is not fully embedded but rather lies on top of the dielectric layer (as in figure 24b) an effective dielectric constant $\varepsilon_{\mathrm{r,eff}}$ can be used in equation 32 [**54**, **55**]. According to finite element simulations [**54**], in the case of SiO_2 dielectric and hexagonal nanowire cross-section, an effective dielectric constant of $\varepsilon_{\mathrm{r,eff}} = 2.25$ yields a good agreement with numerical results for $6 < t/r_{\mathrm{nw}} < 100$. However, this correction works well only due to the relatively small difference between the dielectric constants of SiO_2 and air. For example, with larger dielectric constant materials (like HfO_2) good agreement cannot be reached due to the drastic changes in the electric field in the non-embedded case and the analytical solution is not applicable. [**54**, **55**]

For a wrap-gate nanowire FET (figure 24c), again assuming cylindrical shape and infinite length, the capacitance per unit length is given as

$$C_{\mathrm{gl}} = \frac{2\pi\varepsilon_{\mathrm{r,i}}\varepsilon_0}{\ln(\frac{r_{\mathrm{nw}}+t}{r_{\mathrm{nw}}})}\,, \tag{33}$$

where t is the thickness of the insulator layer surrounding the nanowire. As a first approximation, equation 33 can be used for the top-gate configuration (figure 24d) as well leading to a slight overestimation of the capacitance. [**55**] An added benefit of the wrap- or top-gate configuration is that the gate voltages do not affect the source and drain contacts unlike in a back-gate configuration. When the nanowire contacts are poor and the back gate field additionally affects them, the interpretation of gate–sweep measurements becomes more difficult [**8**].

4.7 Micro-Raman spectroscopy

In micro-Raman spectroscopy a confocal microscope is used to focus a laser beam on the sample (providing submicron lateral resolution) and this is used to probe the vibrational excitations in the sample by detecting the scattered radiation and measuring the change in energy due to inelastic photon–phonon scattering. More specifically, Raman scattering (in crystalline materials) refers to the scattering of

(visible) light from phonons of optic branches in the dispersion relation of the material [**10**, p. 257]. Intensity peaks in the measured Raman spectrum (intensity versus energy shift) indicate detected phonon modes and these spectra give information on e.g. composition, crystal structure and defects [**56**]. Conventionally, the Raman intensity has an arbitrary unit and the energy shift is given as normalized to a unit of cm^{-1}.

In this work, micro-Raman measurements were used to investigate the crystal structure and quality of the grown GaAs nanowires with varied doping. The used micro-Raman system was WITec Alpha 300 RA and a schematic of the setup is shown in figure 25. The setup uses a backscattering geometry and consists of a laser source (wavelength of 532.07 nm), a microscope equipped with lenses of different magnification, a video camera for normal microscope inspection and a cooled Raman CCD detector. The dispersion grating in the Raman detector unit provides a spectral resolution of 0.8 cm^{-1}. The light source (white light or laser) and detector (video camera or Raman CCD) are selected manually. The samples for micro-Raman measurements were prepared by dispersing nanowires on the sample substrates by mechanical contact with the growth substrates. The pieces used as sample substrates (roughly 1 cm × 1 cm) were diced from SiO_2 coated Si wafers with patterned marker grids for each piece. After dispersing, suitable nanowires were found by inspection with optical microscope and the locations were recorded.

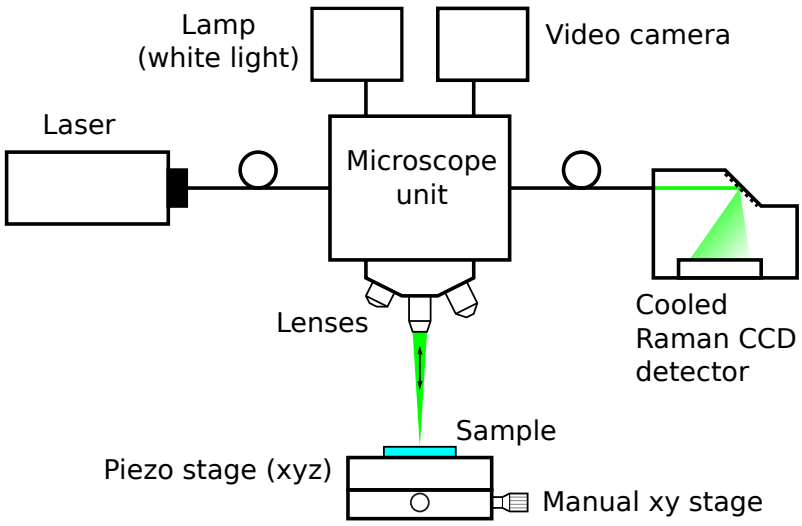

Figure 25: Schematic of the used micro-Raman system. The sample is initially positioned with the manual xy stage while inspected by the video camera. The piezo stage is used to scan the confocal laser beam over the sample and the backscattered light is collected and directed to the cooled Raman CCD detector.

In single crystalline materials, the atomic lattice vibrations (or phonons equivalently) are restricted to allowed modes (with angular frequency ω_q and wave vector $\vec{\mathbf{k}}_q$) corresponding to standing wave solutions as described by the dispersion relation ($\omega_q(\vec{\mathbf{k}}_q)$). In three dimensions, the vibrations can be either transversal (shear) or

longitudinal. A crystalline material that has a basis with two dissimilar atoms (like GaAs) gives rise to separate branches of allowed modes, termed acoustic and optic branches. In general, if there are M primitive cells in the crystal with b atoms each, there is a total of $3Mb$ dynamical degrees of freedom. Since each branch has M allowed modes in the first Brillouin zone (containing all physically meaningful modes), there are $3b$ different branches of which 3 are acoustic and $3(b-1)$ optic. The branches can also overlap in which case they are degenerate. [**10**, p. 218–234]

The interaction of photons with the sample can be envisaged as momentary absorption of an incident photon producing electronic excitation of an atom followed by a de-excitation and the emission of another photon. If the emitted photon has the same energy (frequency) as the incident photon, the scattering is elastic Rayleigh scattering. Inelastic scattering involving an incident photon and one phonon can take place either via a Stokes or an anti-Stokes process as schematically illustrated in figure 26. The Stokes process corresponds to the creation of a phonon and emission of a photon with lower energy (frequency) whereas the anti-Stokes process corresponds to the destruction of a phonon and emission of a photon with higher energy (frequency). The overall energy and momentum (or crystal momentum) are conserved in these processes such that

$$\omega = \omega_0 \pm \omega_\mathrm{q} \tag{34}$$

and

$$\vec{\mathbf{k}} = \vec{\mathbf{k}}_0 \mp \vec{\mathbf{k}}_\mathrm{q} + \vec{\mathbf{G}}\,, \tag{35}$$

where ω, ω_0 and ω_q are the (angular) frequencies and $\vec{\mathbf{k}}$, $\vec{\mathbf{k}}_0$ and $\vec{\mathbf{k}}_\mathrm{q}$ are the wave vectors of the incident photon, emitted photon and the phonon, respectively, and $\vec{\mathbf{G}}$ is a reciprocal lattice translation vector in the sample. Higher order Raman scattering involves several phonons that are created or destroyed simultaneously, but these processes are much more unlikely to take place and to contribute to Raman measurements. Since the wave vector of the incident light is much smaller than phonon wave vectors corresponding to the boundaries of the first Brillouin zone, only those vibrational states near the zone center ($\vec{\mathbf{k}}_\mathrm{q} \approx 0$) are probed. [**10**, p. 256–260]

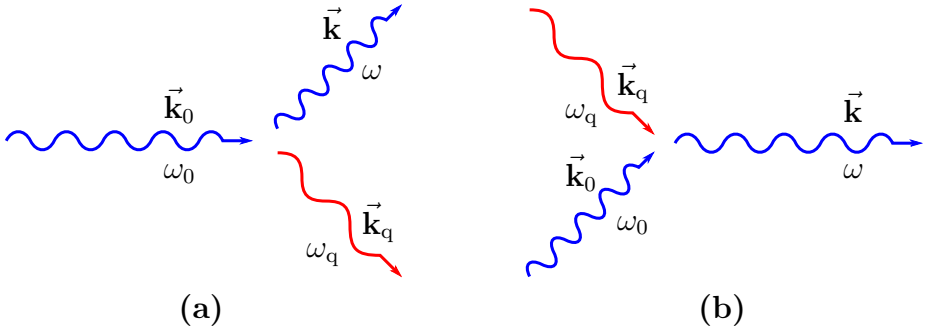

Figure 26: Inelastic scattering of photons by a single phonon in (a) Stokes process and (b) anti-Stokes process.

GaAs nanowires have been reported to exhibit three fundamental mode related intensity peaks in Raman spectra, denoted here as TO, LO and E2. Some reported values for the peak positions are given in table 2. GaAs nanowires with ZB structure have been reported to show the TO and LO mode related peaks [**56**–**58**] while WZ structure additionally gives rise to the E2 mode peak [**56**]. Bulk GaAs, on the other hand, only exhibits the TO peak since light interaction with the LO mode in backscattering is not allowed by the Raman selection rules derived from the energy and momentum conservation requirements. These selection rules predict that the TO mode is allowed in backscattering from the {110} and {111} surfaces while the LO mode is allowed in backscattering from {100} and {111} surfaces, respectively (the nanowire growth direction being $[\bar{1}11]$). [**56**] However, those {110} nanowire side facets not perpendicular to the incident direction should allow scattering from the LO mode as well [**58**]. Controversially, both the absence and presence of the LO mode peak for GaAs nanowires grown along the [111] (or equivalent) direction has been reported [**56**, **58**]. Additionally, the LO mode has been observed in backscattering configuration from nanowires with $\{11\bar{2}\}$ side facets with polarizations perpendicular to the [111] growth direction [**59**]. ZB GaAs nanowires have also been reported to show a surface optic (denoted here as SO) mode related peak on the lower frequency side of the LO peak [**57**, **58**]. The SO peak position downshifts and intensity increases with decreasing nanowire diameter while the TO and LO peaks remain unaffected [**58**].

Table 2: Some reported peaks in GaAs Raman spectra. Nanowires were grown in [111] (or equivalent) directions.

Peak	**Structure**	**Facet**	**Position (cm^{-1})**
TO	ZB (bulk)	$(0\bar{1}1)$	267.2 [**56**]
TO	ZB (bulk)	(111)	$\sim$ 269 [**58**]
LO	ZB (bulk)	(111)	$\sim$ 292 [**58**]
TO	ZB (nanowire)	{110}	266.7 [**56**], 268.7 [**58**]
LO	ZB (nanowire)	oblique {110}	292.2 [**58**]
TO	WZ (nanowire)	{110}	$\sim$ 266 [**56**]
E2	WZ (nanowire)	{110}	$\sim$ 256 [**56**]

The peak positions and full width at half maximum (FWHM) values are indicative of the structural quality of the nanowires. For example, the presence of structural defects causes downshift in the TO and LO peak positions (compared to a corresponding defect free crystal) the more the shorter the defect-free regions are [**57**]. Similarly, high density of defects causes peak broadening, i.e. increased FWHM values. Furthermore, stress in the nanowire, e.g. due to ZB–WZ polytypism, can also cause such effects. The peak intensities, however, are typically not directly comparable between different nanowires. On the other hand, variation of the E2 peak intensity within a single nanowire, for example, can be indicative of the variation in the fraction of the WZ phase. [**56**] It should be noted that the intensities can further depend on the incident and analyzed polarization. It was found in [**56**] that the TO peak shows maximum intensity when incident polarization is parallel to the nanowire

while the E2 peak shows maximum intensity when polarization is perpendicular to the nanowire. In both cases, maximum intensities are observed when both incident and analyzed polarization are parallel to each other (in addition to the alignment with regard to the nanowire). Conversely, no clear incident polarization dependence of the TO and LO peak intensities was observed in [**57**].

In some cases, the effects of doping are discernible in Raman spectra. For example, in polar semiconductors like GaAs, the screening of longitudinal optic phonons by charge carriers results in the LO signal predominantly originating from the surface depletion layer. Therefore, the LO peak intensity is reduced with higher doping along with the depletion layer depth. [**59**] Additionally, the longitudinal optic phonon–plasmon coupled mode from the non-depleted region may be probed. The coupled mode peak shifts from the LO towards the TO with increasing carrier concentration and the intensity gets reduced. [**60**] The reduction in the LO peak intensity has been used to asses the doping (surface depletion) of Te-doped (n-type) GaAs nanowires with backscattering configuration [**59**], while the coupled mode has been used to determine carrier concentrations and mobilities in Si-doped (p-type) GaAs nanowires with forward scattering (transmission) configuration [**60**]. Furthermore, resonant Raman scattering measurements have been used to probe local vibrational modes related to Si and Be dopants in GaAs nanowires [**61**]. The locations of such local mode related peaks are different depending on the incorporation site (group III or V) of amphoteric dopants and the measurements hence gave information on the preferential site [**61**].

The Raman measurement procedure in this work was as follows. First, the selected nanowires were located with the video camera mode using a 20x lens after which a 100x lens was selected. Secondly, the 100x video image was used to determine the scan area and the illumination and detection were changed to the laser mode. Finally, the incident and detector polarizers were set before initiating the measurement. The laser power was adjusted as low as possible for the measurements to avoid sample heating as it can e.g. affect the peak positions [**57**] and even cause structural changes and permanent damage [**62**]. Structural quality of the measured nanowires was inferred from the obtained Raman spectra by observing the positions and FWHMs of the TO and LO peaks.

5 Results and discussion

The results and discussion thereof are divided here to focus separately on the nanowire growth, contacting and electrical measurements. First, the doped nanowire sample series are described and the results from SEM and micro-Raman inspections are given in section 5.1. Section 5.2 then discusses the attempt to develop a process for nanowire contacting relying on optical lithography for contact patterning. Finally, the results from the electrical measurements are presented in section 5.3.

5.1 Nanowire growth

Several GaAs nanowire samples were grown in this study with either Zn or Sn doping and varying II/III or IV/III ratios, respectively. Undoped nanowires were additionally grown for reference. The different dopant precursor molar flows and ratios used for growing the nanowires are given in table 3. The nominal and obtained molar flows are calculated from set point and measured gas flow rates, respectively. The samples were grown using the sample preparations, growth recipe and group III and V flows as described in section 4.1. The dopant precursor flows were selected mainly based on previously reported values. The nominal II/III ratios used varied between 0.005 and 0.080 which corresponds to the values previously resulting in successful growth under similar conditions in the same system [**40**]. The TESn precursor was installed to the used MOVPE apparatus during this work and hence previous results were not available. The nominal IV/III ratio was varied between 0.041 and 0.080 corresponding to values reported elsewhere [**31**].

Table 3: Different dopant molar ratios and precursor molar flows used for nanowire growth in this work. The obtained TBAs and TMGa flows were 150.0 μmol/min and 5.97 μmol/min, respectively.

	II/III		**DEZn (μmol/min)**	
Zn doped	Nominal	Obtained	Nominal	Obtained
1	0.005	0.005	0.030	0.030
2	0.010	0.010	0.060	0.060
3	0.020	0.020	0.120	0.120
4	0.041	0.042	0.248	0.248
5	0.080	0.082	0.488	0.487

	IV/III		**TESn (μmol/min)**	
Sn doped	Nominal	Obtained	Nominal	Obtained
1	0.041	0.040	0.250	0.241
2	0.061	0.061	0.376	0.366
3	0.080	0.083	0.504	0.493

For one Zn-doped nanowire sample, however, a slightly modified growth recipe was used. The purpose of this sample was to investigate the two-temperature growth method (as discussed in section 3.1.3). A modest nominal II/III ratio of 0.005 was

used to include the effect of doping and simultaneously keep it to minimum. The only modification to the recipe is that the growth (step 4) is divided to two steps: a 60 s nucleation step at 450 °C and the actual growth step (840 s) at a lower temperature of 390 °C. All molar flows were the same as in the corresponding one-step growth. This sample is referred to as the two-step sample in the following.

Due to the limited accuracy of the mass-flow controllers in the MOVPE, the measured gas flow rates deviated slightly from the set point values for all the precursors. This especially affected the TESn source since its mass-flow controller had to be operated at lower-than-recommended flows to obtain the IV/III ratios without altering the other flows. Furthermore, the cooler of the TESn bubbler liquid bath broke and could not be replaced during this work. The TESn molar flows hence also varied slightly with the bath temperature. The temperature for each growth was recorded and taken into account when converting the gas flow rates to molar flows. However, the temperature variation was not considered significant during any single growth. The nominal bath temperature was 16.7 °C (measured before the growths). The obtained molar flows given in table 3 are calculated from gas flow rates averaged over the measured values during growths. The obtained molar flows of TBAs and TMGa were 150.0 μmol/min and 5.97 μmol/min, respectively, giving a V/III ratio of 25.1. These values were consistent for all the samples. In the following, all given molar flows and ratios refer to the obtained values instead of the nominal values.

5.1.1 SEM

All nanowire growth samples were inspected with SEM after the growth and average lengths, growth rates and tapering were estimated from the SEM images. In order to get a good side-view, the growth substrates were cleaved and the nanowires near the cleavage plane edge were investigated. The axial growth rate is defined here simply

$$\nu_{\mathrm{a}} = \frac{l_{\mathrm{nw}}}{t_{\mathrm{g}}}\,, \tag{36}$$

where l_{nw} is the nanowire length and t_{g} is the duration of the growth step. The nanowire nucleation was assumed to be very fast compared to the long growth time [**29**] and the time taken for the nucleation was therefore not accounted for. Similarly, the radial growth rate is defined here as

$$\nu_{\mathrm{r}} = \frac{r_{\mathrm{b}} - r_{\mathrm{t}}}{t_{\mathrm{g}}}\,, \tag{37}$$

where r_{b} is the nanowire radius at the base and r_{t} is the radius at the tip. The tapering is then obtained as the ratio of the growth rates $\nu_{\mathrm{r}}/\nu_{\mathrm{a}}$. Assuming that both growth rates are constant, the slope $\mathrm{d}r/\mathrm{d}l$ anywhere along the nanowire should be equal to the tapering.

The samples, in general, had a relatively high density of nanowires (Au nanoparticles) and exhibited growth in various directions. This is illustrated in figure 27 that shows tilted top views of the undoped reference sample. The high density and large number of non-vertical nanowires made it difficult to take measures. The other

samples showed the same problems, as would be expected due to the identical sample preparations. Furthermore, the cleaving and handling easily resulted in breaking a significant number of nanowires near the edges, which further reduced the number of nanowires suitable for measurements. Therefore, the values reported here are taken from only few (1 to 15) representative nanowires per sample. Since a statistically significant number of nanowires were not measured, standard deviations for the values are not reported. The accuracy with which measures can be taken from SEM images depends on the magnification. A rough estimate of the accuracy here is that, for long nanowires with length of few tens of μm, the length can be determined to $\pm$ 1 μm. However, the magnification is significantly increased when inspecting the nanowire diameters, and these should be accurate within roughly $\pm$ 10 nm.

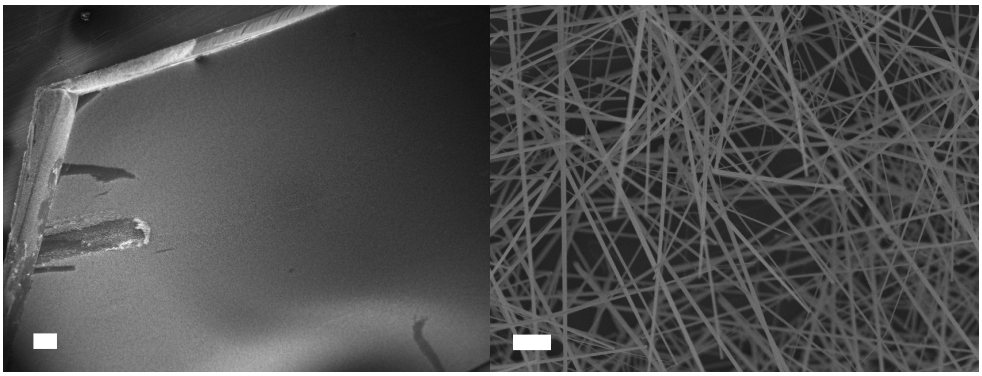

Figure 27: Tilted top view SEM images of the undoped GaAs nanowire reference sample showing high nanowire density and mostly non-vertical growth directions. The scale bars are 200 μm and 2 μm, respectively.

The undoped reference nanowires were observed to grow mostly straight with relatively little kinking or stacking faults. A typical view of these nanowires is shown in figure 28a and a close-up of a single nanowire is shown in figure 28b. The average length of the undoped wires was 27 μm corresponding to an axial growth rate of 30 nm/s. The tapering was found to be in the order of 4 nm/μm when measured from base to tip. However, the slope dr/dl was larger closer to nanowire base compared to middle by a factor of up to 6 indicating that one or both of the growth rates were not constant during the growth. This could be due to e.g. increased radial growth for the lower part of the nanowires when the nanowires have become long enough such that diffusing Ga adatoms are less likely to reach the axial growth interface. Even this rather low tapering leads to thick nanowires with diameters in the order of 300 nm near the base.

The Zn doping was found to have a significant effect on the nanowire growth. Figure 29 shows typical views of the nanowires at the cleavage plane edge for all the Zn-doped samples (The sample with II/III ratio of 0.010 was quite badly damaged during cleaving and subsequent handling and only a couple of intact nanowires were inspected). All samples show similarly high densities and varying growth directions as the undoped reference sample. The lower II/III ratios 0.005 to 0.020 resulted in rather low defect density, while the growth was deemed to have failed for the

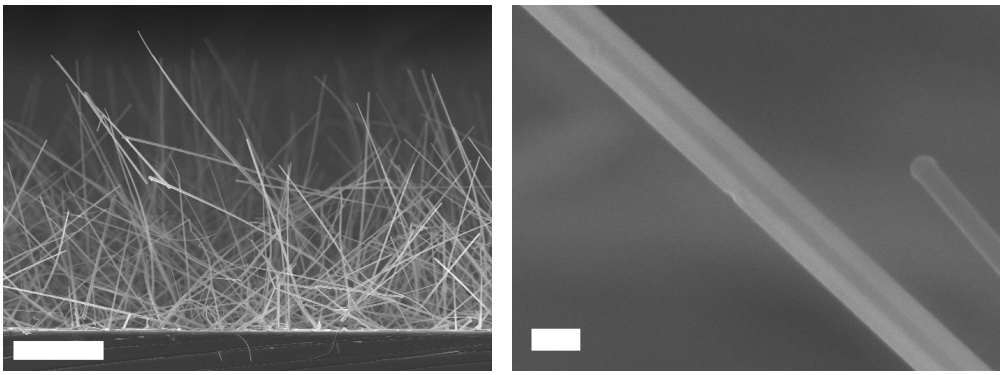

(a) (b)

Figure 28: Representative SEM images of the undoped GaAs nanowires showing an overview (a) and a close-up of a single nanowire (b). The scale bars are 10 μm and 200 nm, respectively.

highest used ratio of 0.082. This qualitative relationship is in good agreement with previous findings [**30**, **38**, **40**]. Figure 30 illustrates the increase in defect density with the II/III ratio increasing from 0.02 to 0.082. For the ratio of 0.082 most of the nanowires experience a total loss of growth direction leading to highly twisted structures. However, these nanowires also tended to have long straight or smoothly kinking sections before the loss of growth direction takes place. This would indicate that the sudden failure in the growth may be a result of a change in the local growth conditions. Regardless, the II/III ratio of 0.08 was considered to be the upper limit at or above which the growth fails with the parameters used here. This upper limit is only about half of that reported in [**40**] where the growth temperature was 470 °C and the molar flows approximately the same.

The average nanowire lengths, growth rates and tapering parameters for the Zn-doped nanowires are given in table 4. These were not measured for the nanowires grown with the II/III ratio of 0.082 since most of them were severely deformed. The growth rate and tapering were not significantly affected by varying the II/III ratio between 0.005 and 0.020. However, the II/III ratio of 0.042 resulted in almost doubling the growth rate. Since the temperature and group III and V flows were not changed, the increased growth rate could result from altered Au nanoparticle phase due to increased alloying of Zn as suggested in [**40**]. Furthermore, the tapering was not significantly reduced which indicates that the increased growth rate was not due to suppression of radial growth.

For the two-step sample (with II/III ratio 0.005), the average length of the wires was 27 μm, corresponding to an axial growth rate of 30 nm/s, and the tapering was in the order of 3 nm/μm when measured from base to tip. However, the slope $\mathrm{d}r/\mathrm{d}l$ was smaller near nanowire top and middle compared to base by a factor of 10 or more. These results indicate that the two-step growth indeed reduces the tapering significantly, as was expected. On the other hand, the fraction of kinked nanowires seemed to have increased for this sample, possibly due to the temperature gradient when cooling from the initial 450 °C to the lower growth temperature of 390 °C.

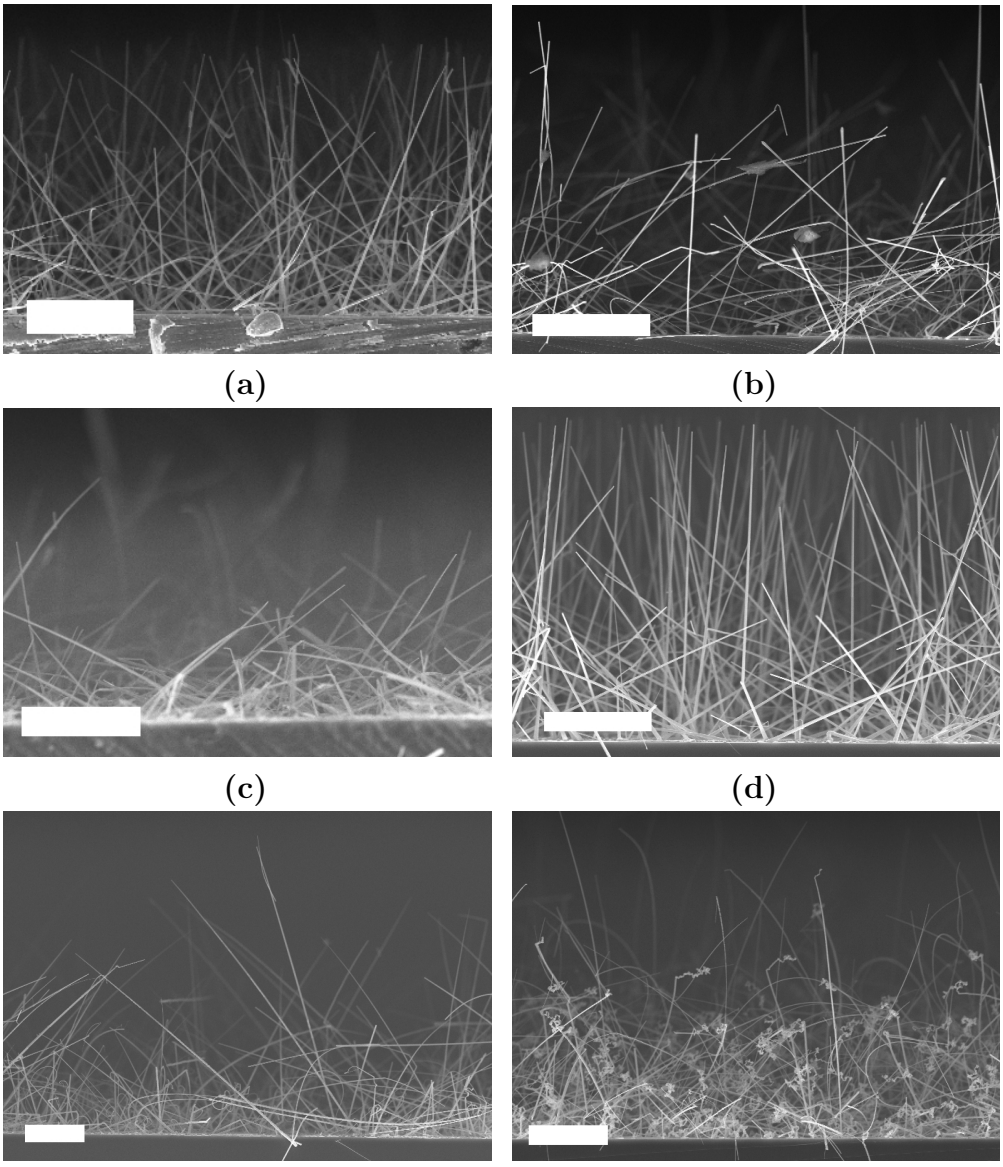

Figure 29: SEM images showing an overview of Zn-doped nanowires with II/III ratio of (a) 0.005 (b) 0.005 (two-step) (c) 0.010 (d) 0.020 (e) 0.042 and (f) 0.082. The scale bars are 10 μm.

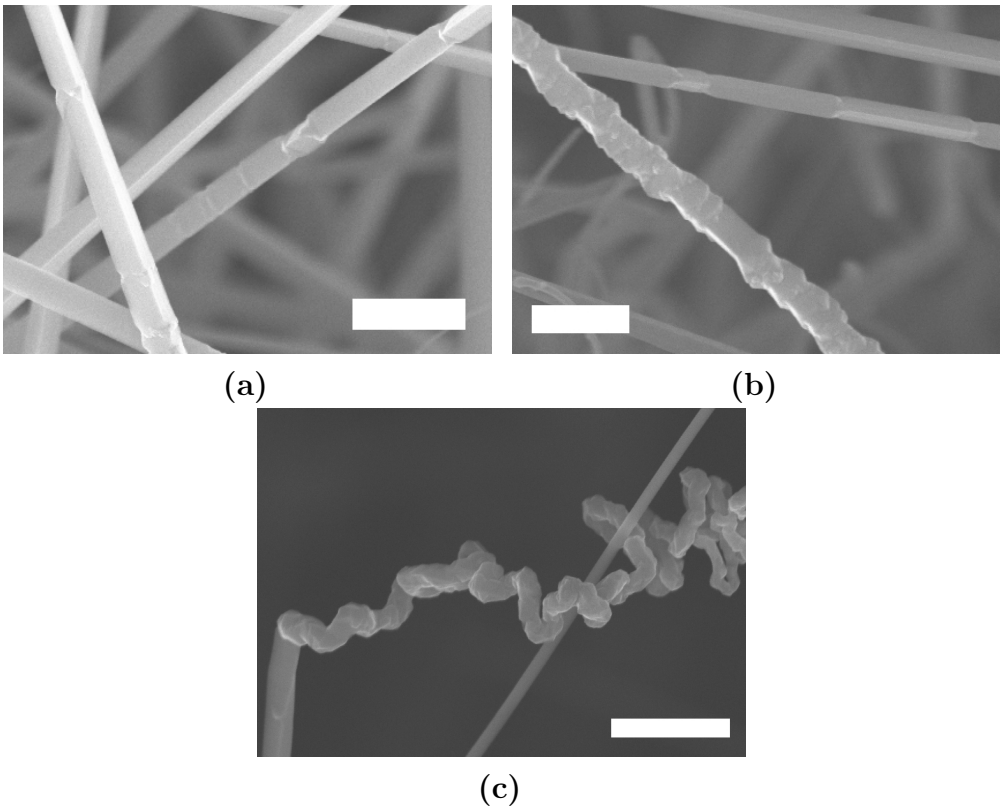

Figure 30: SEM images of the nanowire growth defects with II/III ratio of (a) 0.020, (b) 0.042 and (c) 0.082. The scale bars are 1 μm.

Table 4: Average length, growth rate and tapering for the grown Zn-doped GaAs nanowires. The values for the undoped nanowires are also given for comparison. (* Only a couple of nanowires were measured)

II/III ratio	**Length (μm)**	**Axial growth rate (nm/s)**	**Tapering (nm/μm)**
0.000	27	30	4
0.005	24	27	5
0.010*	20	22	6
0.020	28	31	5
0.042	50	56	4

The Sn doping was found to mainly effect the nanowire growth rates. Figure 31 shows typical views of the nanowires at the cleaved edge for all the Sn-doped samples. The doping did not cause any discernible increase in stacking fault density or kinking compared to the reference. Consequently, no upper limit for the IV/III ratio was observed here. However, there seemed to be a significant increase in additional growth of very thin, strongly kinked nanowires and nanowire crawling along the substrate. Moreover, the nanowire (Au nanoparticle) density might have been even higher than in the reference.

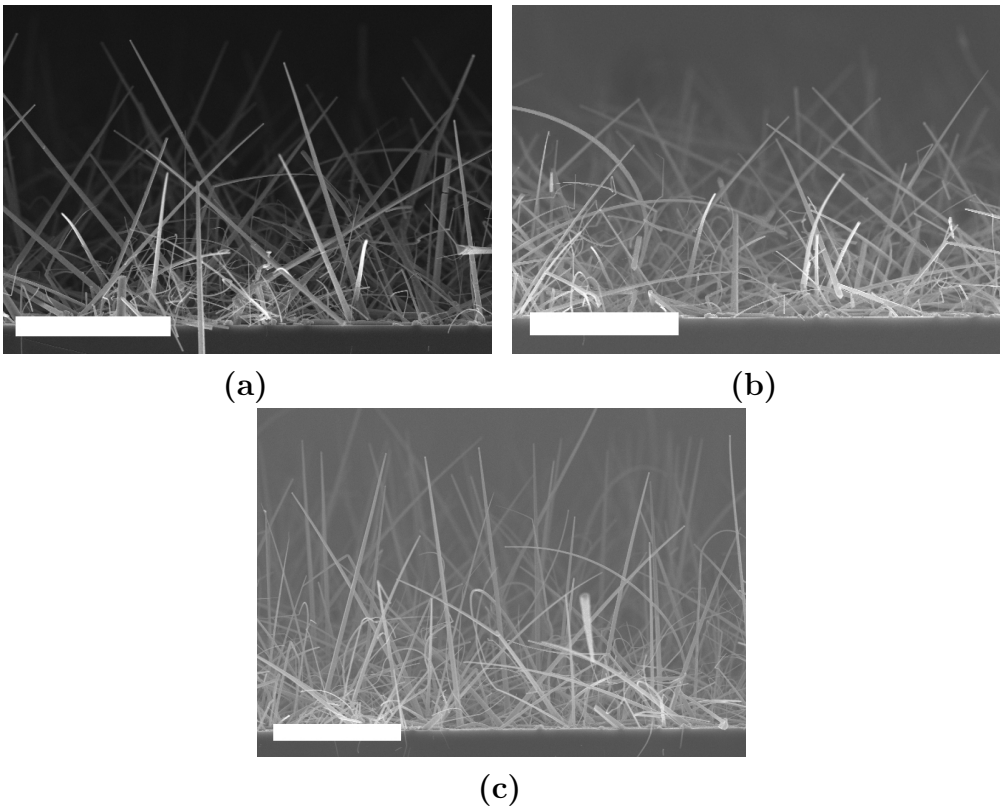

Figure 31: SEM images showing an overview of Sn-doped nanowires with IV/III ratio of (a) 0.040 (b) 0.061 and (c) 0.083. The scale bars are 10 μm.

The average nanowire lengths, growth rates and tapering parameters are given in table 5. There is a striking increase in tapering compared to the Zn-doped or the undoped nanowires accompanied with reduced growth rate. It seems that the increased radial growth took place at the expense of axial growth due to material competition. However, it is unclear why the radial growth would be enhanced so by the presence of TESn. The minute observable effect of Sn doping (with TESn) on nanowire defect density in the straight grown nanowires is in agreement with what has been reported before **[31**, **38]**, whereas the increased tapering is not. On the other hand, the results are not quite comparable since a two-step temperature process was used in the references to strongly suppress the radial growth for doped and undoped nanowires alike.

Table 5: Average length, growth rate and tapering for the grown Sn-doped GaAs nanowires. The values for the undoped nanowires are also given for comparison.

IV/III ratio	**Length (μm)**	**Axial growth rate (nm/s)**	**Tapering (nm/μm)**
0.000	27	30	4
0.040	18	20	11
0.061	16	18	7
0.083	22	24	9

Overall, most of the nanowires did not grow in the [111] vertical direction, which is the typically preferred III–V nanowire epitaxial growth direction from (111) oriented surfaces [**19**]. This is most likely due to the native oxide layer on the Si substrates that was not etched away prior to growth. However, some of the non-vertical nanowires might still have grown in the epitaxial equivalent ⟨111⟩ directions (19.5° from the substrate surface) for which facets may be formed due to the alloying of Au with Si [**63**]. Some nanowires might also have initially nucleated in the vertical [111] growth direction but then kinked to another direction or first crawled along the substrate and then kinked upwards due to the prevailing local growth conditions. Furthermore, the Au nanoparticle density was excessively high making the SEM inspection more difficult. The high density of growing nanowires might also have affected the local growth conditions (as discussed in section 3.1.3).

5.1.2 Micro-Raman

Micro-Raman measurements were conducted on nanowires detached from the growth samples to complement the inspection made with SEM and hence obtain further information on the quality of the grown nanowires and how it is affected by the addition of doping. While Raman measurements do not provide information on the crystal structure directly like TEM, they are fast and require little sample preparation. Therefore, Raman measurements make it feasible to inspect a larger number of nanowires and hence better detect possible variations within a single batch [**57**]. Several nanowires from each inspected sample were scanned spatially and the Raman spectrum was recorded for each point in the scan. The locations and FWHM values of the peaks were then obtained by fitting the spectra with a constant background level and Lorentzian curves of the form

$$y(x) = \frac{y_\mathrm{p}}{1 + 4\left(\frac{x - x_\mathrm{p}}{w}\right)^2}, \tag{38}$$

where y_p is the peak intensity, x_p is the peak position and w is the FWHM of the peak. Finally, the obtained values of the TO and LO peaks were compared to the previously reported values in [**56**, **58**].

The peak intensities in the Raman spectra were relatively low compared to the background noise level with laser power of 372 μW and became indiscernible at 27.2 μW (the laser powers here refer to values measured before the objective lens since these were considered more reliable than the powers measured after the 100x lens). However, when the power was increased to obtain better signal-to-noise ratio, the beam tended to burn the nanowires at the power of 6.05 mW and above as shown in figure 32. It is also likely that heating due to the beam affects the measurements already at lower power levels. For example, Begum et al. [**57**] observed shifts of ~ 5 cm^{-1} in the TO and LO peak positions with a given laser intensity (power). This heating related shift was removed by dropping the intensity by a factor of 10. Furthermore, their initial laser intensity was already low enough to not cause any damage to the wires. Therefore, it was deemed here that the laser power should be below 600 μW and the 372 μW setting was selected. It might still be possible

that the measured nanowires were heated by the beam and consequently show slight additional shift in the TO and LO peaks.

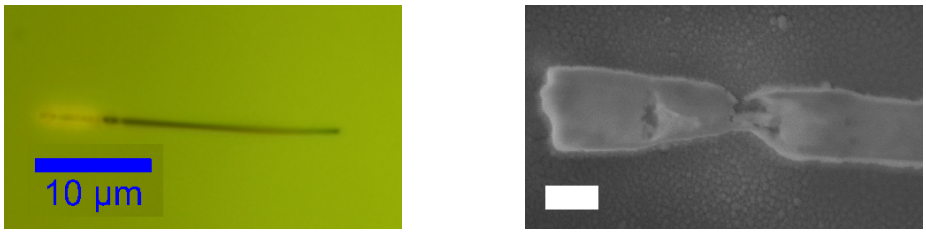

(a) **(b)**

Figure 32: Laser beam induced damage in a nanowire as observed with the optical Raman microscope (a) and SEM (b). The scale bar in (b) is 200 nm.

The intensities of the TO and LO peaks were found to strongly depend on the polarization of incident light. The TO peak intensity was higher when the incident and analyzed polarizations were parallel to the nanowire axis, whereas the LO peak was practically only discernible when the polarizations were perpendicular to the nanowire axis. This polarization dependence of the TO peak agrees well with that reported in [**56**]. Interestingly, the polarization dependence of the LO peak, in turn, is in agreement with that reported in [**60**] for forward scattering configuration. The polarizations, however, could not easily be aligned exactly parallel or perpendicular to the measured nanowires. Instead, the polarizations were set along either the vertical or horizontal axis of the scan and the measured nanowires were roughly aligned with one of these axes. Furthermore, measuring nanowires aligned with either of the axes allowed for smaller scan grids and hence longer integration time to improve the signal in the spectra.

The undoped GaAs nanowires were used in the Raman measurements to provide a reference against which the results from the doped nanowires could be compared. Figure 33a shows a SEM image of a representative undoped GaAs nanowire, figure 33b shows the coordinate axes in the Raman scan and figures 33c and 33d show peak fits for one point on this nanowire with the polarizations set along x- and y-axis, respectively. Variation of the TO and LO peaks along the nanowire are additionally shown in figures 34a and 34b, respectively. Furthermore, Raman spectra from several locations along four undoped nanowires were analyzed. The TO peak position varied between 262.7 ... 268.7 cm^{-1} with FWHM values of 5.4 ... 8.6 cm^{-1} and the average values were 265.8 cm^{-1} and 6.9 cm^{-1}, respectively. The LO peak position, in turn, varied between 283.2 ... 289.7 cm^{-1} with FWHM values of 6.1 ... 10.1 cm^{-1} and the average values were 288.3 cm^{-1} and 7.2 cm^{-1}, respectively. No E2 peak was detected for any of the nanowires.

These results indicate that the undoped nanowires had ZB structure and rather good quality. The TO peak position values correspond to those reported in [**56**] and [**58**] and are downshifted with respect to the reported bulk value by only ~ 3 cm^{-1} on average. On the other hand, the FWHM values are clearly larger than the 4.8 cm^{-1}

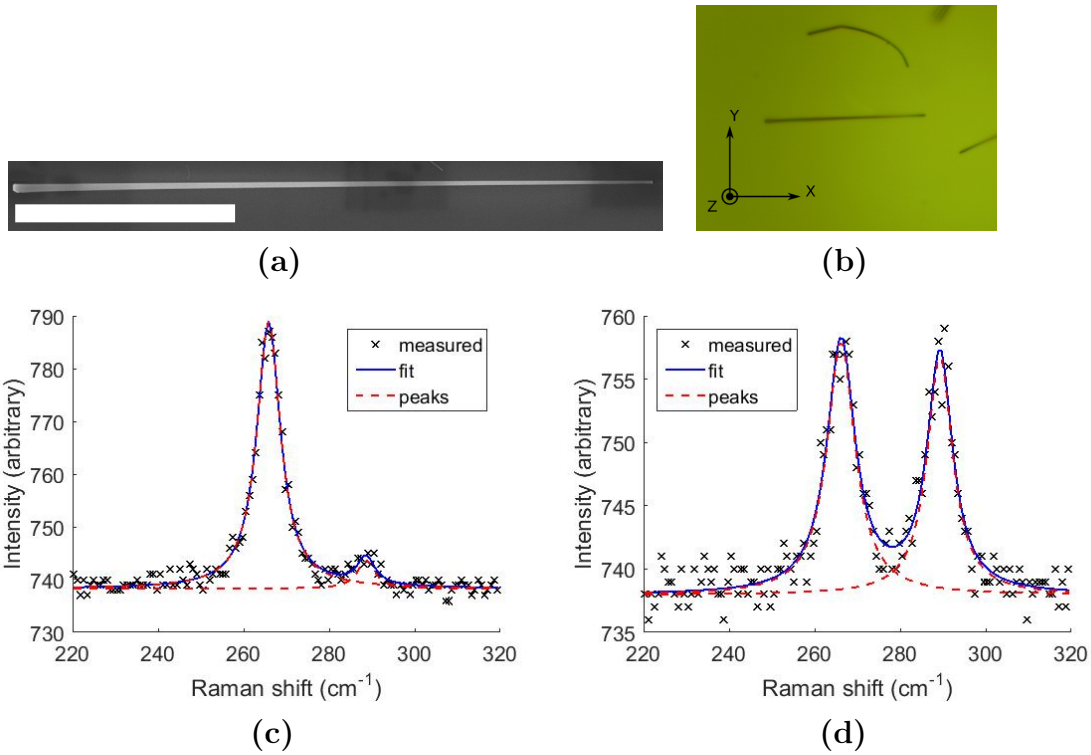

Figure 33: Micro-Raman measurement of a representative undoped GaAs nanowire: (a) SEM image of the nanowire, (b) video image and scan axes, (c) peak fit for a single Raman spectrum with polarizations along the x-axis and (d) peak fit for a single Raman spectrum with polarizations along the y-axis. The scale bar in (a) is 10 μm.

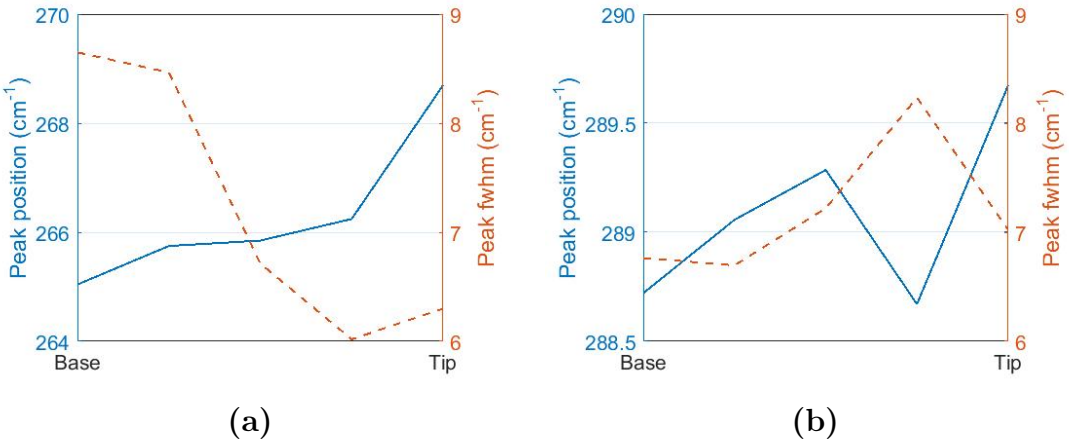

Figure 34: TO (a) and LO (b) peak positions and FWHM values along the representative undoped GaAs nanowire.

and 2.8 cm^{-1} reported in [**56**] for nanowires and bulk, respectively. The LO peak downshift from the value reported in [**58**] was slightly larger, $\sim$ 4 cm^{-1} on average, and the FWHM values were larger by $\sim$ 3 cm^{-1} on average. However, a poorly resolved SO peak might have accompanied the LO peak increasing its apparent shift and FWHM values.

The Zn-doped nanowires were found to exhibit worse quality with increasing II/III ratio, hence supporting the conclusion obtained by inspection of the SEM images. Figure 35 shows the TO and LO peak values for the Zn-doped nanowires. For each sample, Raman spectra from several locations over 3 to 6 nanowires were fitted to obtain these values. As seen in the figures, there is a clear trend that increasing doping leads to larger peak shifts and FWHM values, although the lowest-doped sample actually showed slightly better values than the undoped reference. The two-step sample nanowires (also with II/III ratio of 0.005) showed slightly worse values but still clearly better than the nanowires with II/III ratio of 0.020 and 0.042. Furthermore, the LO peak was not detected from the nanowires with these two high II/III ratios even when relatively good signal for the TO peak was obtained. The absence of the LO peak with high II/III ratios might be an indication of high doping levels as discussed in section 4.7.

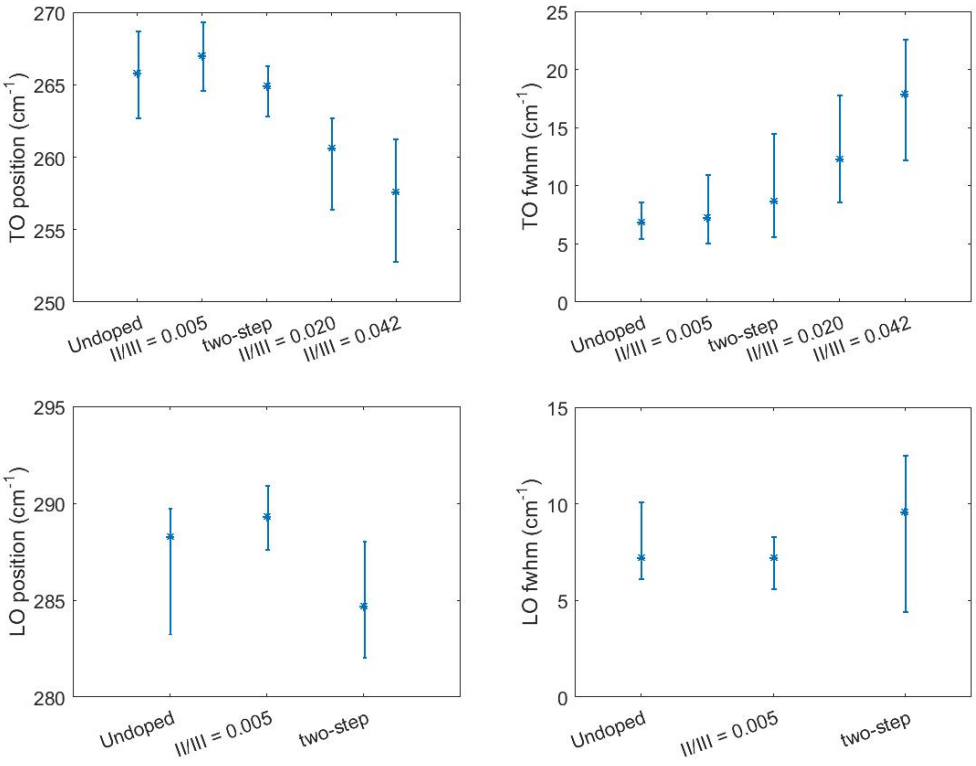

Figure 35: TO and LO peak values obtained for the Zn-doped nanowires including the two-step sample. The dots indicate average values and the bars indicate the lowest and highest individual values. The values for the undoped nanowires are also shown for comparison.

The severely tapered nanowires from the Sn-doped samples mostly showed weak signals with recognizable TO peak only near the tip of the nanowires. An example of this is shown in figure 36 for a representative nanowire with IV/III ratio of 0.061. The peak fit at the tip of this nanowire gave TO peak position of 258.2 cm^{-1} and FWHM of 10.1 cm^{-1}. For a nanowire with IV/III ratio of 0.083 showing similar spectra, the peak fit at the tip gave TO peak position of 260.6 cm^{-1} and FWHM of 8.6 cm^{-1}. Additionally, one of the inspected nanowires with IV/III ratio of 0.083 showed relatively good TO peak signal throughout. The evolution of the fitted TO peak position and FWHM along this nanowire is shown in figure 37. Again, the region near the other end showed much smaller peak shift and broadening. Since the region near the nanowire tip has less radial growth than the base, these results might indicate that the thick tapering shell resulting from radial growth has significantly worse structural quality than the axially grown nanowire below. Furthermore, like with the Zn-doped nanowires with higher II/III ratios, no clear LO peak was detected for any of the Sn-doped nanowires. This might indicate high doping levels, unless the signals were simply too weak or the structural quality too poor.

It should be noted that the TO peak positions with the largest shifts obtained in this work are actually closer to the WZ nanowire E2 peak at 254 cm^{-1} reported in [**56**]. However, were these peaks actually E2 rather than TO, they would instead have a negligible shift. In that case, the WZ nanowires should also exhibit the TO peak around 266 cm^{-1} with correspondingly small shift. Furthermore, the E2 peak is expected to show larger intensity with polarizations perpendicular to the nanowire axis, i.e. the opposite of the expected TO peak behavior. Neither simultaneous E2 and TO peaks nor the expected E2-type peak intensity variation with polarization was observed here. Therefore, the peaks were attributed to the TO mode despite the large shifts.

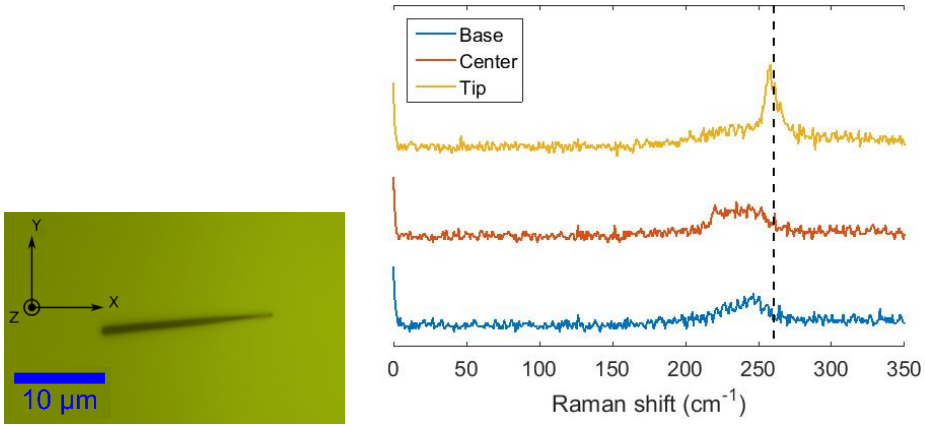

Figure 36: Video image and scan axes of a representative Sn-doped GaAs nanowire with IV/III ratio of 0.061 (a) and corresponding Raman spectra (b). The polarizations were along the x-axis. The spectra are shifted vertically for easier comparison and the black dashed line is a guide for the eye.

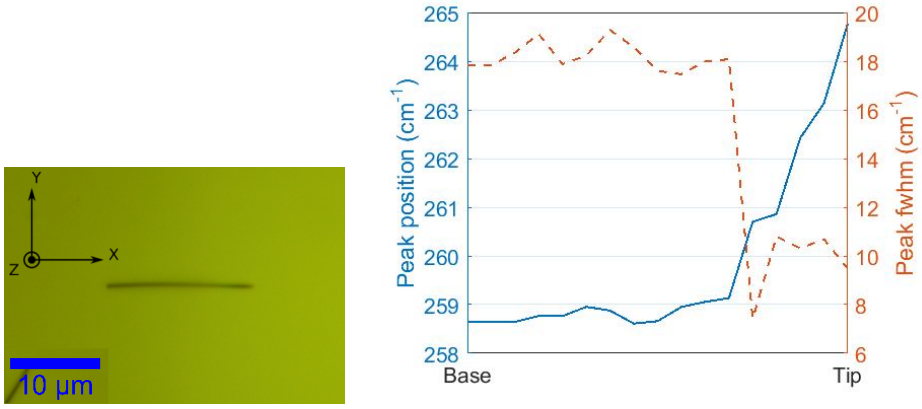

(a) (b)

Figure 37: Video image and scan axes of a Sn-doped GaAs nanowire with IV/III ratio of 0.083 (a) and the variation in the TO peak fit results along the nanowire axis from left to right (b). The polarizations were along the x-axis.

5.2 Nanowire contacting

The metal contacting for the electrical measurements was done by first dispersing nanowires to a substrate and then evaporating metal and patterning it via the lift-off process. An attempt was made to develop a process for this that would employ optical lithography with a large number of regular contact patterns instead of defining contacts for each nanowire individually with EBL. Since optical lithography is not capable of such high resolution as EBL, the contact fingers and separation had to be at least 1 μm wide. Furthermore, in order to make the fringing capacitances negligible and hence the back gate capacitance approximation (equation 32) more valid, the contact spacing should preferably be larger. For these reasons, a four-point contact scheme requires nanowires with length of ~ 7 μm at the very least in the case of smallest possible contacts and perfect alignment. Moreover, only a single nanowire should be contacted by one set of contact fingers to avoid ambiguity in analyzing the measurements. Therefore, the nanowires needed to be broken off the growth substrate as near the base and dispersed with as little agglomeration as possible, preferably with some defined alignment. Three different methods for dispersing the nanowires were hence investigated here.

Nanowire dispersion by simple mechanical scraping was tried first. In this method, a small sharp intermediate carrier (e.g. the corner of a cleanroom paper) is used to scrape nanowires from the growth substrate and then deposit the detached nanowires to the contacting substrate by scrubbing the carrier against it. This approach was fast but led to very nonuniform distribution of the nanowires on the substrates with significant agglomeration. Worse yet, the nanowires on the growth substrate tended to break at random points along the axis which resulted in mostly too short nanowire pieces. This approach hardly ever resulted in successfully contacted nanowires.

In the second technique, the nanowire growth substrate was immersed in ethanol and the nanowires were detached by ultrasonication. The nanowires were then dispersed on the contacting substrates by drop casting and subsequent evaporation of the liquid. This technique has been used in conjunction with EBL elsewhere (e.g. [**14**, **44**]). In this work, it did result in longer nanowire pieces and even whole nanowires detached near the base. Furthermore, the agglomeration of nanowires was significant only near the locations where the liquid had receded to small droplets before complete evaporation. The random nanowire positions and alignment still significantly reduced the chance to obtain four-point contacts.

Thirdly, a technique similar to that used in [**64**] was employed. First, the nanowire growth substrate is placed upside down on the contacting substrate with patterned resist and slid along it for few millimeters while applying manual pressure. The nanowires then break off the growth substrate and end up either on the resist or the substrate exposed by the resist openings. When the resist is removed with acetone, nanowires on top of the resist get washed away while those on the substrate remain. This allows nanowires to be positioned on the sample in a controlled manner with a rough alignment with the sliding direction. In this work, the substrate contact and the sliding was achieved by using a manual micromanipulator stage. The alignment of the resist openings and the contact pattern was achieved by using markers etched with RIE. This approach significantly improved the chances of positioning metal contacts on top of the dispersed nanowires.

While the third approach was deemed here as the best match with optical lithography, it was not without shortcomings. For example, it was not uncommon that several nanowires occupied the same resist openings and ended up contacted simultaneously. Figure 38a shows an example of successful alignment while figure 38b shows an example of several nanowires contacted simultaneously. However, this issue may be solved by better optimization of the size and shape of the openings and by reducing the nanowire density on the growth substrate. The process would also be improved if the nanowires grew straight in the vertical [111] direction. The real problem, instead, was achieving smooth substrate contact. In most cases, one end of the growth substrate scratched the contact substrate crushing the nanowires while the opposite end was not yet in contact. In the end, this technique was not yet optimized in this work and the yield of four-point contacts remained far from what was initially expected.

The contact metal evaporation and lift-off produced more reliable results and the contact fingers were mostly smooth and well-defined. The evaporated AuZn alloy (95–5 wt%) for contacting the Zn-doped GaAs nanowires had rather good quality (as shown in figure 39a) and resulted in near-ohmic contacts in some cases. However, the Ni/AuGe/Ni metal stack (AuGe composition 88–12 wt%) evaporated for the Sn-doped samples had poor quality as shown in figure 39b. Despite this, some of the contacted Sn-doped nanowires showed near-ohmic current–voltage behavior. On the other hand, when the nanowires had significant tapering or the metal thickness was too small, partial or insufficient metal coverage was sometimes observed leading to a poor or no contact at all. Gaps resulting from such insufficient metal thickness and coverage are shown in figure 40.

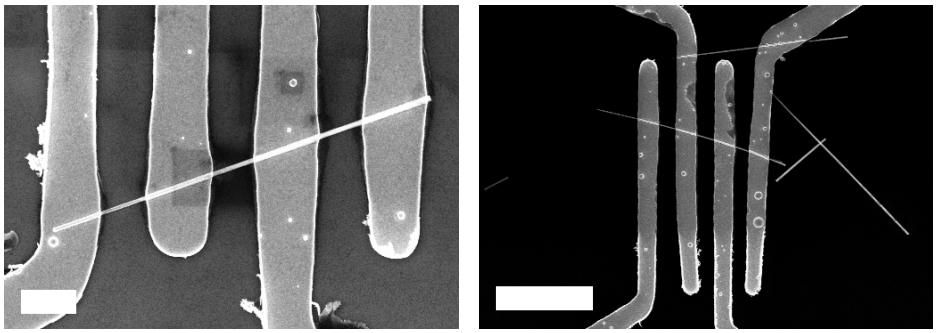

(a) **(b)**

Figure 38: SEM images of contacted nanowires dispersed with the substrate contact method showing (a) successful positioning and (b) several nanowires in the same opening. The scale bars are 2 μm and 10 μm, respectively.

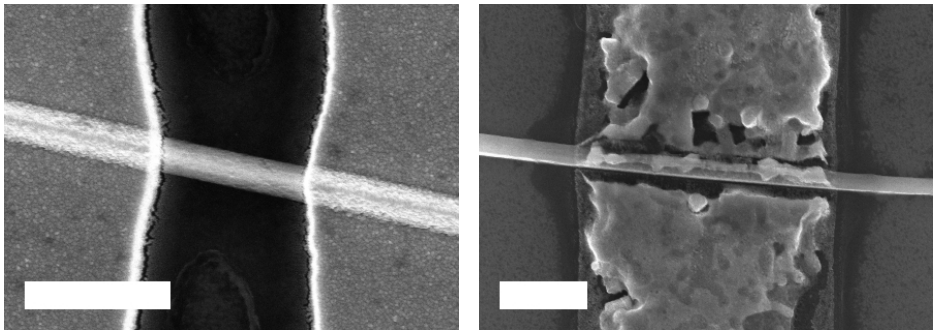

(a) **(b)**

Figure 39: SEM images of (a) AuZn alloy and (b) Ni/AuGe/Ni metal stack contacts. The scale bars are 1 μm.

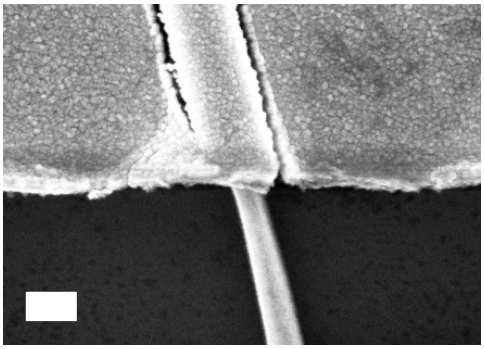

Figure 40: SEM image of gaps in the metal contact to a nanowire. The scale bar is 200 nm.

5.3 Electrical measurements

Due to the issues with nanowire contacting, functioning four-point contacts were scarce and the nanowires with two and three contacts were hence also employed. When the nanowires not in contact, giving currents below 1 nA or showing SCL current were excluded, a total of 19 nanowires (9 Zn-doped and 10 Sn-doped) were usable in the measurements. Clearly, this sample size is neither statistically significant nor sufficient to draw definite conclusions. Nevertheless, it should suffice to give some indication of how the resistivities, mobilities and carrier concentrations varied with II/III and IV/III ratios.

The drain–source current–voltage and the transconductance measurements were done subsequently for each nanowire. For all two-point ohmic (or near-ohmic) contacts, the contact resistances were assumed to be negligible. For the Schottky-type two-point contacts, the nanowire resistance was approximated with the differential resistance in the linear part of the current–voltage curve at higher voltages (if observed). For three-point contacts, in turn, one of the contact resistances (voltage drop) was measured and the other was assumed to behave similarly taking into account the reversed voltage polarity over the contact. No attempt was made to correct for the effect of contact resistances on the obtained transconductances or mobility calculation.

5.3.1 Current–voltage measurements

Contacting and current–voltage measurements were realized for those Zn-doped nanowires with II/III ratio of 0.010, 0.020 and 0.042. The few contacted nanowires with II/III ratio of 0.005 either conducted no current or showed currents below 1 nA which would indicate that either the nanowires were actually not in contact or that they grew practically undoped. Nanowires with II/III ratio of 0.042 showed mostly ohmic contacts while nanowires with II/III ratios of 0.020 and 0.010 showed mostly non-linear current–voltage behavior and smaller currents. The average obtained resistivities (excluding the effect of surface depletion) were 0.0052 Ωcm, 0.0076 Ωcm and 24 Ωcm for II/III ratios 0.042, 0.020 and 0.010, respectively. These results indicate that the Zn doping had a clear dependence on the II/III ratio. However, the resistivity with II/III ratio of 0.010 is likely overestimated here due to two-point measurements and neglecting the surface depletion. On the other hand, a couple of the nanowires with II/III ratio of 0.010 showed a slope of 2 in the $\log(I)$ vs $\log(V)$ plots (an example of which is given in figure 41) indicating SCL behavior and hence possibly even full depletion. Therefore, the doping might have varied considerably between nanowires.

Four-point contact measurements for nanowires with II/III ratio of 0.042 yielded small but relatively significant contact resistances. Figure 42 shows an ohmic current–voltage curve measured from the center part of a nanowire with II/III ratio of 0.042 while the outer contacts were used to measure contact resistances (voltage drops). The obtained nanowire resistance was 3110 Ω and the drain and source contact resistances were 1150 Ω and 640 Ω, respectively, corresponding to an average specific contact resistivity of $\sim 7 \times 10^{-6}$ Ωcm^2 (assuming that the metal covers ~ 75 % of the nanowire circumference). This means that even with the highest doping and

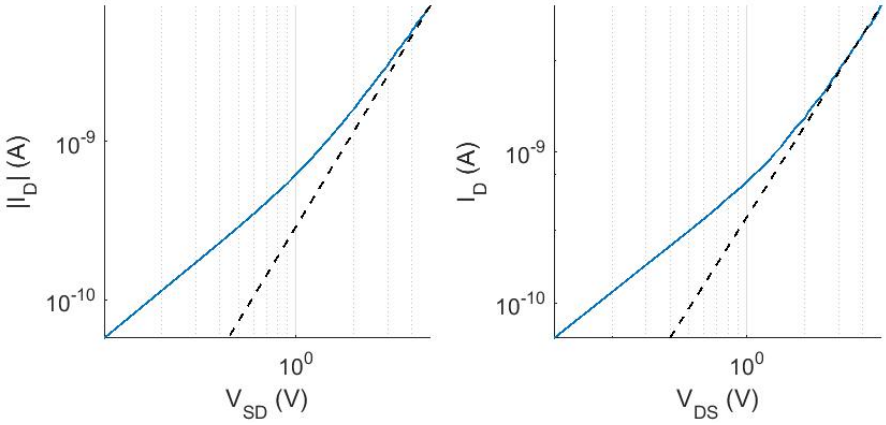

Figure 41: Possible SCL current behavior in a nanowire with II/III ratio of 0.010 at V_{DS} voltages above ~ 2 V. The black dashed line corresponds to an exact slope of 2.

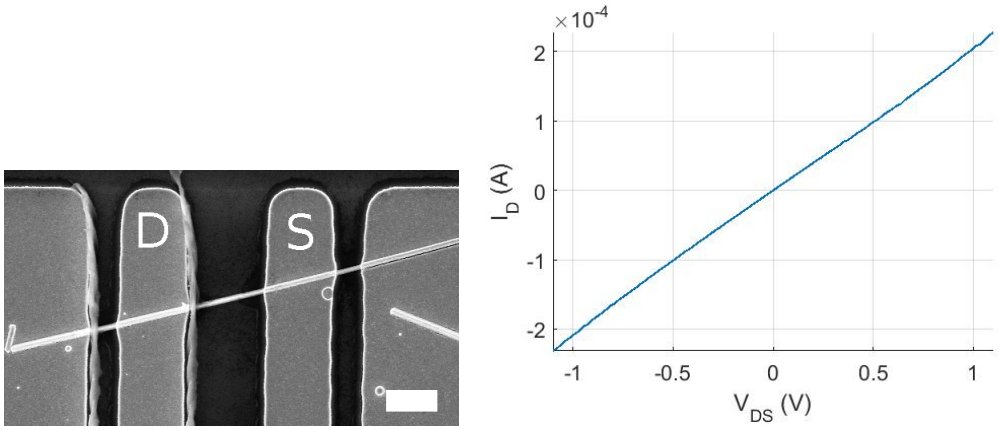

(a) **(b)**

Figure 42: SEM image (a) and measured current–voltage curve (b) of a four-point contacted nanowire with II/III ratio of 0.042. The scale bar in (a) is 2 μm.

ohmic contacts the contact resistances constituted a significant portion of the total resistance, although neglecting them would still give the correct order of magnitude for the nanowire resistance. Therefore, the resistivities obtained here from any of the two-point measurements should be considered only indicative. Furthermore, the transfer length L_{T} was around 1 μm which is clearly shorter than the ~ 3 μm contact lengths. As discussed in section 4.6, this implies that the middle contacts would disturb the current flow in a normal four-point measurement configuration, especially since the contacts are relatively long compared to the total nanowire length between the outer contact fingers (~ 11 μm).

For the Sn-doped nanowires, contacting and current–voltage measurements were realized with IV/III ratios of 0.061 and 0.083. Both ohmic and non-linear Schottky-type current–voltage behaviors were observed with nanowires of either doping but no

clear SCL current–voltage behavior was found in any of the nanowires. The obtained resistivity values (excluding the effect of surface depletion) varied considerably. However, most of the measurements were conducted with two-point contacts and the contact resistances were likely to be relatively high due to the poor quality of the metalization.

5.3.2 FET measurements

The obtained (apparent) transconductances indicated p-type doping with Zn as the I_D current magnitude increased with increasing (negative) V_{GS} voltage. Correspondingly, n-type doping was indicated with Sn as the I_D current increased with increasing V_{GS} voltage. However, three of the Sn-doped nanowires indicated p-type doping instead. It should be possible that under some local growth conditions the Sn atoms would rather substitute an As atom in the GaAs lattice and cause p-type doping, although this was not expected. Regardless, these three nanowires were excluded from the results.

In general, the transconductance values obtained with the back-gate configuration were low and the measurements contained significant noise and instabilities as seen in figure 43. The noise and variation in the transconductance measurements might be at least partially explained by surface state charging and discharging due to the lack of surface passivation and by the back-gate field simultaneously affecting the contacts in addition to the nanowire channel. Furthermore, the SiO_2 layer thicknesses were 300 nm and 86 nm for the Zn- and Sn-doped samples, respectively which are both quite large values for a transistor gate thickness. On the other hand, the achievable drain current control with the gate voltage is relatively small when the nanowire is highly doped (i.e. the gate voltage required for depletion is very high). Additionally, large contact resistances relative to the nanowire resistance work to reduce the (apparent) transconductance and low values could hence be expected.

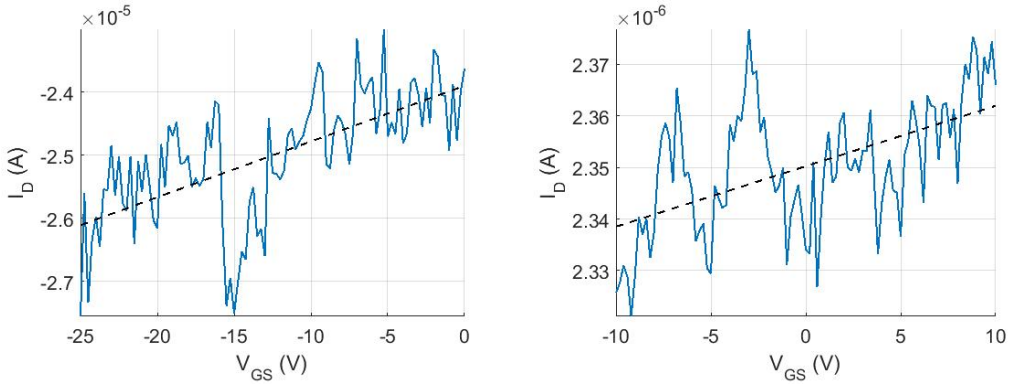

Figure 43: Back-gate FET transconductance current–voltage curve typical for (a) the Zn-doped and (b) the Sn doped nanowires. The V_{GS} voltages refer to the measurable values and the black dashed lines denote best fit for the (apparent) transconductance.

In order to further investigate the issues with transconductance measurements, top-gate structures were fabricated on one of the samples with Zn-doped nanowires (II/III ratio 0.042). The sample was first coated with 37 nm of HfO_2 in an atomic layer deposition reactor after which the top-gate metals were fabricated using the same procedure as with the contact patterns. Figure 44 shows the transconductance current–voltage curves using the back-gate and top-gate configurations for a four-point contacted nanowire (the same as already shown in figure 42a). As seen in figure 44, the top-gate configuration yields much improved current behavior with negligible noise. Furthermore, measured currents were also more stable with the top-gate configuration. Table 6 shows the measured and calculated values for these two measurements. The calculations were done using the back-gate capacitance approximation of equation 32 and the equation 33 for the top-gate. When calculating the capacitances, the effective dielectric constant for the back-gate system was $\varepsilon_{r,eff} = 2.25$ and HfO_2 dielectric constant was $\varepsilon_r = 25$ as in **[54]**. Furthermore, the surface depletion was accounted for. In general, the top-gate results yielded lower mobilities than with back-gate measurements by roughly a factor of 10. It is likely that the disagreement is mostly due to the error in the capacitance calculations, both of which are only rough approximations. This would suggest that there is possibly a relatively high systematic error in the obtained mobilities and hence carrier concentrations.

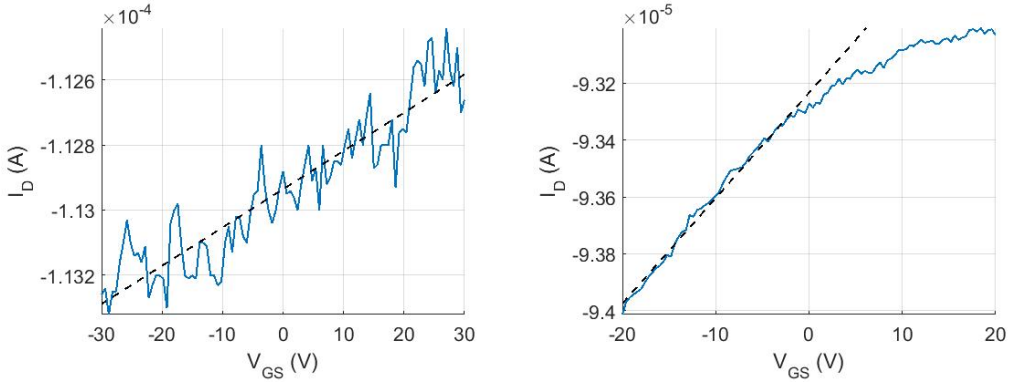

(a) **(b)**

Figure 44: Both (a) a back-gate and (b) a top-gate FET transconductance current–voltage curve for the same nanowire. The V_{GS} voltages refer to the measurable values and the external V_{DS} voltages were -0.5 V and -0.3 V, respectively. The black dashed lines denote best fit for the (apparent) transconductance.

Table 6: Values calculated from transconductance measurements with both a back- and a top-gate.

	g_m (nS)	V_{DS} (V)	C_{gl} (aF/μm)	L_{ch} μm	μ_h (cm^2/Vs)
Back-gate	11.8	-0.5	65	3.03	10
Top-gate	37.0	-0.3	5100	3.03	0.7

The calculated resistivities and mobilities as a function of the II/III and IV/III ratio are shown in figures 45 and 46, respectively. Qualitatively, it is expected that the resistivity increases with reduced doping and the mobility either increases due to reduced scattering from dopant atoms or stays approximately the same if scattering due to other defects or surfaces dominates. Despite the large variation in the obtained values, these expectations are mostly met. However, the average resistivities of the Sn-doped nanowires rather seemed to stay constant. Furthermore, the mobilities obtained from the nanowires with II/III ratio of 0.010 are suddenly clearly lower than with higher II/III ratios. Based on the SEM and micro-Raman measurements the nanowires with II/III ratio of 0.010 should be less defective and the drop in mobility therefore indicates error in the results. Since these values were obtained from two-point measurements, this might be due to contact resistances constituting larger fraction of the total resistance leading to underestimation of the mobilities. Overall, it is unclear to what degree the low mobility values here could be due to increased scattering from defects and due to error in the estimation. With either type of doping, the obtained surface depletion layer widths were less than 10 % of the nanowire radii and were hence of rather small significance.

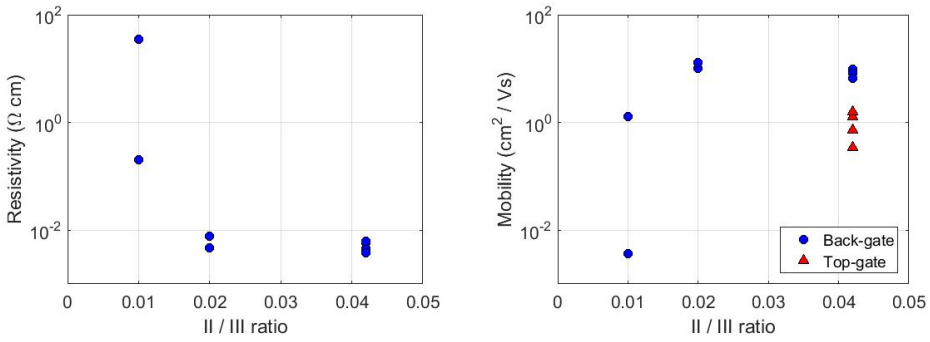

Figure 45: Calculated resistivities (a) and mobilities (b) as a function of II/III ratio.

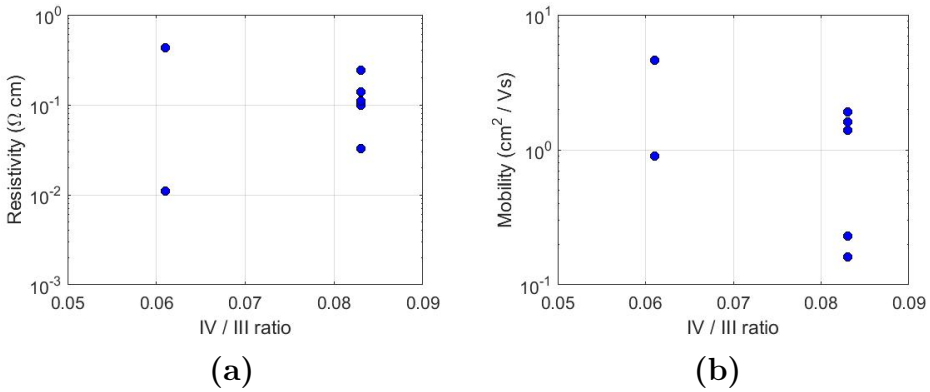

Figure 46: Calculated resistivities (a) and mobilities (b) as a function of IV/III ratio.

The calculated carrier concentrations as a function of the doping are shown in figure 47. The results indicate that, with Zn doping, the carrier concentration had approximately log-linear dependence on the II/III ratio. Similar log-linear dependence was also observed in [**30**], where carrier concentrations of 4.6×10^{18} cm^{-3} and 2.3×10^{19} cm^{-3} were estimated with II/III ratios of 0.0008 and 0.008, respectively. As can be seen in figure 47a, the values obtained here agree quite well with those results. On the other hand, with Sn doping and IV/III ratios between 0.04 and 0.08, the carrier concentrations obtained in [**31**] varied in the range 7×10^{17}...2×10^{18} cm^{-3} and the variation was mainly attributed to axially non-uniform doping profiles. The estimated carrier concentrations are here over an order of magnitude higher, but there might well be non-uniformity in the doping since the change with IV/III ratio seems to be smaller than the variation within nanowires with the nominally same doping. However, the unknown and possibly large contact resistances might contribute to this variation.

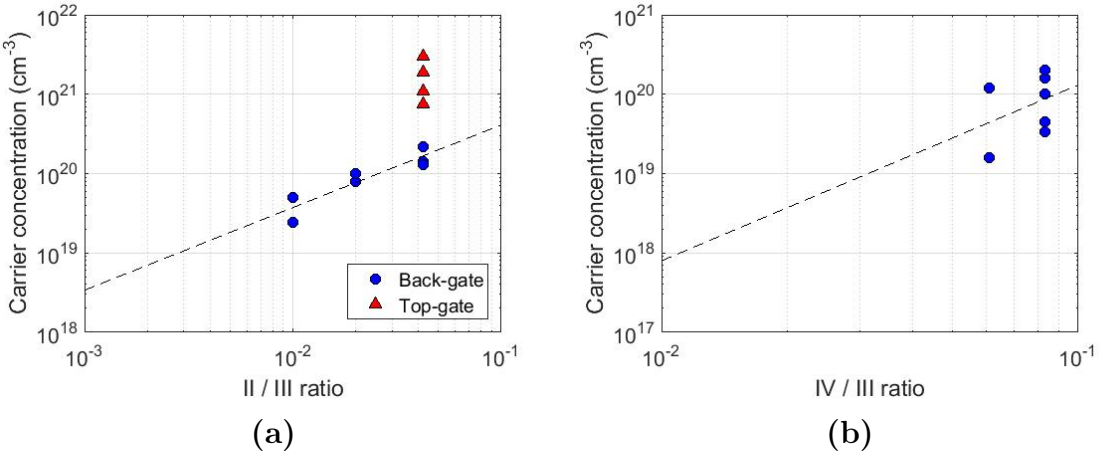

Figure 47: Calculated carrier concentrations as a function of (a) II/III and (b) IV/III ratio. The black dashed lines show log-linear fits to the data (the top-gate results are not included).

6 Conclusions

Doped GaAs nanowires were grown and characterized in this work in order to forward the development of the growth process used by the Nanotechnology group. A growth recipe for undoped GaAs nanowire growth in MOVPE via the VLS mechanism was used as a starting point to which p-type doping with Zn and n-type doping with Sn were added. Several GaAs nanowire samples were grown in this study with either DEZn or TESn dopant precursors and varying II/III or IV/III molar ratios, respectively. Undoped nanowires were additionally grown for reference and a two-step growth recipe was briefly investigated. The effects of doping on nanowire growth were investigated with inspection by SEM and micro-Raman spectroscopy. Carrier concentrations in the nanowires were estimated with electrical measurements for which the nanowires were removed from the growth substrates and contacted.

The results obtained with SEM and micro-Raman indicated that the undoped nanowires had ZB structure and rather good quality while the doped samples suffered from structural defects and tapering to varying degrees. Both SEM and micro-Raman inspections suggested increased defect density with increasing the II/III ratio. Additionally, the II/III ratio of 0.042 resulted in almost doubling the growth rate which was assumed to result from altered Au nanoparticle phase due to increased alloying of Zn. An upper limit for acceptable Zn-doped nanowire growth was deemed to be at the II/III ratio of 0.083. The two-step sample nanowires showed decreased tapering as expected but also slightly worse quality than the corresponding regularly grown nanowires. With Sn doping, the tapering was found to be significantly increased, apparently at the expense of axial growth. The Sn-doped nanowires additionally showed weak Raman signal with a recognizable TO peak only near the tip of the nanowires suggesting that the thick tapering shell had significantly worse structural quality than the axially grown nanowire below. The LO peak was not detected from nanowires with either Sn doping or high II/III ratios possibly due to high doping levels.

An attempt was made to develop a nanowire contacting process that would employ optical lithography with a large number of regular contact patterns instead of defining contacts for each nanowire individually with EBL. The most promising technique tried was dispersing nanowires mechanically using a resist mask and substrate-to-substrate contact achieved with a manual micromanipulator stage. This technique allowed controlled nanowire positioning to some degree and hence significantly improved the chance to align metal contacts on top of the dispersed nanowires. However, it was not uncommon that several nanowires occupied the same resist openings and ended up contacted simultaneously. Worse yet, in most cases, one end of the growth substrate scratched the contact substrate crushing the nanowires while the opposite end was not yet in contact. In the end, the technique was not yet optimized in this work and the yield of contacted nanowires was much lower than initially expected.

The measured (apparent) transconductances indicated p-type doping with Zn and n-type doping with Sn. With Zn doping, the obtained carrier concentration had approximately log-linear dependence on the II/III ratio, similar to what has been reported elsewhere. With Sn doping, the obtained carrier concentrations varied

considerably and were, on average, over an order of magnitude higher than expected based on reported results. The variation in the values might have been related to non-uniformity in the doping.

It should be noted, however, that the accuracy and reliability of the results obtained from electrical measurements might be limited. Firstly, the number of measured nanowires was rather low due to the issues with the contacting. Secondly, the contact resistances could constitute a significant portion of the total resistance and the measurements employing two contacts were hence considered only indicative. Thirdly, the measured currents in the back-gate FET configuration contained significant noise and instabilities, possibly in part due to the back-gate field affecting the contacts and to surface state charging and discharging as the nanowire surfaces were not passivated. In order to further investigate the transconductance measurements, top-gate structures were fabricated on one of the samples with Zn-doped nanowires. In general, the top-gate results yielded lower mobilities than with back-gate measurements by roughly a factor of 10 and the disagreement was likely mostly due to the approximative nature of the capacitance equations. Consequently, there might have been a relatively high systematic error in the obtained mobilities and hence carrier concentrations.

Based on the results obtained in this work, it seems that further effort is required to obtain high quality doped nanowires and reliable estimates of the doping levels. The nanowire growth process would require separate optimization when doping is added to avoid the observed increase in structural defect density and tapering. Techniques like the two-step growth could be employed here. Surface passivation might also improve the stability in the electrical measurements. Furthermore, ohmic contacts and a wrap-gate configuration would be preferred to minimize the ambiguity related to the used models. The carrier concentration values obtained here should give some indication of the doping in the current process, although additional measurements would be needed to confirm the results. However, the dependence is expected to change somewhat when the growth process is altered as a result of the optimization. Since the dopant incorporation is also affected by the growth conditions, several iterations might be needed.

References

[1] K. A. Dick. "A review of nanowire growth promoted by alloys and non-alloying elements with emphasis on Au-assisted III–V nanowires". *Progress in Crystal Growth and Characterization of Materials*, 2008. Vol. **54** (3–4). pp. 138–173. DOI: 10.1016/j.pcrysgrow.2008.09.001.

[2] K. Tomioka, M. Yoshimura, and T. Fukui. "A III-V nanowire channel on silicon for high-performance vertical transistors". *Nature*, 2012. Vol. **488** (7410). pp. 189–192. DOI: 10.1038/nature11293.

[3] J. Svensson, A. W. Dey, D. Jacobsson, and L.-E. Wernersson. "III–V Nanowire Complementary Metal–Oxide Semiconductor Transistors Monolithically Integrated on Si". *Nano Letters*, 2015. Vol. **15** (12). pp. 7898–7904. DOI: 10.1021/acs.nanolett.5b02936.

[4] S. Nadj-Perge, S. M. Frolov, E. P. A. M. Bakkers, and L. P. Kouwenhoven. "Spin–orbit qubit in a semiconductor nanowire". *Nature*, 2010. Vol. **468** (7327). pp. 1084–1087. DOI: 10.1038/nature09682.

[5] E. D. Minot, F. Kelkensberg, M. van Kouwen, J. A. van Dam, L. P. Kouwenhoven, V. Zwiller, M. T. Borgström, O. Wunnicke, M. A. Verheijen, and E. P. A. M. Bakkers. "Single quantum dot nanowire LEDs". *Nano Letters*, 2007. Vol. **7** (2). pp. 367–371. DOI: 10.1021/nl062483w.

[6] D. Saxena, S. Mokkapati, P. Parkinson, N. Jiang, Q. Gao, H. H. Tan, and C. Jagadish. "Optically pumped room-temperature GaAs nanowire lasers". *Nature Photonics*, 2013. Vol. **7** (12). pp. 963–968. DOI: 10.1038/nphoton.2013.303.

[7] M. Yao, N. Huang, S. Cong, C.-Y. Chi, M. A. Seyedi, Y.-T. Lin, Y. Cao, M. L. Povinelli, P. D. Dapkus, and C. Zhou. "GaAs Nanowire Array Solar Cells with Axial p–i–n Junctions". *Nano Letters*, 2014. Vol. **14** (6). pp. 3293–3303. DOI: 10.1021/nl500704r.

[8] J. Wallentin and M. T. Borgström. "Doping of semiconductor nanowires". *Journal of Materials Research*, 2011. Vol. **26** (17). pp. 2142–2156. DOI: 10.1557/jmr.2011.214.

[9] D. L. Sidebottom. *Fundamentals of Condensed Matter and Crystalline Physics*. Cambridge University Press, 2012. ISBN: 978-1-107-01710-8.

[10] S. Elliott. *The Physics and Chemistry of Solids*. Wiley, 1998. ISBN: 978-0-471-98195-4.

[11] H. J. Joyce, J. Wong-Leung, Q. Gao, H. H. Tan, and C. Jagadish. "Phase Perfection in Zinc Blende and Wurtzite III–V Nanowires Using Basic Growth Parameters". *Nano Letters*, 2010. Vol. **10** (3). pp. 908–915. DOI: 10.1021/nl903688v.

[12] N. Cavassilas, F. Aniel, K. Boujdaria, and G. Fishman. "Energy-band structure of GaAs and Si: A sps^* $k \cdot p$ method". *Physical Review B*, 2001. Vol. **64** (11). p. 115207. DOI: 10.1103/PhysRevB.64.115207.

[13] H. Park, R. Beresford, S. Hong, and J. Xu. "Geometry- and size-dependence of electrical properties of metal contacts on semiconducting nanowires". *Journal of Applied Physics*, 2010. Vol. **108** (9). p. 094308. DOI: 10.1063/1.3499698.

[14] Z. Zhang, K. Yao, Y. Liu, C. Jin, X. Liang, Q. Chen, and L.-M. Peng. "Quantitative Analysis of Current–Voltage Characteristics of Semiconducting Nanowires: Decoupling of Contact Effects". *Advanced Functional Materials*, 2007. Vol. **17** (14). pp. 2478–2489. DOI: 10.1002/adfm.200600475.

[15] P. E. Allen and D. R. Holberg. *CMOS Analog Circuit Design*. 3rd ed. New York: Oxford University Press, 2012. ISBN: 978-0-19-993742-4.

[16] P. Nguyen, H. T. Ng, and M. Meyyappan. "Catalyst Metal Selection for Synthesis of Inorganic Nanowires". *Advanced Materials*, 2005. Vol. **17** (14). pp. 1773–1777. DOI: 10.1002/adma.200401717.

[17] R. S. Wagner and W. C. Ellis. "Vapor-liquid-solid Mechanism of Single Crystal Growth". *Applied Physics Letters*, 1964. Vol. **4** (5). pp. 89–90. DOI: 10.1063/1.1753975.

[18] M. Ohring. *Materials Science of Thin Films : Deposition and Structure*. 2nd ed. Academic Press, 2001. ISBN: 9780080491783 (electronic).

[19] T. Mårtensson, C. P. T. Svensson, B. A. Wacaser, M. W. Larsson, W. Seifert, K. Deppert, A. Gustafsson, L. R. Wallenberg, and L. Samuelson. "Epitaxial III–V Nanowires on Silicon". *Nano Letters*, 2004. Vol. **4** (10). pp. 1987–1990. DOI: 10.1021/nl0487267.

[20] L. C. Chuang, M. Moewe, C. Chase, N. P. Kobayashi, C. Chang-Hasnain, and S. Crankshaw. "Critical diameter for III-V nanowires grown on lattice-mismatched substrates". *Applied Physics Letters*, 2007. Vol. **90** (4). p. 043115. DOI: 10.1063/1.2436655.

[21] F. Glas. "Critical dimensions for the plastic relaxation of strained axial heterostructures in free-standing nanowires". *Physical Review B*, 2006. Vol. **74** (12). p. 121302. DOI: 10.1103/PhysRevB.74.121302.

[22] V. G. Dubrovskii, N. V. Sibirev, J. C. Harmand, and F. Glas. "Growth kinetics and crystal structure of semiconductor nanowires". *Physical Review B*, 2008. Vol. **78** (23). p. 235301. DOI: 10.1103/PhysRevB.78.235301.

[23] Y.-C. Chou, K. Hillerich, J. Tersoff, M. C. Reuter, K. A. Dick, and F. M. Ross. "Atomic-Scale Variability and Control of III-V Nanowire Growth Kinetics". *Science*, 2014. Vol. **343** (6168). pp. 281–284. DOI: 10.1126/science.1244623.

[24] P. Paiano, P. Prete, N. Lovergine, and A. M. Mancini. "Size and shape control of GaAs nanowires grown by metalorganic vapor phase epitaxy using tertiarybutylarsine". *Journal of Applied Physics*, 2006. Vol. **100** (9). p. 94305. DOI: 10.1063/1.2364603.

[25] J. Johansson, B. A. Wacaser, K. A. Dick, and W. Seifert. "Growth related aspects of epitaxial nanowires". *Nanotechnology*, 2006. Vol. **17** (11). S355–S361. DOI: 10.1088/0957-4484/17/11/S21.

[26] K. W. Schwarz and J. Tersoff. "Elementary Processes in Nanowire Growth". *Nano Letters*, 2011. Vol. **11** (2). pp. 316–320. DOI: 10.1021/nl1027815.

[27] C.-Y. Wen, J. Tersoff, K. Hillerich, M. C. Reuter, J. H. Park, S. Kodambaka, E. A. Stach, and F. M. Ross. "Periodically Changing Morphology of the Growth Interface in Si, Ge, and GaP Nanowires". *Physical Review Letters*, 2011. Vol. **107** (2). p. 025503. DOI: 10.1103/PhysRevLett.107.025503.

[28] H. J. Joyce, Q. Gao, H. H. Tan, C. Jagadish, Y. Kim, X. Zhang, Y. Guo, and J. Zou. "Twin-Free Uniform Epitaxial GaAs Nanowires Grown by a Two-Temperature Process". *Nano Letters*, 2007. Vol. **7** (4). pp. 921–926. DOI: 10.1021/nl062755v.

[29] X.-Y. Bao, C. Soci, D. Susac, J. Bratvold, D. P. R. Aplin, W. Wei, C.-Y. Chen, S. A. Dayeh, K. L. Kavanagh, and D. Wang. "Heteroepitaxial Growth of Vertical GaAs nanowires on Si (111) Substrates by Metal-Organic Chemical Vapor Deposition". *Nano Letters*, 2008. Vol. **8** (11). pp. 3755–3760. DOI: 10.1021/nl802062y.

[30] C. Gutsche, I. Regolin, K. Blekker, A. Lysov, W. Prost, and F. J. Tegude. "Controllable p-type doping of GaAs nanowires during vapor-liquid-solid growth". *Journal of Applied Physics*, 2009. Vol. **105** (2). p. 024305. DOI: 10.1063/1.3065536.

[31] C. Gutsche, A. Lysov, I. Regolin, K. Blekker, W. Prost, and F.-J. Tegude. "n-Type Doping of Vapor–Liquid–Solid Grown GaAs Nanowires". *Nanoscale Research Letters*, 2010. Vol. **6** (1). p. 65. DOI: 10.1007/s11671-010-9815-7.

[32] H. J. Joyce, Q. Gao, H. H. Tan, C. Jagadish, Y. Kim, M. A. Fickenscher, S. Perera, T. B. Hoang, L. M. Smith, H. E. Jackson, J. M. Yarrison-Rice, X. Zhang, and J. Zou. "High Purity GaAs Nanowires Free of Planar Defects: Growth and Characterization". *Advanced Functional Materials*, 2008. Vol. **18** (23). pp. 3794–3800. DOI: 10.1002/adfm.200800625.

[33] H. J. Joyce, Q. Gao, H. H. Tan, C. Jagadish, Y. Kim, M. A. Fickenscher, S. Perera, T. B. Hoang, L. M. Smith, H. E. Jackson, J. M. Yarrison-Rice, X. Zhang, and J. Zou. "Unexpected Benefits of Rapid Growth Rate for III–V Nanowires". *Nano Letters*, 2009. Vol. **9** (2). pp. 695–701. DOI: 10.1021/nl803182c.

[34] J.-H. Kang, Q. Gao, H. J. Joyce, H. H. Tan, C. Jagadish, Y. Kim, Y. Guo, H. Xu, J. Zou, M. A. Fickenscher, L. M. Smith, H. E. Jackson, and J. M. Yarrison-Rice. "Defect-Free GaAs/AlGaAs Core–Shell Nanowires on Si Substrates". *Crystal Growth & Design*, 2011. Vol. **11** (7). pp. 3109–3114. DOI: 10.1021/cg2003657.

[35] M. T. Borgström, G. Immink, B. Ketelaars, R. Algra, and E. P. A. M. Bakkers. "Synergetic nanowire growth". *Nature Nanotechnology*, 2007. Vol. **2** (9). pp. 541–544. DOI: 10.1038/nnano.2007.263.

[36] C. Soci, X.-Y. Bao, D. P. R. Aplin, and D. Wang. "A Systematic Study on the Growth of GaAs Nanowires by Metal–Organic Chemical Vapor Deposition". *Nano Letters*, 2008. Vol. **8** (12). pp. 4275–4282. DOI: 10.1021/nl801986r.

[37] S. Korte, M. Steidl, W. Prost, V. Cherepanov, B. Voigtländer, W. Zhao, P. Kleinschmidt, and T. Hannappel. "Resistance and dopant profiling along freestanding GaAs nanowires". *Applied Physics Letters*, 2013. Vol. **103** (14). p. 143104. DOI: 10.1063/1.4823547.

[38] I. Regolin, C. Gutsche, A. Lysov, K. Blekker, Z.-A. Li, M. Spasova, W. Prost, and F.-J. Tegude. "Axial pn-junctions formed by MOVPE using DEZn and TESn in vapor–liquid–solid grown GaAs nanowires". *Journal of Crystal Growth*, 2011. Vol. **315** (1). pp. 143–147. DOI: 10.1016/j.jcrysgro.2010.08.028.

[39] R. E. Algra, M. A. Verheijen, M. T. Borgström, L.-F. Feiner, G. Immink, W. J. P. van Enckevort, E. Vlieg, and E. P. A. M. Bakkers. "Twinning superlattices in indium phosphide nanowires". *Nature*, 2008. Vol. **456** (7220). pp. 369–372. DOI: 10.1038/nature07570.

[40] T. Haggrén, J.-P. Kakko, H. Jiang, V. Dhaka, T. Huhtio, and H. Lipsanen. "Effects of Zn doping on GaAs nanowires". In: *Nanotechnology (IEEE-NANO), 2014 IEEE 14th International Conference on*. IEEE, 2014. pp. 825–829. DOI: 10.1109/NANO.2014.6968091.

[41] H. Hasegawa and M. Akazawa. "Surface passivation technology for III–V semiconductor nanoelectronics". *Applied Surface Science*, 2008. Vol. **255** (3). pp. 628–632. DOI: 10.1016/j.apsusc.2008.07.002.

[42] C.-C. Chang, C.-Y. Chi, M. Yao, N. Huang, C.-C. Chen, J. Theiss, A. W. Bushmaker, S. LaLumondiere, T.-W. Yeh, M. L. Povinelli, C. Zhou, P. D. Dapkus, and S. B. Cronin. "Electrical and Optical Characterization of Surface Passivation in GaAs Nanowires". *Nano Letters*, 2012. Vol. **12** (9). pp. 4484–4489. DOI: 10.1021/nl301391h.

[43] F. Jabeen, S. Rubini, F. Martelli, A. Franciosi, A. Kolmakov, L. Gregoratti, M. Amati, A. Barinov, A. Goldoni, and M. Kiskinova. "Contactless monitoring of the diameter-dependent conductivity of GaAs nanowires". *Nano Research*, 2010. Vol. **3** (10). pp. 706–713. DOI: 10.1007/s12274-010-0034-4.

[44] B. S. Simpkins, M. A. Mastro, C. R. Eddy Jr., and P. E. Pehrsson. "Surface depletion effects in semiconducting nanowires". *Journal of Applied Physics*, 2008. Vol. **103** (10). p. 104313. DOI: 10.1063/1.2932072.

[45] T. Haggrén, H. Jiang, J.-P. Kakko, T. Huhtio, V. Dhaka, E. Kauppinen, and H. Lipsanen. "Strong surface passivation of GaAs nanowires with ultrathin InP and GaP capping layers". *Applied Physics Letters*, 2014. Vol. **105** (3). p. 033114. DOI: 10.1063/1.4891535.

[46] A. A. Talin, F. Léonard, B. S. Swartzentruber, X. Wang, and S. D. Hersee. "Unusually Strong Space-Charge-Limited Current in Thin Wires". *Physical Review Letters*, 2008. Vol. **101** (7). p. 076802. DOI: 10.1103/PhysRevLett.101.076802.

[47] G. Bussone, H. Schäfer-Eberwein, E. Dimakis, A. Biermanns, D. Carbone, A. Tahraoui, L. Geelhaar, P. H. Bolívar, T. U. Schülli, and U. Pietsch. "Correlation of Electrical and Structural Properties of Single As-Grown GaAs Nanowires on Si (111) Substrates". *Nano Letters*, 2015. Vol. **15** (2). pp. 981–989. DOI: 10.1021/nl5037879.

[48] S. E. Mohney, Y. Wang, M. A. Cabassi, K. K. Lew, S. Dey, J. M. Redwing, and T. S. Mayer. "Measuring the specific contact resistance of contacts to semiconductor nanowires". *Solid-State Electronics*, 2005. Vol. **49** (2). pp. 227–232. DOI: 10.1016/j.sse.2004.08.006.

[49] T. Haggrén. "Growth of Gallium Arsenide Nanowires on Silicon". Master's thesis. Aalto University, School of Electrical Engineering. Espoo. 2011.

[50] S. Franssila. *Introduction to Microfabrication*. 2nd ed. Wiley, 2010. ISBN: 978-0-470-74983-8.

[51] A. G. Baca, F. Ren, J. C. Zolper, R. D. Briggs, and S. J. Pearton. "A survey of ohmic contacts to III-V compound semiconductors". *Thin Solid Films*, 1997. Vol. **308–309**. pp. 599–606. DOI: 10.1016/S0040-6090(97)00439-2.

[52] G. H. Michler. *Electron Microscopy of Polymers*. Springer-Verlag Berlin Heidelberg, 2008. ISBN: 978-3-540-36350-7.

[53] Q. Li, S.-M. Koo, C. A. Richter, M. D. Edelstein, J. E. Bonevich, J. J. Kopanski, J. S. Suehle, and E. M. Vogel. "Precise Alignment of Single Nanowires and Fabrication of Nanoelectromechanical Switch and Other Test Structures". *Nanotechnology, IEEE Transactions on*, 2007. Vol. **6** (2). pp. 256–262. DOI: 10.1109/TNANO.2007.891827.

[54] O. Wunnicke. "Gate capacitance of back-gated nanowire field-effect transistors". *Applied Physics Letters*, 2006. Vol. **89** (8). p. 083102. DOI: 10.1063/1.2337853.

[55] D. R. Khanal and J. Wu. "Gate Coupling and Charge Distribution in Nanowire Field Effect Transistors". *Nano Letters*, 2007. Vol. **7** (9). pp. 2778–2783. DOI: 10.1021/nl0713301.

[56] I. Zardo, S. Conesa-Boj, F. Peiro, J. R. Morante, J. Arbiol, E. Uccelli, G. Abstreiter, and A. Fontcuberta i Morral. "Raman spectroscopy of wurtzite and zinc-blende GaAs nanowires: Polarization dependence, selection rules, and strain effects". *Physical Review B*, 2009. Vol. **80** (24). p. 245324. DOI: 10.1103/PhysRevB.80.245324.

[57] N. Begum, M. Piccin, F. Jabeen, G. Bais, S. Rubini, F. Martelli, and A. S. Bhatti. "Structural characterization of GaAs and InAs nanowires by means of Raman spectroscopy". *Journal of Applied Physics*, 2008. Vol. **104** (10). p. 104311. DOI: 10.1063/1.3026726.

[58] D. Spirkoska, G. Abstreiter, and A. Fontcuberta i Morral. "Size and environment dependence of surface phonon modes of gallium arsenide nanowires as measured by Raman spectroscopy". *Nanotechnology*, 2008. Vol. **19** (43). p. 435704. DOI: 10.1088/0957-4484/19/43/435704.

[59] O. Salehzadeh, M. X. Chen, K. L. Kavanagh, and S. P. Watkins. "Rectifying characteristics of Te-doped GaAs nanowires". *Applied Physics Letters*, 2011. Vol. **99** (18). p. 182102. DOI: 10.1063/1.3658633.

[60] B. Ketterer, E. Uccelli, and A. Fontcuberta i Morral. "Mobility and carrier density in p-type GaAs nanowires measured by transmission Raman spectroscopy". *Nanoscale*, 2012. Vol. **4** (5). pp. 1789–1793. DOI: 10.1039/C2NR11910B.

[61] M. Hilse, M. Ramsteiner, S. Breuer, L. Geelhaar, and H. Riechert. "Incorporation of the dopants Si and Be into GaAs nanowires". *Applied Physics Letters*, 2010. Vol. **96** (19). p. 193104. DOI: 10.1063/1.3428358.

[62] S. Yazji, I. Zardo, M. Soini, P. Postorino, A. Fontcuberta i Morral, and G. Abstreiter. "Local modification of GaAs nanowires induced by laser heating". *Nanotechnology*, 2011. Vol. **22** (32). p. 325701. DOI: 10.1088/0957-4484/22/32/325701.

[63] S. A. Fortuna and X. Li. "Metal-catalyzed semiconductor nanowires: a review on the control of growth directions". *Semiconductor Science and Technology*, 2010. Vol. **25** (2). p. 024005. DOI: 10.1088/0268-1242/25/2/024005.

[64] A. Javey, S. Nam, R. S. Friedman, H. Yan, and C. M. Lieber. "Layer-by-Layer Assembly of Nanowires for Three-Dimensional, Multifunctional Electronics". *Nano Letters*, 2007. Vol. **7** (3). pp. 773–777. DOI: 10.1021/nl0630561.